

ON TEMPERATURE MEASUREMENTS AND ANALYSIS
IN ELECTRON BEAM ADDITIVE MANUFACTURING
USING NEAR INFRARED THERMOGRAPHY

by

STEVEN PRICE

Y. KEVIN CHOU, COMMITTEE CHAIR

ROBERT TAYLOR

JOHN BAKER

A THESIS

Submitted in partial fulfillment of the requirements
for the degree of Master of Science in the
Department of Mechanical Engineering
in the Graduate School of
The University of Alabama

TUSCALOOSA, ALABAMA

2014

Copyright Steven Price 2014
ALL RIGHTS RESERVED

ABSTRACT

Powder-based electron beam additive manufacturing (EBAM) is a type of additive manufacturing (AM) that utilizes an electron beam to sequentially melt cross-sections of the desired part in a bed of metal powder. There is currently very little understanding of the thermal characteristics of the EBAM process. Therefore, the ability to accurately measure process temperatures is necessary before process models can be validated and closed-loop feedback control systems can be developed. Knowledge of the cooling rates experienced by the part during fabrication is also essential for the development of predictive microstructure models.

In this study, a near-infrared (NIR) thermal imager was used to measure the part temperature during the EBAM process in an Arcam S12 EBAM machine using Ti-6Al-4V powder. The temperature images collected were post-processed to analyze the process temperatures along electron beam scanning path and the size of the molten pool. Several experiments of different settings were conducted to evaluate the effects of transmission loss due to glass metallization and the effects of process parameters and part overhang geometry on temperature distributions and melt-pool sizes.

The major findings are summarized as follows. (1) Metallization on the glass may significantly reduce the transmission rate, and thus, measurement quality. (2) In general, the maximum temperatures during EBAM with Ti-6Al-4V powder are in the range of 2400 °C to 2800 °C, and the length and width of molten pools are in the range of 1.5 to 3.5 mm and 0.6 to 1.0 mm, respectively. (3) The beam speed and current decrease with the build height, but the

decreasing rate becomes much smaller once the build height reaches about 15 to 20 mm. (4) The larger the speed function (SF), the higher the beam speed, and the smaller the molten-pool size, e.g., for length, 2.4 mm for SF20 vs. 1.25 mm for SF65 at a build height of 6.35 mm. (5) In building an overhang feature, the heat dissipation on the overhang side is much poorer due to the low thermal conductivity of the powder. However, such an effect only dominates during the building the first few layers of the overhang feature.

DEDICATION

I would like to dedicate this thesis to my wife, Kayla, because of her endless love and support during my work on this research. This road has been much easier with you by my side.

LIST OF ABBREVIATIONS AND SYMBOLS

C_1	First Radiation Constant
C_2	Second Radiation Constant
E	Spectral Emissive Power
M	Minimizing Variable
r	Radius
T	Temperature
T_0	Room Temperature
T_{app}	Apparent Temperature
T_{envir}	Environment Temperature
T_{true}	True Temperature
ϵ	Emissivity
λ	Wavelength
σ	Stefan-Boltzmann Constant
w_λ	Relative Sensitivity of NIR Camera
AM	Additive Manufacturing
ASTM	American Society for Testing and Materials
CAD	Computer-Aided Design
CCD	Charge Coupled Device
CMOS	Complementary Metal Oxide Semiconductor

EBAM	Electron Beam Additive Manufacturing
EDS	Energy Dispersive X-Ray Spectroscopy
FDM	Fused Deposition Modeling
FPA	Focal Plane Array
LENS	Laser Engineered Net Shaping
NASA	National Aeronautics and Space Administration
NIR	Near Infrared
NIST	National Institute of Standards and Technology
SF	Speed Function
SLS	Selective Laser Sintering

ACKNOWLEDGMENTS

I would like to thank my advisor, Dr. Kevin Chou, for providing me the opportunity to work first as an undergraduate research assistant and then as one of his graduate research assistants. He has provided clear direction and expert advice during the pursuit of my research. I am thankful for his commitment to help me succeed and become a more skilled and knowledgeable engineer.

I would also like to thank Dr. Robert Taylor and Dr. John Baker for their willingness to serve on my committee.

My research group members, Ping Lu, Xibing Gong, Bo Cheng, and Xiaoqing Wang, have been very helpful and willing to provide assistance and advice when needed. I am thankful to have worked with them.

Special thanks are also extended to the Advanced Manufacturing Technology Team from Marshall Space Flight Center for allowing me to use their Arcam EBAM machine to conduct this research. Ken Cooper and James Lydon were always very helpful during my research visits to their facilities.

I would also like to thank Dr. Daniel Fonseca for his advice on the statistical methods used in this research.

Funding for this research was provided by NASA Grant No. NNX11AM11A as well as the Department of Defense SMART Scholarship.

CONTENTS

ABSTRACT.....	ii
DEDICATION.....	iv
LIST OF ABBREVIATIONS AND SYMBOLS.....	v
ACKNOWLEDGMENTS.....	vii
LIST OF TABLES.....	xi
LIST OF FIGURES.....	xii
CHAPTER I	
INTRODUCTION.....	1
Additive Manufacturing.....	1
Powder-Based Electron Beam Additive Manufacturing.....	3
Near-Infrared Thermography.....	7
Motivation and Objectives.....	8
Uniqueness of the Present Work.....	9
Organization of the Thesis.....	9
CHAPTER II	
LITERATURE REVIEW.....	11
Introduction.....	11

Electron Beam Additive Manufacturing.....	11
Infrared Thermography.....	12
Temperature Measurements in Additive Manufacturing.....	16
Emissivity of Ti-6Al-4V.....	19
Summary.....	23

CHAPTER III

EXPERIMENTAL SETUP.....	25
Arcam S12 EBAM Machine.....	25
LumaSense MCS640 Near-Infrared Camera.....	27
Imaging Methodology.....	31
Experiments.....	31
CAD Models used in Experiments.....	33
Summary.....	34

CHAPTER IV

RESULTS AND ANALYSIS.....	35
NIR Imaging of EBAM.....	35
Spatial Resolution Analysis.....	36
Hatch Melting Temperature Profile Analysis.....	38
High Exposure Experiment.....	42
Limited Exposure Experiments.....	48
Controlled Exposure Experiment.....	61

Summary.....	77
CHAPTER V	
PROCESS CONDITION EFFECTS.....	78
Speed Function Experiment.....	78
Overhang Part Experiment.....	96
Summary.....	100
CHAPTER VI	
CONCLUSIONS AND RECOMMENDATIONS.....	101
Conclusions.....	101
Recommendations and Future Work.....	103
REFERENCES.....	104
APPENDIX.....	109

LIST OF TABLES

3.1. Arcam S12 EBAM Ti-6Al-4V Hatch Melting Build Theme Parameters.....26

4.1. Chemical Composition of the Metallization Found Using EDS.....44

LIST OF FIGURES

1.1.	Generic additive manufacturing process.....	1
1.2.	Arcam S12 EBAM Machine.....	3
1.3.	Schematic of Arcam EBAM machine.....	4
1.4.	Acetabular cup and turbine blade manufactured by EBAM.....	6
2.1.	Calculated emissivity of Ti-6Al-4V.....	20
2.2.	Normal spectral emissivity of Ti-6Al-4V obtained during first heating cycle, as a function of (a) wavelength and (b) temperature	21
2.3.	Emissivity plot of Ti-6Al-4V.....	22
2.4.	Integral hemispherical emissivity of Ti-6Al-4V during cooling.....	23
3.1.	Arcam S12 EBAM machine located as Marshall Space Flight Center	26
3.2.	Arcam EBAM machine viewport component arrangement	27
3.3.	Sketch showing position and orientation of the camera relative to the EBAM machine from the (a) side and (b) top views (drawing not to scale).....	29
3.4.	NIR camera experimental setup with Arcam S12 EBAM machine.....	29
3.5.	Arcam S12 EBAM machine heat shield	30
3.6.	NIR image of preheating showing interference from heat shield	30
3.7.	CAD models of parts fabricated in the (a) controlled exposure, (b) speed function, and (c) overhang part experiments.....	34
4.1.	NIR images of the various EBAM fabrication steps taken at different temperature ranges.....	36
4.2.	Binary image of contour melting used for spatial resolution determination.....	37

4.3.	Two-dimensional temperature profile generation procedure- (a) raw NIR image, (b) maximum temperatures in the region of the molten pool identified, (c) trendline generated, (d) individual temperature profile extracted, (e) individual temperature profile aligned, (f) average temperature profile with standard deviations.....	40
4.4.	Temperature profile alignment example.....	41
4.5.	Sacrificial glass from High Exposure Experiment	42
4.6.	NIR images of hatch melting at build heights of (a) 25.97 mm (b) 36.19 mm from the High Exposure Experiment.....	43
4.7.	Transmission rate determination experimental setup.....	45
4.8.	Metallization transmission rate experiment data from High Exposure Experiment.....	46
4.9.	Average temperature profile with standard deviations from the High Exposure Experiment at a build height of 0.77 mm	47
4.10.	Average temperature profiles from the High Exposure Experiment at various build heights from the first build	47
4.11.	Sacrificial glass from Limited Exposure Experiment I	48
4.12.	Metallization transmission rate experiment data from Limited Exposure Experiment I.....	49
4.13.	NIR image of hatch melting at a build height of 20.93 mm from Limited Exposure Experiment I.....	49
4.14.	Average temperature profile with standard deviations from Limited Exposure Experiment I at a build height of 1.33 mm	50
4.15.	Average temperature profiles from Limited Exposure Experiment I that are within 9 layers of each other	51
4.16.	Average temperature profiles from Limited Exposure Experiment I at various build heights	51
4.17.	Identification of liquidus and solidus temperatures on a temperature vs. time graph of Ti-6Al-4V cooling during a casting process.....	52
4.18.	Example temperature versus time curve created from a spatial temperature profile.....	53

4.19.	2D average temperature profiles in the (a) scanning and (b) transverse directions from Limited Exposure Experiment I at a build height of 1.75 mm showing the locations of the average measured liquidus temperature	54
4.20.	Average molten pool dimensions from Limited Exposure Experiment I	55
4.21.	Average molten pool emissivities from Limited Exposure Experiment I.....	57
4.22.	Sacrificial glass from Limited Exposure Experiment II	58
4.23.	Metallization transmission rate experiment data from Limited Exposure Experiment II	58
4.24.	Average temperature profiles from Limited Exposure Experiment II at a variety of build heights	60
4.25.	Average molten pool dimensions from Limited Exposure Experiment II	60
4.26.	Average molten pool emissivities from Limited Exposure Experiment II.....	61
4.27.	Sacrificial glass from Controlled Exposure Experiment with two levels of metallization.....	62
4.28.	Transmission rate determination from the (a) first and (b) second builds of the Controlled Exposure Experiment.....	63
4.29.	Contour melting data from the (a) first and (b) second builds of the Controlled Exposure Experiment used for spatial resolution analysis	64
4.30.	Average temperature profiles from the first build of the Controlled Exposure Experiment	65
4.31.	Average temperatures observed through the (a) lighter and (b) darker sides of the sacrificial glass from the second build of the Controlled Exposure Experiment	66
4.32.	Average temperature profile comparisons from the second build of the Controlled Exposure Experiment at build heights of (a) 6.37 mm, (b) 16.87 mm, and (c) 26.39 mm	68
4.33.	Relationship between temperatures observed through the lighter and darker sides of the sacrificial glass from the second build of the Controlled Exposure Experiment at a build height of 6.37 mm	69
4.34.	Slope of transmission loss relationship at different build heights from first build of the Controlled Exposure Experiment	70

4.35.	Results of transmission loss and emissivity compensation for the average temperature profile from the first build of the Controlled Exposure Experiment at a build height of 6.23 mm.....	71
4.36.	Compensated temperature profiles from the first build of the Controlled Exposure Experiment.....	71
4.37.	Average molten pool dimensions from the (a) first and (b) second builds of the Controlled Exposure Experiment	73
4.38.	Average molten pool emissivities from the (a) first and (b) second builds of the Controlled Exposure Experiment.....	75
4.39.	Average beam speeds from the (a) first and (b) second builds of the Controlled Exposure Experiment.....	76
5.1.	Molten pool during hatch melting at different speed functions.....	79
5.2.	Spatial resolution determination for the (a) first and (b) second builds of the Speed Function Experiment	80
5.3.	Average beam speeds from the (a) first and (b) second builds of the Speed Function Experiment	82
5.4.	Slopes of linear fits between speed functions from the (a) first and (b) second builds of the Speed Function Experiment	83
5.5.	Comparison of estimated beam speeds with actual beam speeds from the (a) first and (b) second builds of the Speed Function Experiment	84
5.6.	Beam speeds from speed function 20 part from second build of the Speed Function Experiment showing notch effect	85
5.7.	Beam current versus build height from the Speed Function Experiment	86
5.8.	Average temperature profiles from the first build of the Speed Function Experiment at build heights of (a) 6.09 mm, (b) 10.71 mm, and (c) 15.19 mm	88
5.9.	Average temperature profiles from the second build of the Speed Function Experiment at build heights of (a) 6.65 mm and (b) 24.43 mm	89
5.10.	Slope of transmission loss relationship at different build heights from the second build of the Speed Function Experiment	90

5.11.	(a) Original and (b) compensated average temperature profiles from the second build of the speed function experiment	91
5.12.	Compensated profiles from the second build of the Speed Function Experiment at 6.65 mm	91
5.13.	Average molten pool lengths from the (a) first and (b) second builds and average molten pool widths from the (c) first and (d) second builds of the Speed Function Experiment.....	94
5.14.	Average molten pool lengths and widths as function of beam speed from the second build of the Speed Function Experiment at build heights of (a) 6.65 mm and (b) 24.43 mm.....	95
5.15.	Averages and ranges of the molten pool dimensions at similar build heights from both builds of the Speed Function Experiment.....	95
5.16.	Overhang CAD model and part fabricated during Overhang Part Experiment.....	96
5.17.	Substrate layout of imaged layer.....	97
5.18.	Temperature maps showing hatch melting over a half powder-half solid substrate.....	97
5.19.	Average temperature profiles from first overhang layer of the Overhang Part Experiment	98
5.20.	Comparison of individual temperature profiles over different substrates from the first overhang layer of the Overhang Part Experiment	98
5.21.	Average temperature profiles from the from the first overhang layer of the Limited Exposure II Experiment.....	99
5.22.	Comparison of individual temperature profiles over different substrates from the first overhang layer of the Limited Exposure Experiment II.....	99

CHAPTER I

INTRODUCTION

Additive Manufacturing

Additive manufacturing (AM) is a category of manufacturing methods that create parts by adding material. The opposite of additive manufacturing is subtractive manufacturing, where material is removed to create the desired part. Most traditional manufacturing processes such as turning, milling, and drilling are subtractive. The basic methodology of AM begins with the creation of part geometry in a computer-aided design (CAD) software package. The part is saved as a .stl file, which approximates the surface geometry of the part with many triangles. Manufacturer supplied software is then used to slice the part model into many layers and set other process parameters. The part is then fabricated by the AM machine one layer at a time. A diagram showing an overview of the entire generic AM process is show in Figure 1.1.

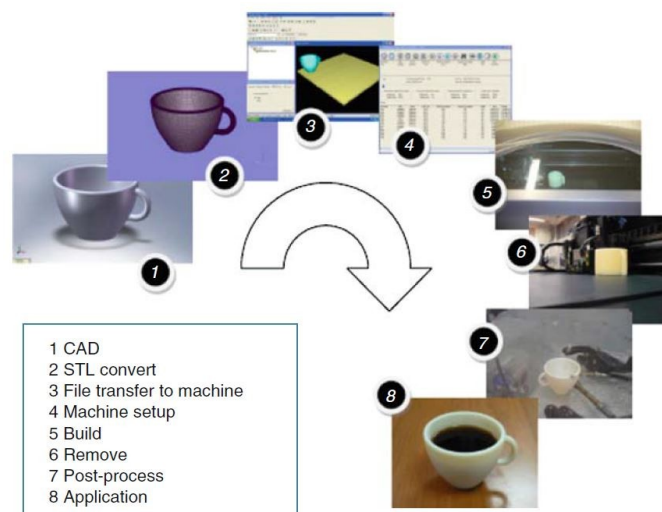


Figure 1.1. Generic additive manufacturing process (Gibson, Rosen, & Stucker, 2010).

The American Society for Testing and Materials (ASTM) Standard F2792-12a (2012) has defined seven AM process categories. What makes each AM process category unique is their method of fabricating the part layers. One of the most common AM process categories is material extrusion (fused deposition modeling). A plastic filament is heated to a semi-liquid state and extruded out of a nozzle to create the part layers. Another process called vat photopolymerization (stereolithography) shines an ultraviolet light onto a photosensitive resin causing it to harden. AM processes also exist that are capable of producing metal parts. These processes use either a laser or electron beam to melt or sinter metal powder or wire together, forming each layer. The two major AM process categories that are used to produce metal parts are powder bed fusion and directed energy deposition. The process studied in this work, powder-based electron beam additive manufacturing (EBAM), is classified as a powder bed fusion process.

Additive manufacturing has many advantages over traditional manufacturing techniques. Because AM uses a layer-based manufacturing method, the fabrication of many complex part geometries such as internal channels and 3D meshes are possible that are extremely difficult to manufacture using traditional manufacturing techniques. AM does not require any tooling which gives it an initial cost and lead time advantage when compared with processes such as casting and forging. In many cases, fabrication time when using AM will be much shorter than if a traditional manufacturing process was used. Many industries are finding AM processes advantageous, with the aerospace and biomedical fields showing particularly heavy interest. AM is well suited for these industries in particular, due to its ability to quickly manufacture custom, small batch parts.

Powder-Based Electron Beam Additive Manufacturing

Powder-based electron beam additive manufacturing is a powder bed fusion additive manufacturing process developed and marketed exclusively by Arcam AB in Sweden. The process uses an electron beam to melt the layers of the part in a bed of metal powder. The Arcam EBAM machine shown in Figure 1.2 is capable of producing of layers as thin as 70 μm . Figure 1.3 shows a schematic of the major components of the Arcam EBAM machine. A tungsten filament is used to generate electrons which are then accelerated by a voltage of 60 kV. Magnetic fields are used as various lenses that focus the electrons in order to create a beam and then deflect the beam to impact the build surface at the correct locations. The metal powder is stored in hoppers on two sides of the build platform and a rake is used to spread the powder for each layer. The build chamber of the Arcam machine is held at a vacuum of 10^{-3} - 10^{-5} mbar during fabrication in order to prevent impurities such as oxidation from forming in the part.



Figure 1.2. Arcam S12 EBAM Machine (Arcam AB, n.d.).

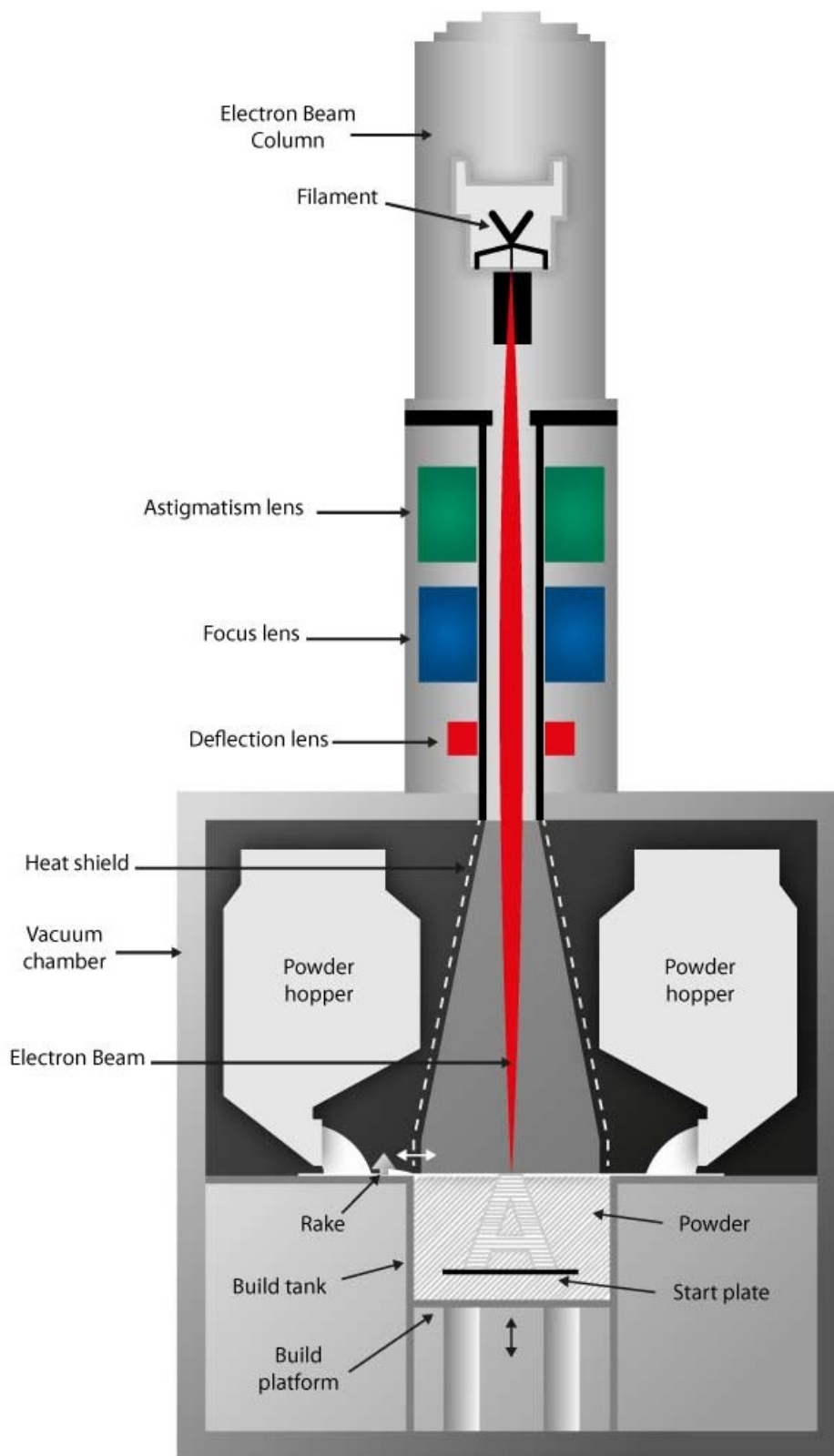


Figure 1.3. Schematic of Arcam EBAM machine (Arcam AB, n.d.).

The EBAM build sequence begins with stage plate heating. The electron beam scans over the surface of the steel build plate until it reaches a temperature of 730 °C. Once the stage plate has been heated, the layer fabrication process initiates. The fabrication of each layer includes several steps. In the first step, the electron beam scans at a high power and high speed over the build surface in order to preheat the powder. Preheating serves two purposes in the EBAM process. First, preheating elevates the temperature of the powder before melting in order to reduce the residual stresses in the part. Second, preheating lightly sinters the powder together in order to reduce the expulsion of powder during melting due to the repelling force felt between the ionized powder particles. Next the electron beam scans around the perimeter of the cross-section of the part to melt it. The electron beam deflects quickly between several locations on the perimeter in order to maintain multiple molten pools simultaneously. Hatch melting occurs next by scanning the electron beam at high power and slower speeds in order to create a single molten pool. The electron beam scans a raster pattern on the inside of the cross-section in order to melt the interior of the part. Lastly, the build platform lowers one layer thickness and a new layer of powder is spread on top of the build surface by the rake. When the part fabrication has completed, the part is cooled very slowly over a period of several hours in order to reduce post-fabrication part distortion.

Because EBAM can create full density parts made of alloys such as Ti-6Al-4V and CoCr, the process has many potential applications in both the aerospace and medical industries. Ti-6Al-4V is a widely used aerospace alloy that can be used to make parts that experience high thermal stresses, such as turbine blades. The ability of EBAM to build highly customized CoCr parts also makes it an excellent process for the manufacture of medical implants. Figure 1.4

shows an acetabular cup used in hip joint replacements and a turbine blade that were both manufactured using EBAM.



Figure 1.4. Acetabular cup and turbine blade manufactured by EBAM (Arcam AB, 2013).

EBAM has several advantages over laser-based AM processes. EBAM has a higher power density than laser-based AM processes, enabling it to achieve faster build times. The absorption rate achieved by EBAM is also higher than laser-based processes, making EBAM the more efficient process.

As discussed above, the EBAM process has many advantages; however the process still has many challenges to be addressed. The surface roughness of EBAM parts is greater than metal parts produced by laser-based powder bed fusion AM processes. The dimensional accuracy of EBAM parts is not as high as parts machined using traditional subtractive manufacturing processes. Process monitoring is also very challenging due to the harsh environment within the build chamber. All viewports into the build chamber are made with

thick, leaded glass and the exposure of this glass during fabrication allows metal particles to be deposited onto the glass, eventually limiting the visibility into the build chamber.

Near-Infrared Thermography

Conducting accurate temperature measurements of the EBAM process is a very challenging task. As discussed in the previous section, the electron beam generates a transient, point heat source that produces very high temperatures and extreme thermal gradients. Because of these process characteristics, the use of thermocouples is impractical due to their lack of spatial information and slow response time.

Infrared thermography is a non-contact temperature measurement technique that measures the amount of radiation in one or more bands of the infrared spectrum that is being emitted by a surface. By specifying surface emissivity and transmission rate, software can use the amount of detected radiation to calculate the temperature of the surface. Single color infrared cameras use a single wavelength or wavelength band and require knowledge of the surface emissivity. Two-color infrared cameras use two wavelengths or wavelength bands in an attempt to bypass the emissivity requirement, but they depend on the assumption that the emissivity of the surface is independent of wavelength. This is also known as the “grey body” assumption.

Infrared thermography is better suited for the EBAM process because of its spatial temperature measurement capability and faster response time. The near-infrared portion of the infrared spectrum is particularly appropriate for the EBAM process because of its ability to detect the very high temperatures reached during fabrication. The temperature measurements made in the near-infrared spectrum are also less sensitive to surface emissivity than the farther regions of the infrared spectrum, meaning there will be less error due to the uncertainty of the

assumed surface emissivity. However, there are still other aspects of the EBAM machine and process that make the use of near-infrared thermography techniques challenging.

The EBAM process creates ionizing radiation therefore the machine is built to contain this radiation, protecting individuals in the vicinity of the machine. Due to this design requirement, the viewport into the build chamber of the EBAM machine is made of two thick glasses. These glasses cause transmission loss in the near-infrared spectrum. During fabrication, metal particles are deposited onto the interior surface of the viewport glass if exposed. To protect the thick viewport glass from metallization, a thin piece of clear sacrificial glass is placed in front of the thick glass. A metal shutter then shields the sacrificial glass during the process; however it can be manually opened by the user during fabrication to allow observation of the build platform. The metallization that forms on the sacrificial glass also causes transmission losses of varying degrees depending on its severity. Transmission losses that are not accounted for during the measurement can cause the measured temperatures to be lower than the true temperatures.

Motivation and Objectives

The ability to make accurate temperature measurements of the molten pool during the EBAM process is a foundational capability that must be established before process models can be validated and technologies like closed loop feedback control systems can be implemented successfully. Molten pool monitoring could prove useful for improving the dimensional accuracy of EBAM parts as well as producing parts with more homogenous microstructures. A thorough understanding of the molten pool geometry and temperature gradients in the EBAM process are also vital to the development of accurate microstructure models.

Temperature measurements of the EBAM process made using a near-infrared camera supply thermal information about the EBAM process that can be analyzed to study a variety of topics. The temperatures and shape of the molten pool during hatch melting were studied as well as the effect that process parameters have on the molten pool. The transmission loss caused by the metallization of the sacrificial glass and its effect on the NIR temperature measurements was also studied in order to better understand how to minimize and compensate for its impact on the temperature measurements.

Uniqueness of the Present Work

This work presents the results and analysis of temperature measurements of the EBAM process made using NIR thermography. In this research, high spatial resolution temperature measurements of the molten pool in EBAM were conducted for the first time. A novel approach to the estimation of the molten pool emissivity is also presented. A new method of compensating for transmission loss and incorrect molten pool emissivity is shown. This work also examined the relationships between beam speed, build height, and molten pool size. The thermal effects of fabricating overhang structures were also studied.

Organization of the Thesis

Chapter II of this thesis reviews literature on the topics of electron beam additive manufacturing, infrared thermography, temperature measurements of additive manufacturing processes, and the emissivity of Ti-6Al-4V. Chapter III discusses the experimental setup of the Arcam S12 EBAM machine and the LumaSense near-infrared camera, the imaging methodology and CAD models used, and the various experiments conducted. Chapter IV presents the major analysis methods used and presents temperature profiles of the molten pool as well as results related to the study of effects related to metallization of the sacrificial glass. Chapter V contains

the results of the process parameter effects study. The electron beam translational speed and molten pool size were studied at several different speed function values. A study of the thermal effects of melting overhang geometry is also presented. Chapter VI provides a discussion of conclusions from this research and gives recommendations for future work in this field.

CHAPTER II

LITERATURE REVIEW

Introduction

Electron beam additive manufacturing is a relatively new technology that has generated much research interest due to its relevance to the aerospace and biomedical industries. There are also many precedents for the use of near-infrared thermography to measure manufacturing process temperatures. This chapter reviews previous research that is related to the topics of EBAM, NIR thermography, temperature measurements in additive manufacturing, and the emissivity of Ti-6Al-4V.

Electron Beam Additive Manufacturing

With the growing interest in AM, a wide variety of research has been conducted in relation to the EBAM process. Gong, Anderson, and Chou (2012) provided a review of the research related to EBAM part microstructure, mechanical properties, and process simulations that has been completed. As with any new process, the parts made by electron beam additive manufacturing must be characterized so that their suitability for various applications can be determined. Cormier, Harrysson, and West (2004a) conducted analyses of the microstructure of H13 steel parts produced using an Arcam S12 EBAM machine. Cormier et al. (2004b) also studied how the microstructure of Ti-6Al-4V parts manufactured by EBAM varied between bulk and thin-walled parts. Gong and Chou (2013) characterized sintered Ti-6Al-4V powder that was formed during the EBAM preheating phase. Schwerdtfeger, Singer, and Kömer (2012) used an

infrared camera to detect flaws in EBAM manufactured parts after the hatch melting phase had completed, but before the new layer of powder had been spread. Kahnert, Lutzmann, and Zaeh (2007) studied the effects of various scanning strategies and energy densities on layer connection for the electron beam sintering of H11 tool steel powder. Al-Bermani, Blackmore, Zhang, and Todd (2010) investigated how the magnitude of the preheating temperature in the EBAM process affects the microstructure and mechanical properties of EBAM parts. Shen and Chou (2012) developed a three dimensional finite element thermal model of the molten pool in the EBAM process to study the effects of powder bed porosity and beam diameter on molten pool size. Hrabe and Quinn (2013) researched the effects that part size and distance from the build plate had on the microstructure and mechanical properties of EBAM manufactured Ti-6Al-4V parts. Zäh and Lutzmann (2010) developed a mathematical model of the temperature distribution during EBAM scanning and simulated various combinations of process parameters in an attempt to eliminate defects such as delamination and melt ball formation. Gong, Cheng, Price, and Chou (2013) performed work related to EBAM sintered powder characterization, EBAM process simulations, and EBAM process metrology. Gong, Rafi, Starr, and Stucker (2013) conducted a Taguchi experiment in order to study the effects that the parameters max current, focus offset, line offset, and speed function number had on EBAM part porosity.

Infrared Thermography

Infrared thermography is a widely used non-contact temperature measurement method because it provides excellent spatial resolution and does not affect the temperature of the target it is measuring. Infrared measurement techniques leverage Planck's Law to determine the temperature of a surface from the radiation emitted by that surface. Planck's Law shown in

Equation 1 is a fundamental equation that determines the spectral emissive power of a blackbody as a function of temperature and wavelength.

$$E = \frac{C_1}{\lambda^5 \left(e^{\frac{C_2}{\lambda T}} - 1 \right)} \quad (1)$$

E is the spectral emissive power at a specific temperature and wavelength. λ is the wavelength of the radiation and T is the absolute temperature of the blackbody. C_1 is the first radiation constant which is equal to $119.1 \mu\text{W} \cdot \mu\text{m}^2/\text{sr}$ and C_2 is the second radiation constant which is equal to $14388 \mu\text{m} \cdot \text{K}$. If Planck's Law is integrated over all wavelengths, the result is the Stefan-Boltzmann Law shown in Equation 2 which states that the power radiated per unit area of a blackbody, E, is proportional to the fourth power of the absolute temperature of the surface, T, by the Stefan-Boltzmann constant, σ , which is equal to $5.670 \times 10^{-8} \text{ W/m}^2 \cdot \text{K}^4$.

$$E = \sigma T^4 \quad (2)$$

Since theoretical blackbodies are perfect emitters they have an emissivity of 1, however all real objects have emissivities less than 1. The Stefan-Boltzmann equation can be modified to work for graybodies which are ideal bodies whose emissivity is less than 1, but is not wavelength dependent (Haggqvist, Sikström, & Christiansson, 2013). Equation 3 shows the Stefan-Boltzmann equation modified for use with gray bodies.

$$E = \varepsilon \sigma T^4 \quad (3)$$

Emissivity is the ratio of the radiation emitted by a surface over the radiation emitted by a blackbody at the same temperature. It is a material property that is also dependent on many factors such as temperature, wavelength, surface condition, and incidence angle. Because emissivity is dependent on so many factors, it is a very difficult parameter to know with certainty. Transmission rate is also a factor that must be considered in many measurement scenarios. An object such as a protective glass that is in between the target surface and the

camera will cause the transmission rate of radiation in the infrared spectrum to decrease. The amount that the radiation is attenuated is affected by the wavelength of the radiation and the properties of the object in the path.

Infrared thermography has been used to study process temperatures in many types of manufacturing methods. O'Sullivan and Cotterell (2001) used an Inframetrics Thermacam (Model PM380E) infrared camera with a 256 x 256 resolution to measure the temperatures of an aluminum workpiece during a turning process. Pittalà and Monno (2011) used a FLIR ThermaCAM SC3000 infrared thermal imager with a temperature range of -2 to 2000 °C to help validate a thermal predictive model for the face milling of Ti-6Al-4V. Miller, Li, Wang, and Shih (2006) measured the workpiece temperature during friction drilling using a Raytheon Radiance IR camera system sensitive in the 3-5 μm wavelength range. Alkemper, Buchholz, Murakami, and Ratke (1995) used a charge-coupled detector (CCD) camera sensitive to the 1-1.6 μm wavelength range to monitor the solidification of several aluminum alloys in aerogel moulds. Hjertсэн, Sjöström, Bergström, and Näsström (2004) measured a forging tool's surface temperature using a Varioscan 3021-ST infrared camera.

Infrared radiation is typically divided into the following bands: near-infrared (0.75-1.4 μm), short-wavelength infrared (1.4-3 μm), mid-wavelength infrared (3-8 μm), and long-wavelength infrared (8-15 μm) (Miller, 1994). Detectors operating in the near-infrared band have a high sensitivity at high temperatures and are less sensitive to emissivity variations, which makes the NIR band an ideal choice for the measurement of the very high process temperatures of the EBAM process (Outeiro, Dias, & Lebrun, 2004). Error caused by the uncertainty in the true emissivity will be minimized by the use of the NIR spectrum.

NIR cameras have been used to measure temperatures in a wide variety of processes. Outeiro et al. (2004) and M'Saoubi and Chandrasekara (2004, 2011) used NIR cameras to measure temperatures in turning processes. Outeiro et al. (2004) used a CCD camera sensitive in the 0.85-1.0 μm spectral range and that had a resolution of 1000 x 1018 pixels. M'Saoubi and Chandrasekara (2004) used a CCD camera sensitive in the 0.8-1.1 μm spectral range and also measured temperatures in the range of 500-1000 $^{\circ}\text{C}$. The camera had a resolution of 752 x 582 pixels and a visible area of 3.5 mm x 2.5 mm. M'Saoubi and Chandrasekara (2011) used a CCD camera sensitive in the 0.85-1.1 μm spectral range and measured temperatures in the range of 500-1000 $^{\circ}\text{C}$. Kaschnitz, Reiter, and McClure (2002) used a CCD device sensitive up to 1.3 μm to monitor temperatures in a permanent mold casting process. Pomfret, Steinhurst, and Owrutsky (2010) used an Allied Vision Technologies Stingray F033B ASG CCD camera with a 75 mm focal length telephoto lens to measure the temperature of a solid oxide fuel cell anode. The camera was sensitive in the 0.72-1.0 μm spectral range. Thermocouples were attached to the part and used to calibrate the NIR camera. Ageorges, Ye, and Hou (2000) used a Photometrics Sensys CCD camera to monitor temperatures during a resistance welding process. The camera was sensitive up to 0.9 μm and could measure temperatures above 180 $^{\circ}\text{C}$. Four thermocouples were placed on the sample surface and used to calibrate the NIR camera. Gao, You, and Katayama (2012) used a NAC high-speed CMOS camera to measure the temperature of the molten pool in a fiber laser welding process. The camera was sensitive to the 0.96-0.99 μm spectral range, had a frame rate of 1000 frames/second, and a pixel resolution of 8.77 $\mu\text{m}/\text{pixel}$. Li (2010) used a Mikron MI-GAR12-LO infrared camera sensitive at 0.7 μm to measure the temperature of a Ti-6Al-4V sample in an electrostatic levitator.

Temperature Measurements in Additive Manufacturing

Both contact and non-contact temperature measurement methods have been applied in additive manufacturing to measure process temperatures. Thermocouples and various types of infrared cameras have been used to measure the temperatures during many types of AM.

Sun, Rizvi, Bellehumeur, and Gu (2008) used 0.0118 mm Type-K thermocouples to monitor temperatures during an FDM process. Rodriguez et al. (2012) used a Type-K thermocouple to measure the temperature of an EBAM manufactured part heated with an electron beam. Qian, Mei, Liang, and Wu (2005) used thermocouples to measure temperatures during a direct laser fabrication process. Griffith et al. (1998, 1999) used 10 μm Type-C thermocouples to measure temperature during a Laser Engineered Net Shaping (LENS) process. Pasandideh-Fard, Bhola, Chandra, and Mostaghimi (1998) used a fast response (10 μs) stainless steel sheathed chromel-alumel thermocouple to measure the surface temperature variation during the deposition of liquid tin droplets on a stainless steel surface. Zäh and Lutzmann (2010) placed thermocouples in the build plate of an EBAM machine and measured the temperature response as the electron beam passed above the thermocouples. The response time of thermocouples, however, tends to be too slow to accurately measure the temperatures in the EBAM process because of the fast transient heating.

Noncontact temperature measure methods such as infrared cameras and detectors are better suited for use with AM processes. Because they do not touch the target, noncontact methods do not affect the target temperature. Infrared cameras also have the capability to take spatial temperature measurements, which provides much more information than point temperature measurement when studying AM processes. Some of the various camera models that have been used to monitor AM processes are a Raytheon Radiance HS camera (Kolossoy,

Boillat, Glardon, Fischer, & Locher, 2004; Fischer, Romano, Weber, & Kolossov, 2004; Fischer et al., 2004), a Mikron M67S temperature sensor (Ho, Cheung, & Gibson, 2002), Impac IGA 5-LOMB25 radiation pyrometer (Hagqvist, Sikström, & Christiansson, 2013), Thermaviz two-wavelength pyrometer (Wang, Felicelli, & Craig, 2009), FLIR A320 infrared camera (Schwerdtfeger, Singer, & Kömer, 2012), Raytek MR1S dual wavelength point temperature instrument (Gao, Xing, Zhang, Luo, & Zheng, 2008), and a FLIR Prism DS infrared camera (Griffith et al., 1998, 1999). The spectral ranges of single wavelength cameras used were 0.7-1.06 μm (Hu, Mei, & Kovacevic, 2001, 2002; Hu and Kovacevic, 2003a, 2003b), 1.45-1.8 μm (Hagqvist et al., 2013), 3-5 μm (Kolossov et al., 2004; Wegner and Witt, 2011; Gao et al., 2008; Fischer et al., 2004), and 3.6-5 μm (Griffith et al., 1998, 1999). The sampling rates of these cameras and sensors varied anywhere from 0.5 Hz (Wang et al., 2009) to 10 kHz (Craeghs et al., 2011). The spatial resolutions of these cameras varied from as high as 2 $\mu\text{m}/\text{pixel}$ (Chivel and Smurov, 2007) to as low as 1500 $\mu\text{m}/\text{pixel}$ (Wegner and Witt, 2011). The cameras had a wide variety of resolutions. Many of the cameras had a resolution of 128 x 128 pixels (Hu et al., 2001, 2002; Hu & Kovacevic, 2003a, 2003b). Kolossov et al. (2004) and Fischer et al. (2004) both had cameras with a resolution of 256 x 256 pixels while Rodriguez et al. (2012) used a camera with a much larger resolution of 640 x 480 pixels. The cameras were mounted to view the build surface in various different configurations. The angle of the camera relative to the build surface can have effects on the spatial resolution of the images. Also, the surface emissivity varies as a function of emission angle. Some cameras were mounted coaxially to a laser head (Hua, Jing, Xin, Fengying, & Weidong, 2008; Hu and Kovacevic, 2003a, 2003b), while others were mounted at an angle to the build surface normal direction. Wang et al. (2009) mounted their IR camera at an angle of 75° to observe a LENS process. Schwerdtfeger et al.

(2012) used an angle of 15° to watch for flaws in the EBAM process. Wegner and Witt (2011) used a wide angle lens mounted at 5° to measure the temperature distribution during a laser sintering process and telephoto lens mounted at 23° to measure the temperature of the melt pool. Rodriguez et al. (2012) used a mounting angle of 25° to observe an EBAM process and Ho et al. (2002) observed an SLS process from a 45° angle. Campo et al. (2010) researched the sensitivity of the emissivity of a variety of aeronautical alloys to emission angle and found that at short wavelengths the emissivity remained fairly constant for angles between $0-60^\circ$ from the build surface normal. The emissivity began to quickly decrease at angles above 60° . A variety of calibration methods have been used to ensure accurate temperature measurement. Tan, Chen, Zhang, Lin, and Huang (2010) calibrated their camera with an ultrahigh temperature blackbody calibrator and Wang et al. (2009) calibrated their camera with a tungsten filament provided by the National Institute of Standards and Technology.

NIR cameras are well suited for use with many additive manufacturing processes because of their high sensitivity at high temperatures. Many researchers have already utilized NIR cameras in their study of AM processes. Zalameda et al. (2013) used a Prosilica GC1380H digital NIR camera to image an electron beam freeform fabrication process. The NIR camera had a spectral range of $0.4-1.05 \mu\text{m}$; however a long pass filter trimmed the bottom end of the range up to $0.9 \mu\text{m}$ in order to eliminate the camera's response to visible light. Wang, Felicelli, and Craig (2007) captured thermal images during the fabrication of a single wall using the LENS process. They used a ThermaViz two-wavelength imaging pyrometer that had two detectors, one sensitive in the $0.7-0.8 \mu\text{m}$ band and another sensitive in the $0.8-0.9 \mu\text{m}$ spectral band. Two-wavelength (two-color) infrared cameras attempt to determine the target temperature without having to know the target's emissivity by assuming the target is a "graybody" (assumption that

emissivity is constant at all wavelengths and is independent of direction). Since graybodies do not actually exist, the graybody assumption will inherently introduce a certain amount of error and reduce the signal to noise ratio (Davies, Ueda, M'Saoubi, Mullany, & Cooke, 2007).

Emissivity of Ti-6Al-4V

A single-color near infrared camera was selected to be used in the experiments shown in this work, so an accurate estimate of the emissivity of the build surface was needed. Therefore it was necessary to investigate what emissivities of Ti-6Al-4V have been determined from previous research. Since the conditions of each experiment were different and emissivity is sensitive to surface roughness and temperature as well as other factors, so a wide range of reported results were found.

Hagqvist et al. (2013) calculated the emissivity of a Ti-6Al-4V boss formed by laser metal deposition (LMD). They used an Impac IGA 5-LO MB25 narrow wave-band pyrometer and S, N, and K type thermocouples to monitor the temperature of the boss as it was heated by an induction heater to temperatures in excess of 1550 K. The camera was sensitive to the spectral range of 1.45-1.8 μm . Their results are shown in Figure 2.1. The black line is the calculated emissivity and the grey lines are the 95% confidence intervals.

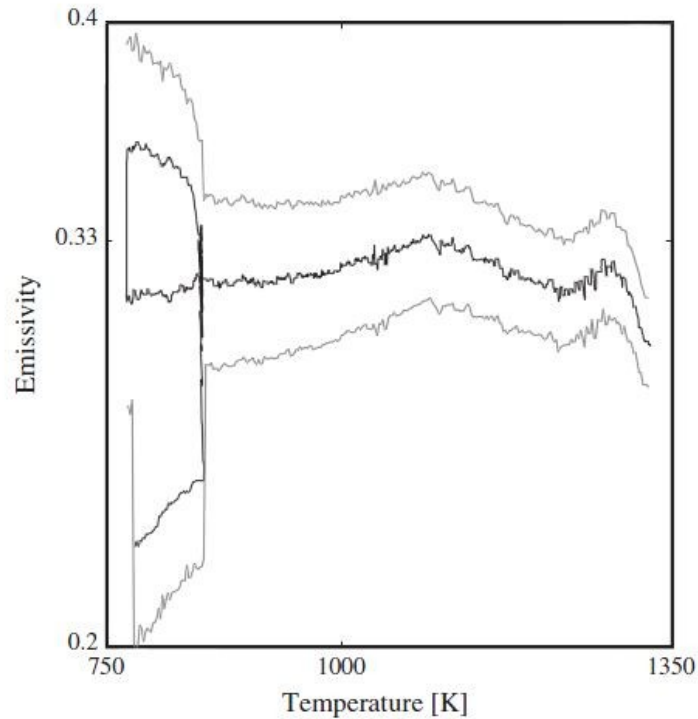


Figure 2.1. Calculated emissivity of Ti-6Al-4V (Hagqvist et al., 2013).

González-Fernández, Risueño, Pérez-Sáez, and Tello (2012) investigated the spectral emissivity at an angle normal to the part surface of polished Ti-6Al-4V discs using a high accuracy infrared radiometer sensitive in the medium infrared spectrum. They determined the emissivity of the discs at various wavelengths and temperatures. The normal spectral emissivity they calculated is shown in Figure 2.2 as functions of wavelength and temperature. The emissivity began to sharply increase as the wavelength dropped below 6 μm .

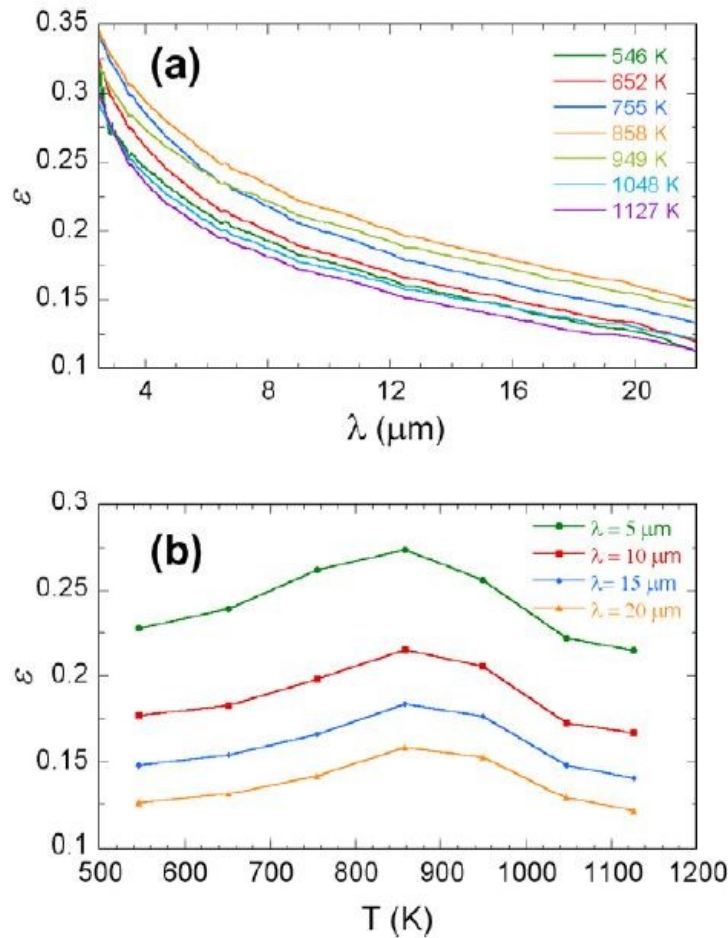


Figure 2.2. Normal spectral emissivity of Ti-6Al-4V obtained during first heating cycle, as a function of (a) wavelength and (b) temperature (González-Fernández et al., 2012).

Rodríguez et al. (2012) determined the emissivity of Ti-6Al-4V parts manufactured by EBAM. The parts were designed with cavity radiators to generate blackbody sources. The EBAM machine was used to heat the parts to a temperature of around 700 °C, then a FLIR SC645 IR camera was used to capture images of the parts. By comparing the temperatures of the surface of the part and the blackbody source, they determined the emissivity of the surface. The emissivity they determined is shown in Figure 2.3 as a function of temperature.

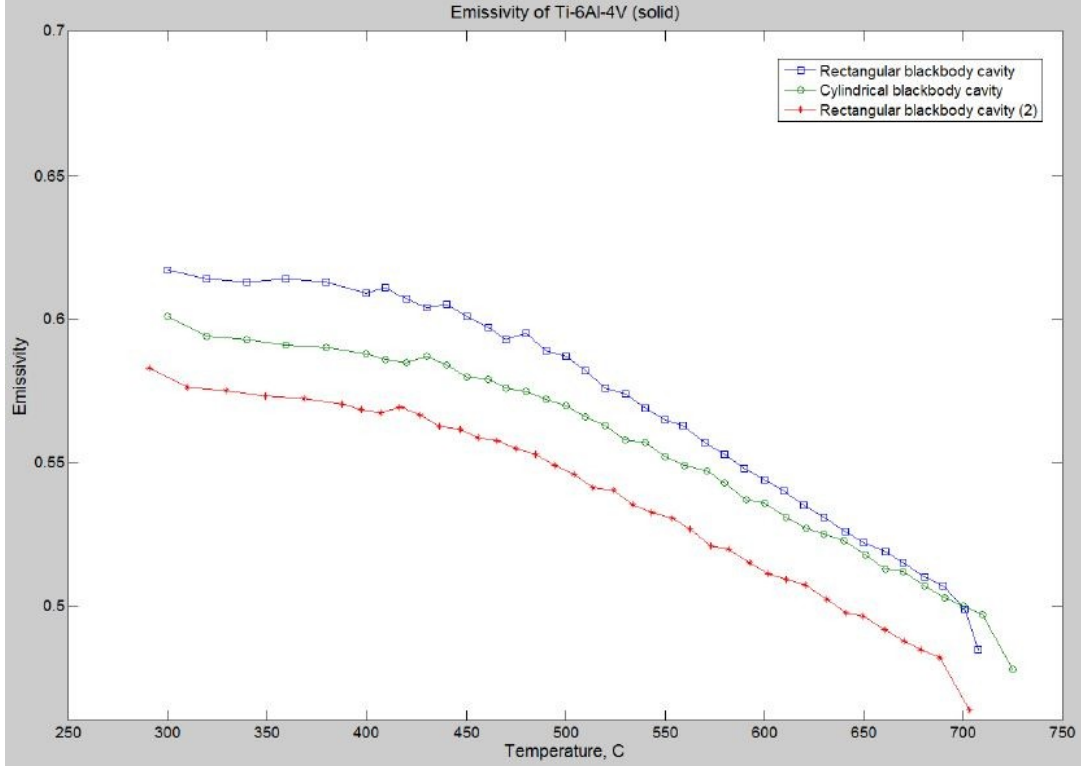


Figure 2.3. Emissivity plot of Ti-6Al-4V (Rodriguez et al., 2012).

Li (2009) determined the hemispherical total emissivity of a Ti-6Al-4V sample suspended by electrostatic levitation. He used a single color pyrometer sensitive at 700 nm to monitor the sample. A free cooling curve was determined and used to calculate dT/dt which was used in Equation 4 to develop an expression for the ratio of the constant-pressure heat capacity and the total hemispherical emissivity as a function of temperature.

$$mC_p \frac{dT}{dt} = -4\pi r^2 \varepsilon \sigma_{SB} (T^4 - T_0^4) \quad (4)$$

mC_p is the heat capacity, r is the radius of the sample, σ_{SB} is the Stefan-Boltzmann constant, ε is the total hemispherical emissivity, T is the sample temperature, and T_0 is the room temperature.

For liquid Ti-6Al-4V, the ratio was calculated to be:

$$\frac{C_{p,l}}{\varepsilon_{T,l}} = 3064 + 0.1291(T - T_m) \frac{J}{kg \cdot K} \text{ for } 1661 \text{ K} \leq T \leq 1977 \text{ K.} \quad (5)$$

For solid Ti-6Al-4V, the ratio was calculated to be:

$$\frac{c_{p,s}}{\varepsilon_{T,s}} = 2699 + 0.08191(T - T_m) \frac{J}{kg \cdot K} \text{ for } 1200 \text{ K} \leq T \leq 1943 \text{ K.} \quad (6)$$

If a value for the heat capacity is known, it can be plugged into the appropriate equation and an expression for the total hemispherical emissivity at constant heat capacity can be found. Li chose a heat capacity of 931 J/kg·K from literature and found that the emissivity of liquid Ti-6Al-4V at its melting temperature was 0.304.

Shur and Peletskii (2004) measured the integral hemispherical emissivity of various alloys of titanium including Ti-6Al-4V. An EOP-66 standard optical pyrometer was used to measure the temperature of the surface of the samples which contained channels that served as blackbody sources. The integral hemispherical emissivity of the Ti-6Al-4V part calculated by the authors is shown in Figure 2.4 as a function of emissivity.

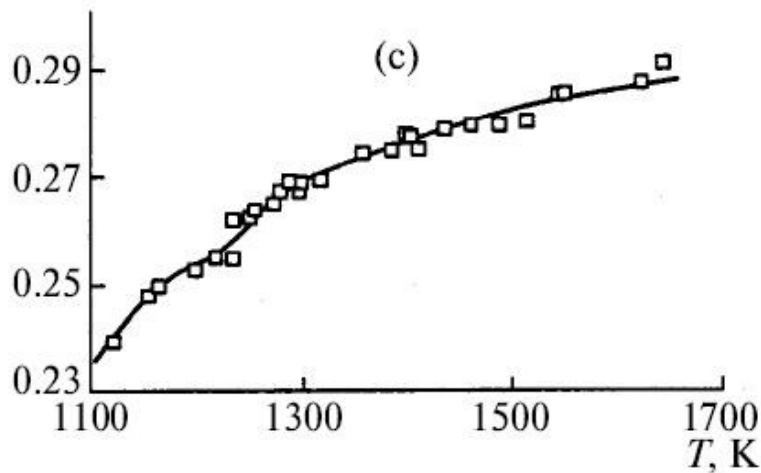


Figure 2.4. Integral hemispherical emissivity of Ti-6Al-4V during cooling (Shur and Peleskii, 2004).

Summary

Industry's rising interest in additive manufacturing has increased the need for research that improves the quality and efficiency of all AM processes. Research conducted in the fields of EBAM and infrared thermography has been reviewed. An examination of various

temperature measurement techniques used in AM was conducted. The work completed to determine the emissivity of Ti-6Al-4V at various temperatures and wavelengths has also been reviewed.

CHAPTER III

EXPERIMENTAL SETUP

Arcam S12 EBAM Machine

An Arcam S12 EBAM machine at NASA's Marshall Space Flight Center, pictured in Figure 3.1, was used to fabricate the test parts. The material used was gas-atomized Ti-6Al-4V powder and the layer thickness used was 70 μm . The standard build theme for Ti-6Al-4V was used when defining the parameters of the builds. There are several important parameters that are unique to the Arcam EBAM process. The maximum current sets a limit on the maximum current used to generate the electron beam during hatch melting. The actual beam current is controlled by an algorithm that is a function of build height as well as part geometry. The focus offset current controls the offset of the focal point of the electron beam from the build surface. The speed function index controls the translational speed of the electron beam. The actual beam speed is not constant during the build so an increase in the speed function index results in larger beam speeds during the entire build. The line offset is the distance between scanning paths during hatch melting. The major Ti-6Al-4V build theme parameters for hatch melting are shown in Table 3.1. Because the EBAM process produces radiation, the viewport into the build chamber is made of several thick glasses. During melting in the EBAM process, metal particles will adhere to any unprotected glass surface. Therefore a thin piece of clear sacrificial glass is placed in front of the thick glasses in order to protect them from metallization. This sacrificial glass can easily be replaced after each build. A metal shutter is positioned in front of the

sacrificial glass and shields it from metallization while the shutter is closed. A lever next to the viewport allows the shutter to be manually opened, enabling the build surface to be observed. A diagram showing the layout of the various pieces of the viewport is provided in Figure 3.2 in order to provide clarity.



Figure 3.1. Arcam S12 EBAM machine located as Marshall Space Flight Center.

Table 3.1

Arcam S12 EBAM Ti-6Al-4V Hatch Melting Build Theme Parameters

Parameter	Value
Maximum Beam Current	17 mA
Focus Offset Current	19 mA
Speed Function	36
Line Offset	0.2 mm

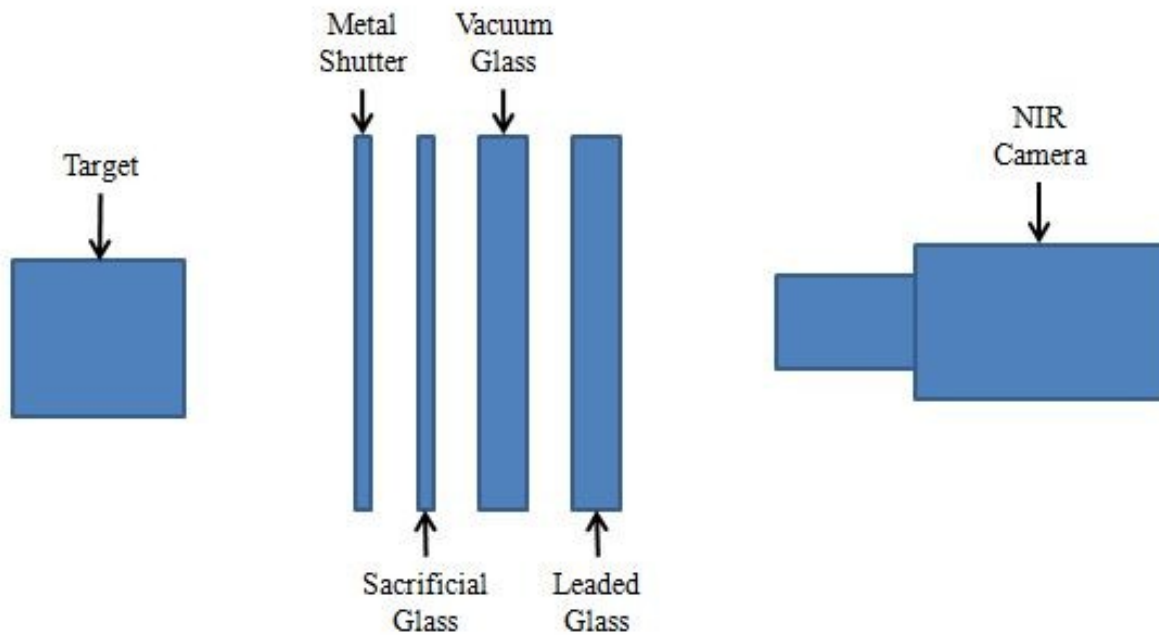


Figure 3.2. Arcam EBAM machine viewport component arrangement.

LumaSense MCS640 Near-Infrared Camera

A LumaSense MCS640 near-infrared camera was used to make the spatial temperature measurements of the build surface which were used for analysis in this study. The NIR camera has a spectral range of 0.78-1.08 μm and a 640 x 480 pixel uncooled focal plane array (FPA) sensor. The image capturing system has a maximum frame rate of 60 Hz and a detectable temperature range of 735-2446 $^{\circ}\text{C}$ which is divided into three nominal temperature ranges: low (735-1108 $^{\circ}\text{C}$), medium (1057-1485 $^{\circ}\text{C}$), and high (1503-2446 $^{\circ}\text{C}$). The camera has a lens with a minimal 500 mm working distance and a view area of 31 mm x 23 mm at 500 mm distance. The camera was calibrated by the camera manufacturer with the same glasses in the viewport of the Arcam S12 EBAM machine so that a transmission rate setting of 100% will correctly account for the transmission losses due to the glasses. The emissivity of the surface was unknown so measurements were taken with an assumed emissivity of 0.35. The integration time of the image

capturing system is 16.25 ms, 1.7 ms, and 50 μ s for the low, medium, and high temperature ranges respectively. The data acquisition system consists of a laptop and an Ethernet cable, connected with a gigabit Ethernet express card.

The NIR camera was mounted on a tripod and positioned to look downward through the EBAM machine's viewport onto the build platform. The camera was vertically inclined at approximately 35° from the surface normal with minimal roll angle and horizontal yaw. A sketch of the camera's arrangement in relation to the EBAM machine is provided in Figure 3.3. An image showing the NIR camera positioned to monitor the build surface is shown in Figure 3.4. The Arcam S12 EBAM machine also contains a heat shield, shown in Figure 3.5, that is positioned between the viewport and the build platform. This heat shield has a cutout for viewing the build platform; however the cutout is obstructed with vertical bars. During the High Exposure Experiment, it was found that these bars caused interference in the temperature data collected using the NIR camera. The interference from the bars can be clearly seen in the NIR image of preheating shown in Figure 3.6. The bars were cut in the subsequent experiments in order to eliminate the interference.

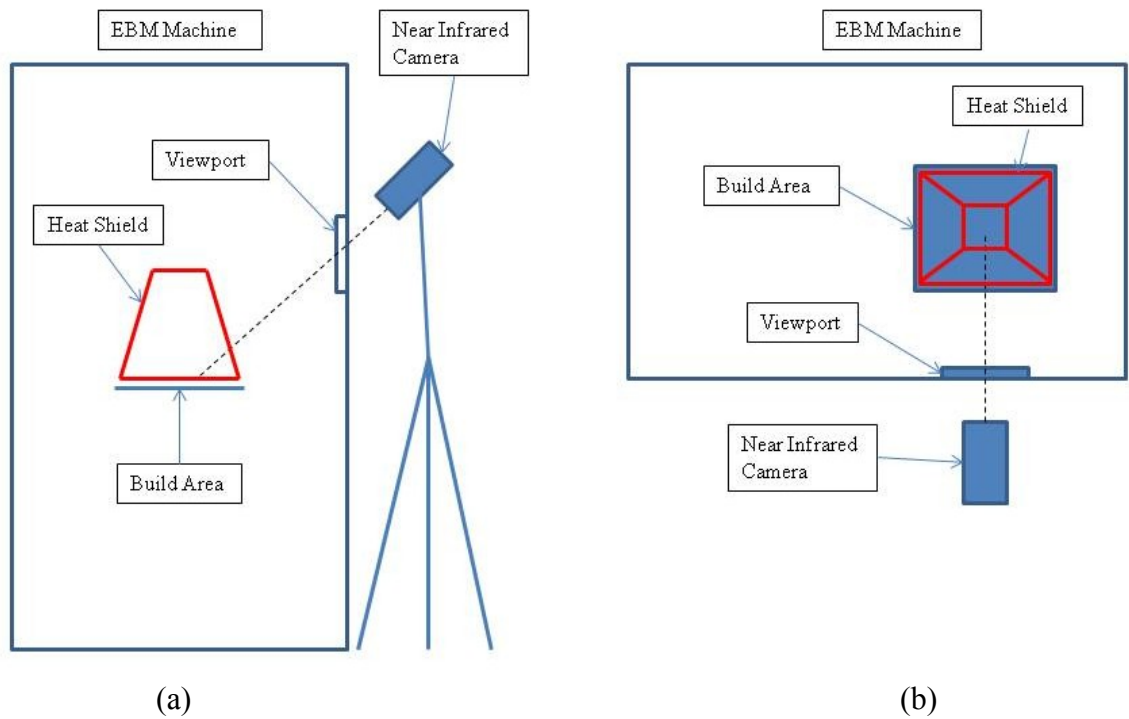


Figure 3.3. Sketch showing position and orientation of the camera relative to the EBAM machine from the (a) side and (b) top views (drawing not to scale).



Figure 3.4. NIR camera experimental setup with Arcam S12 EBAM machine.



Figure 3.5. Arcam S12 EBAM machine heat shield.

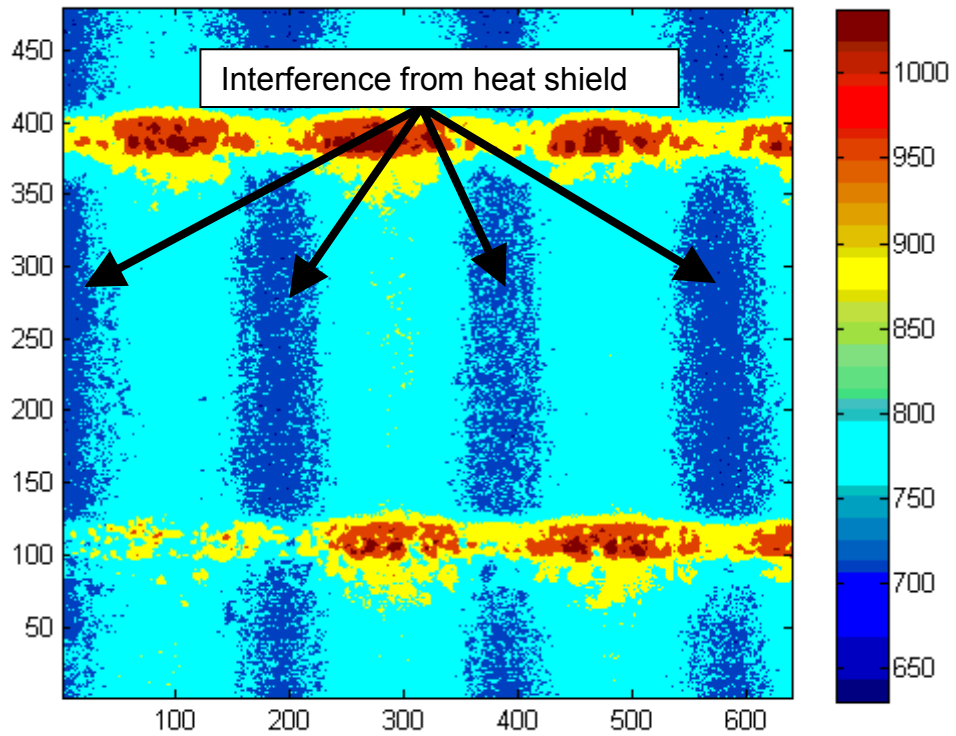


Figure 3.6. NIR image of preheating showing interference from heat shield.

Imaging Methodology

The shutter shielding the glass was opened each time temperature measurements were made. Once the build plate had been heated to around 700 °C before layer fabrication began, the build plate could be seen using the low temperature range of the NIR camera. This enabled the NIR camera to be positioned in front of the viewport and manually adjusted to achieve a focused image without metallization of the sacrificial glass occurring. The camera software was then used to specify the length of the videos to be captured. Also, because of the vertical inclination of the camera, the horizontal spatial resolution of the camera was higher than the vertical resolution. Therefore only layers whose hatch melting raster direction was horizontal were imaged. During the preheating phase of the fabrication of the layer of interest the shutter was opened and the NIR video recording was initiated just prior to the beginning of contour melting. Upon completion of the hatch melting phase, the shutter was closed.

Experiments

Several different experiments were conducted to study a variety of topics related to temperature measurements of the EBAM process and the thermal characteristics of the molten pool. The details of each experiment will be presented in the next two chapters, but a short summary of each experiment is listed below:

1. High Exposure Experiment:

The purpose of this experiment was to gain an initial understanding of the capabilities and challenges of using NIR thermography techniques to measure EBAM process temperatures. The fabrication of a block was imaged at many different layers during the build. No effort to limit the exposure of the sacrificial glass was made, so the glass experienced heavy metallization.

2. Limited Exposure Experiment I:

The sacrificial glass exposure time was reduced in this experiment which successfully reduced the level of metallization. Three bars from the heat shield were trimmed, which reduced, but did not entirely eliminate the interference caused by the heat shield.

3. Limited Exposure Experiment II:

This experiment was similar to the Limited Exposure Experiment I, but this time five bars were trimmed from the heat shield which entirely eliminated the interference. Two dimensional temperature profiles were generated and studied to see how their shape and magnitude changed with build height and increasing metallization. Results from this experiment were also used in the Overhang Experiment.

4. Controlled Exposure Experiment:

This experiment was conducted in order to characterize the effects on NIR temperature measurements from transmission loss due to metallization of the sacrificial glass. The left half of the sacrificial glass was covered to protect it during the fabrication of the first part. After the build was completed, the transmission loss due to metallization on the exposed half of the glass was determined. The left half of the glass was then uncovered and the glass was reused in an identical build. This allowed for the molten pool on an individual layer to be observed through two different levels of metallization, allowing for a study of the effects of metallization on the temperature measurements.

5. Speed Function Experiment:

The effects of the speed function parameter on the molten pool were studied in this experiment. Four parts were fabricated at the same time using four different speed

function values. The NIR camera was used to image the melting at several different build heights. The speed, emissivity, and temperature profiles of the molten pool were studied. Two identical runs of this experiment were made so comparisons of the data could be possible.

6. Overhang Part Experiment:

The purpose of this experiment was to study how the melting of part features over a powder substrate versus a solid substrate affects the thermal characteristics of the EBAM process. A part was fabricated with several overhang features. The fabrication of the overhang features was imaged using the NIR camera. The changes in the hatch melting cooling rate when melting over a powder substrate versus a solid substrate were studied.

CAD Models Used in Experiments

CAD models of the parts fabricated during the experiments are shown in Figure 3.7. The parts were designed with several aspects in mind. Easily identifiable features were needed in order to facilitate the calculation of the spatial resolutions of the images. This calculation process will be discussed in detail in Chapter IV. The widths of the parts were also made to be such that when centered in the camera's view the part would extend much past the left and right edges of view. This was done in order to ensure that the molten pool during hatch melting was at steady state when in the camera's field of view. The parts for the High Exposure and Limited Exposure experiments had solid, rectangular cross-sections. The parts for the Limited Exposure experiments were also designed so that at higher build heights overhang melting could be studied as well as the standard melting. The part for the Controlled Exposure Experiment was designed with notches that made identification of the part center easier so that the camera could be aligned

correctly. Four parts were fabricated in the Speed Function Experiment. The parts were designed so that all four could be seen in the vertical direction of the field of view. The Overhang Experiment part was designed with several overhanging “shelves”. These were positioned so that the molten pool would scan back and forth from a solid substrate to a powder substrate when melting these shelves.

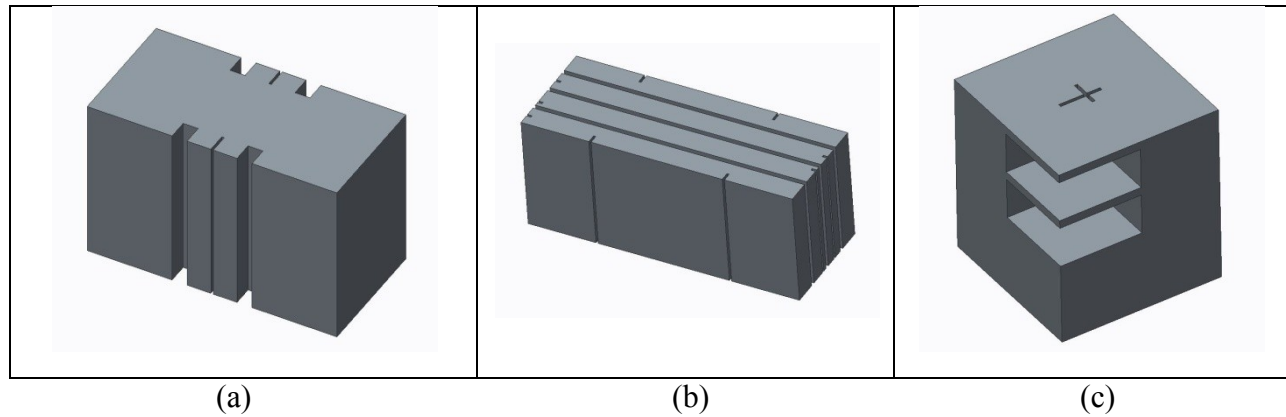


Figure 3.7. CAD models of parts fabricated in the (a) controlled exposure, (b) speed function, and (c) overhang part experiments.

Summary

An Arcam S12 EBAM machine and a LumaSense MCS640 NIR camera were the primary pieces of equipment used in this research. The NIR camera was used to capture images of the build surface of the Arcam S12 EBAM machine during fabrication. The parts built during the experiments were specifically designed with geometry that met the specific criteria needed for successful temperature measurements in each experiment.

CHAPTER IV

RESULTS AND ANALYSIS

This chapter presents the methodology and results of various analyses of the data collected from NIR temperature measurements of the EBAM process. The effects of transmission loss due to metallization of the sacrificial glass were studied in order to better understand and compensate for their impact on the NIR temperature measurements. Average temperature profiles of the molten pool during hatch melting were generated so that the temperatures of the molten pool could be visualized. Characteristics of the molten pool during hatch melting such as estimated emissivity and dimensions were calculated.

NIR Imaging of EBAM

The NIR camera used in the experiments had three different temperature ranges: low, medium, and high. The different phases of the EBAM fabrication process were imaged using each of the default temperature ranges in order to determine the appropriate temperature range to be used for each phase. Example NIR images of each phase from each temperature range are shown in Figure 4.1. The cross-section being fabricated in the images is a 1 in. x 1 in. square. No image is shown for the high temperature range imaging of preheating because the preheating temperatures were below the minimum detectable temperature of the high temperature range. The high temperature range was found to be the best for imaging hatch melting. The medium temperature range was found to be the most useful for detecting the perimeter of the cross-section during contour melting. Preheating was best imaged using the low temperature range.

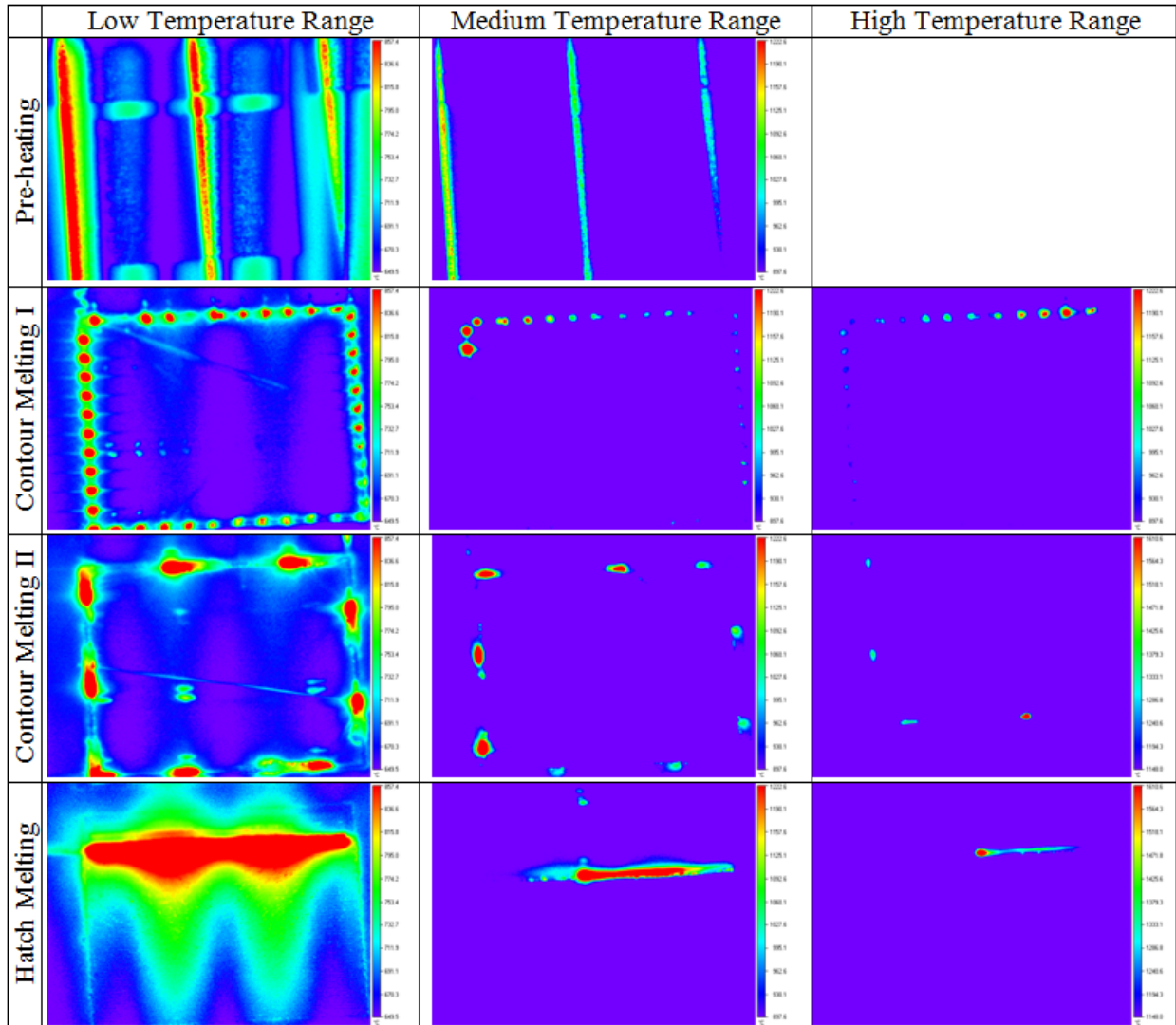


Figure 4.1. NIR images of the various EBAM fabrication steps taken at different temperature ranges.

Spatial Resolution Analysis

The first analysis conducted in most experiments was the determination of the spatial resolutions. The spatial resolutions were necessary for determining the scale of the features in each image. Because the camera was positioned at an angle from the build surface normal, the vertical resolution of the pixels in the thermal images was larger than the horizontal resolution. During the design of the parts to be fabricated in the experiments, identifiable features such as notches were placed on the parts in such a way that they may be observed in the NIR images. By

determining the number of pixels between these identifiable features in the vertical and horizontal directions, the resolutions could be calculated. Typically the top and bottom edges of the part cross-section were designed to fit into the NIR camera's field of view and notches were placed in these edges. These features could then be observed during the contour melting portion of the EBAM process. Since the true distances between the features were known, the spatial resolutions could be calculated. A Matlab code was developed to identify the locations of high temperatures during every frame showing contour melting. A single binary image showing these locations was then used to identify the features to measure between. The distances between the features in pixels were calculated and used to find the spatial resolutions in $\mu\text{m}/\text{pixel}$. An example binary image of compiled contour melting high temperature locations is shown in Figure 4.2. The blue lines indicate the positions of the identified edges and the red lines indicate the distances measured.

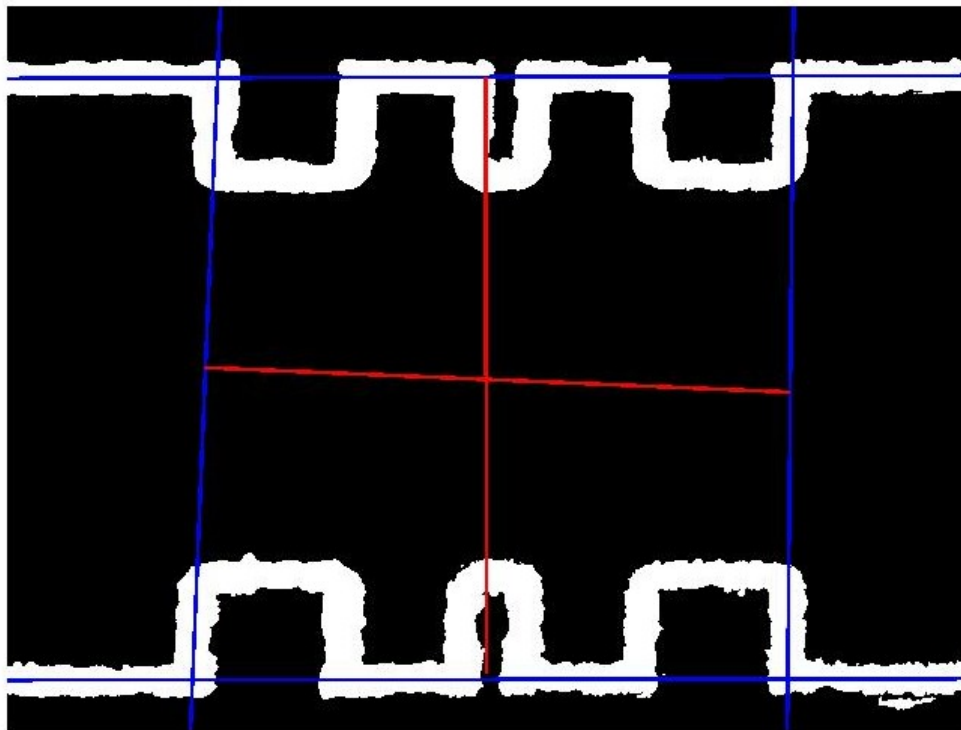


Figure 4.2. Binary image of contour melting used for spatial resolution determination.

Hatch Melting Temperature Profile Analysis

Hatch melting is the phase of the EBAM process that produces the interior of the part when the electron beam scans across the powder bed in a raster pattern, melting the powder as it travels. For most parts, hatch melting is the primary step in the fabrication of the part layers and therefore has a critical impact on the final properties of the part.

In order to characterize the thermal aspects of the hatch melting phase, two-dimensional temperature profiles along the scanning paths were generated from the NIR images. The two-dimensional temperature profiles reveal the thermal gradients of the heating and cooling sides of the scanning paths as well as show the length of the phase transition region of the cooling side. The temperature profiles from individual NIR images were somewhat noisy in the phase transition and below, likely due in part to variations in the emissivity of the powder bed surface as well as the sensitivity of the NIR camera at those temperatures. In order to smooth the temperature profiles and gain a better understanding of the overall shape of the profiles, the individual temperature profiles from a single layer were averaged together. The standard deviations of the temperatures of the average profile were also calculated in order to determine statistical information about the repeatability of the temperature measurements. A detailed explanation of the temperature profile determination and averaging procedure is given next.

Since the horizontal resolution of the NIR images was higher than the vertical resolution, only layers where the scanning paths were horizontal were imaged. The scanning path was determined by identifying the location of the hottest pixel in each column of the image. The locations of pixels with temperatures below a certain magnitude were ignored so as to only identify locations in the region of the molten pool. A trendline was then generated from the identified pixels. This trendline represents the scanning path. The temperatures along the

trendline were extracted, resulting in a raw, two-dimensional temperature profile of the molten pool from that specific image. Because the location of the beam was constantly moving, the position and orientation of the temperature profiles vary from image to image. In order to facilitate averaging, the individual temperature profiles were all aligned together using their peak temperatures and oriented so that their scanning direction would appear rightward. The averages and standard deviations of the temperatures at each point on the temperature profile were calculated. The final result was an average temperature profile for that particular layer with error bars representing one standard deviation. The distance dimension was also converted from pixels to millimeters. A graphical summary of the average temperature profile generation procedure is shown in Figure 4.3. Figure 4.4 shows how temperature profiles can be generated and aligned for molten pools with different orientations.

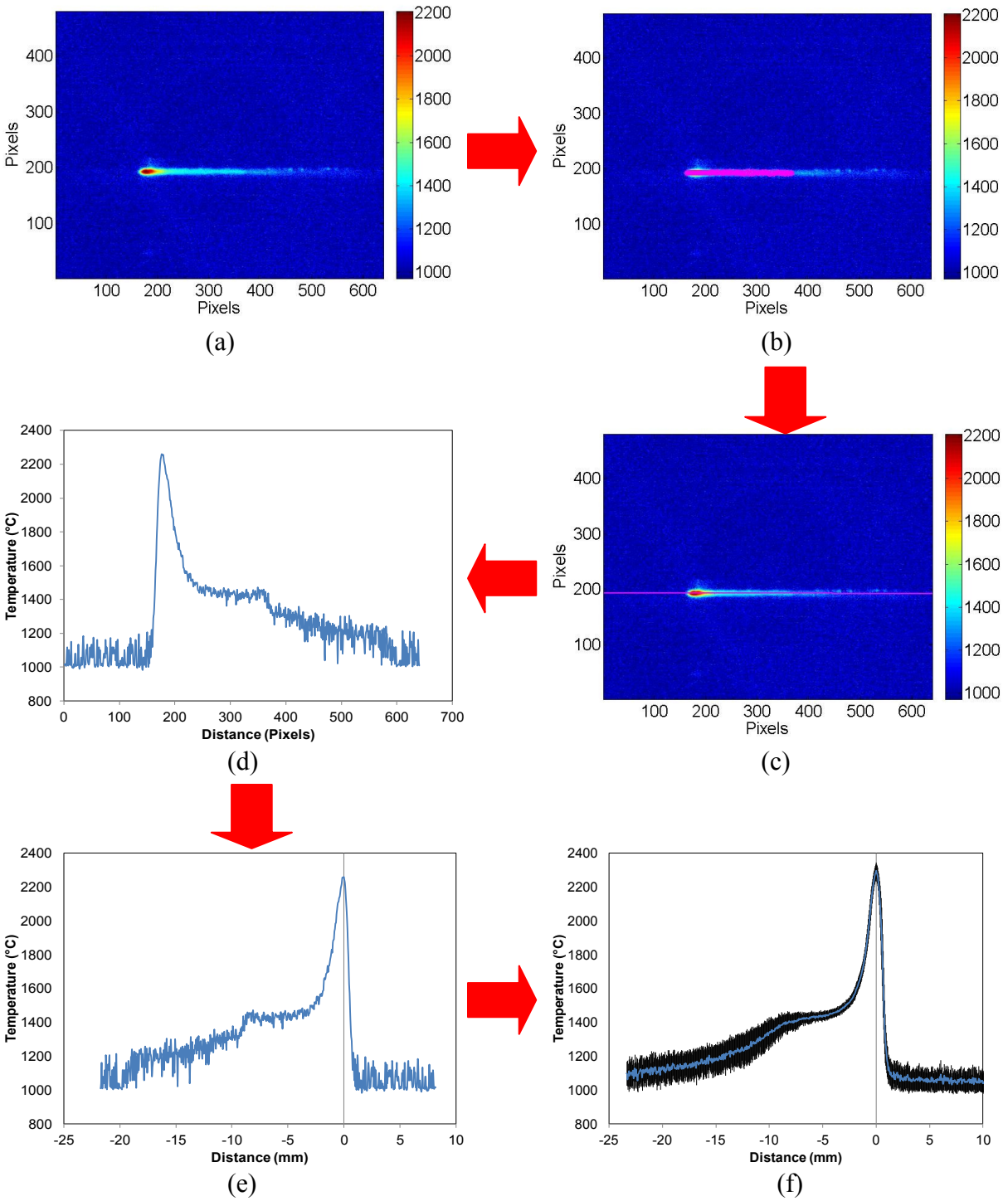


Figure 4.3. Two-dimensional temperature profile generation procedure- (a) raw NIR image, (b) maximum temperatures in the region of the molten pool identified, (c) trendline generated, (d) individual temperature profile extracted, (e) individual temperature profile aligned, (f) average temperature profile with standard deviations.

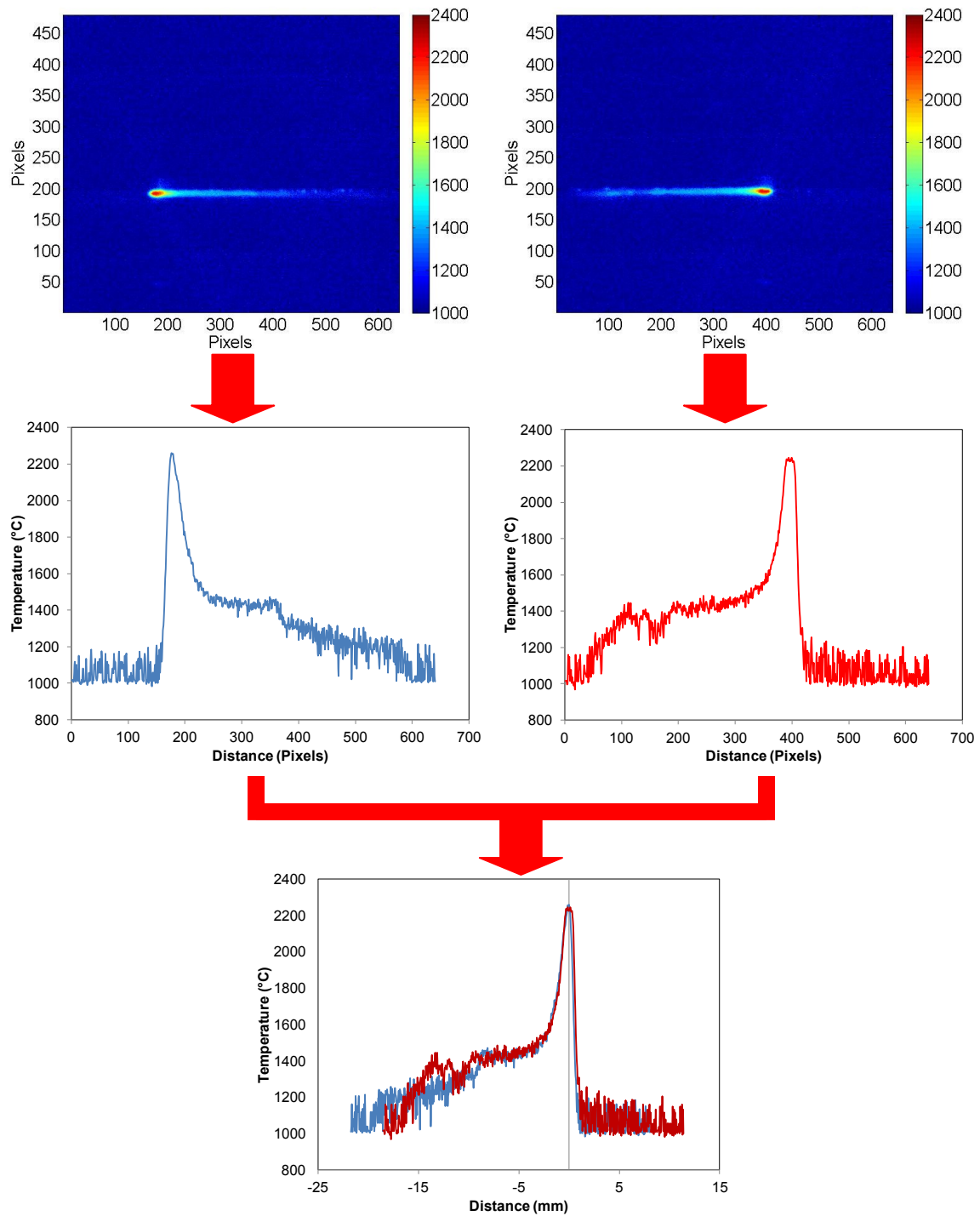


Figure 4.4. Temperature profile alignment example.

High Exposure Experiment

This purpose of this experiment was to gain an initial understanding of the quality and repeatability of the temperature measurements made of the EBAM process using the NIR camera. The part fabricated in this experiment was a block 63.5 mm long in the x direction, 101.6 mm tall in the z direction, and 25.4 mm wide in the y direction. During this experiment 38 NIR videos averaging around 25 seconds each were taken of the EBAM process. Therefore the sacrificial glass experienced a total exposure time of around an estimated 16 minutes. The sacrificial glass accumulated a large amount of metallization during the build as shown in Figure 4.5. Based upon these results, it was decided that the exposure time of the sacrificial glass should be reduced in future experiments. Figure 4.6 shows two NIR images of the molten pool during hatch melting at build heights of 25.97 mm and 36.19 mm. The process parameters being used at these two points in the build were relatively similar, but the temperatures from 36.19 mm are clearly lower than what is seen at 25.97 mm. The decrease in the measured temperatures was due to the transmission loss caused by the metallization of the sacrificial glass that occurred during the 4.3 minutes of exposure that happened between the two images.

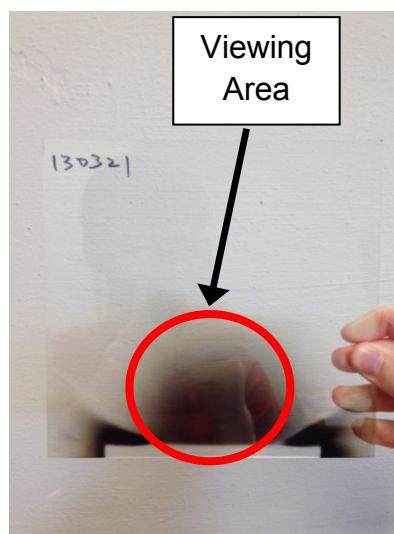
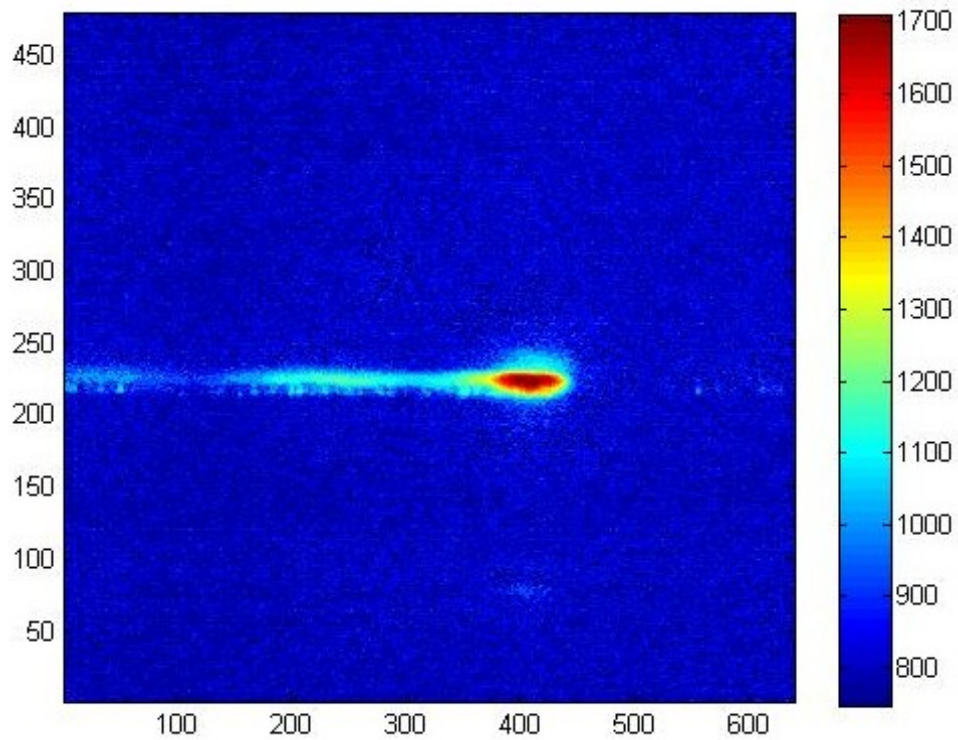
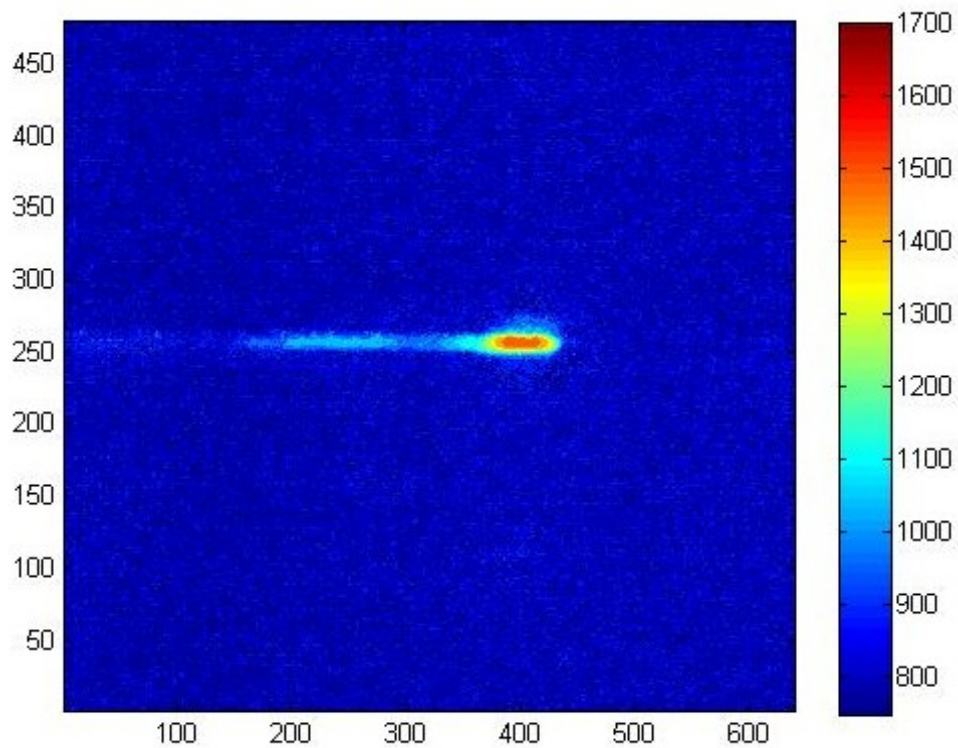


Figure 4.5. Sacrificial glass from High Exposure Experiment.



(a)



(b)

Figure 4.6. NIR images of hatch melting at build heights of (a) 25.97 mm (b) 36.19 mm from the High Exposure Experiment.

The composition of the metal film on the sacrificial glass was studied by Gong (2014) using energy dispersive X-ray spectroscopy (EDS). A working voltage of 20 kV and a working distance of 11 mm were used. The weight percentages found assuming the chemical composition of Ti-6Al-4V are shown in Table 4.1. The results show that the primary elements of the metallization were aluminum and titanium.

Table 4.1

Chemical Composition of the Metallization Found Using EDS

Element	C	N	O	Al	Ti	V
Weight %	7.81	0.88	0.52	21.10	66.47	1.22

A method of estimating the transmission loss due to metallization was developed. A light bulb with a tungsten filament was placed in view of the NIR camera and a clean sacrificial glass was placed in between the camera and the light bulb. Figure 4.7 shows the transmission loss determination experimental setup. A short video of the filament was taken with the emissivity set at 0.35 and the transmission rate set at 1.0, then the clean glass was replaced with the sacrificial glass from the experiment of interest. A short video was then taken with the same emissivity and transmission rate. The transmission rate was then reduced by 0.05 and another video was taken. This process of reducing the transmission rate and taking a video was repeated until the measured temperatures of the filament were clearly larger than what was seen through the clean glass. A Matlab code was then used to average the frames of each video together, creating a single average frame to represent each video. The code then found the temperatures of the pixels that made up the filament and averaged them together to get a single average filament temperature for each video. The measured average filament temperature for each transmission

rate was plotted and the intersection of this curve with the average filament temperature observed through the clean glass indicated the actual transmission rate of the metallization. The plot for the sacrificial glass from the High Exposure Experiment is shown in Figure 4.8. The transmission loss due to the metallization was found to be in the range of 85-90%.

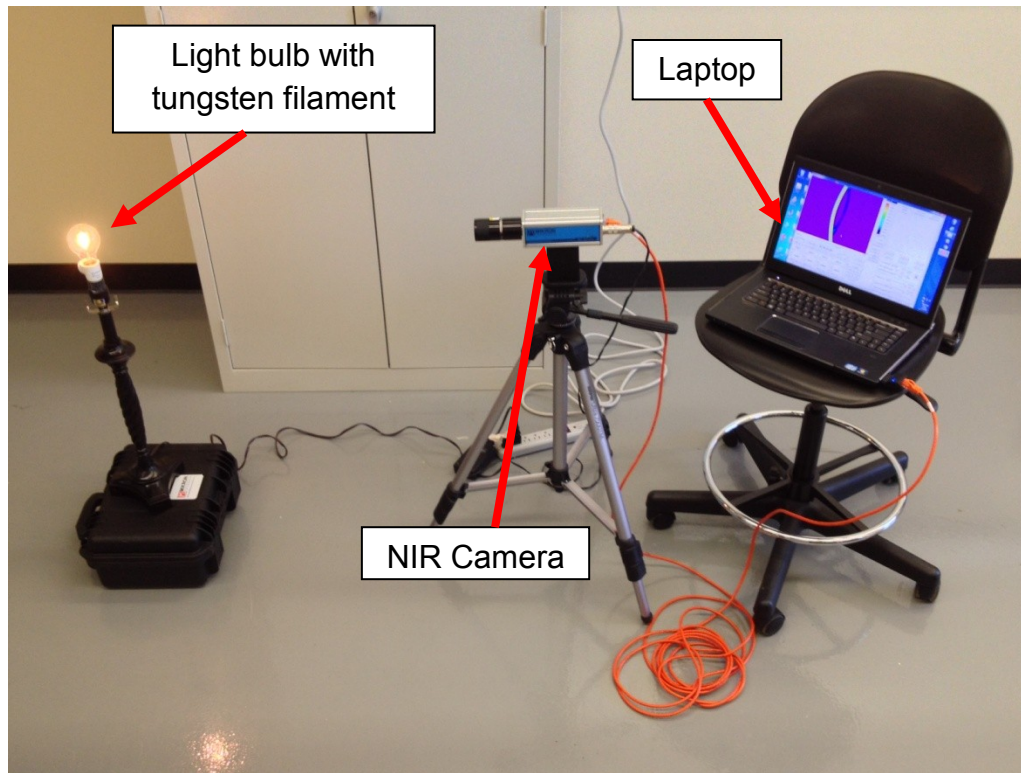


Figure 4.7. Transmission rate determination experimental setup.

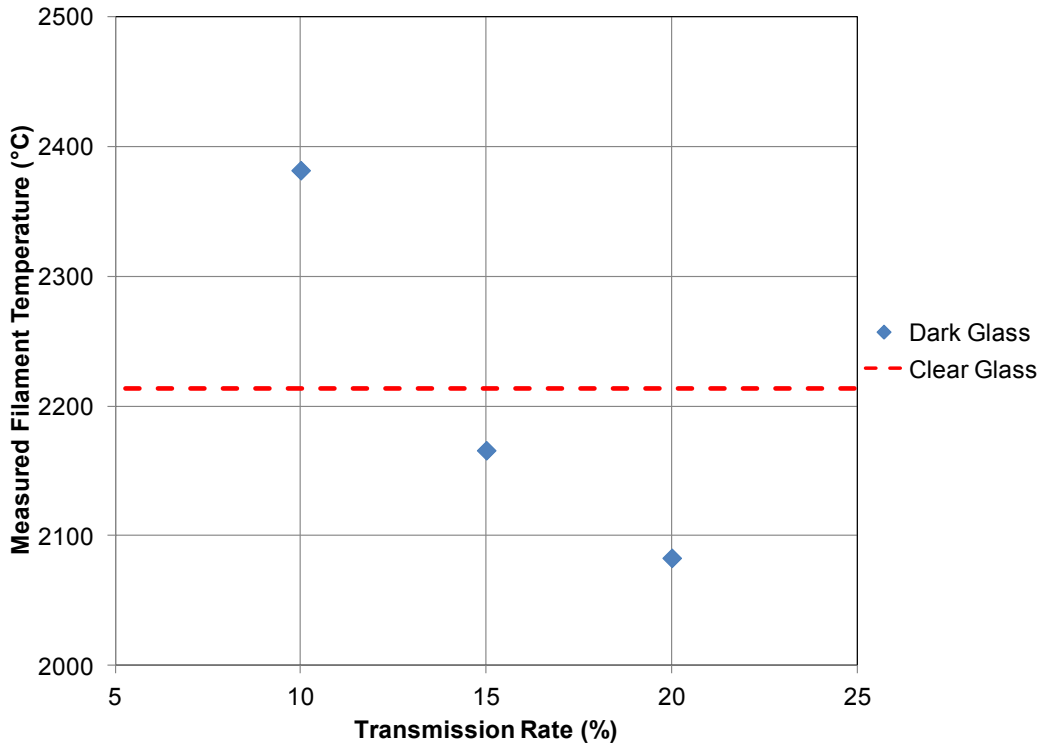


Figure 4.8. Metallization transmission rate experiment data from High Exposure Experiment.

Average two-dimensional temperature profiles of the molten pool during hatch melting were generated for several different layers. The average profiles had very large standard deviations so further investigation was conducted and it was found that the bars from the heat shield may have caused interference in the temperature measurements. The interference likely caused the temperature profiles to become distorted, leading to the high standard deviations of the average temperature profiles. Figure 4.9 shows an average temperature profile from a build height of 0.77 mm along with its standard deviations. Figure 4.10 shows average temperature profiles from various build heights. Trends of the build height effect on the temperature profiles were difficult to notice due to the large uncertainty in the measurements.

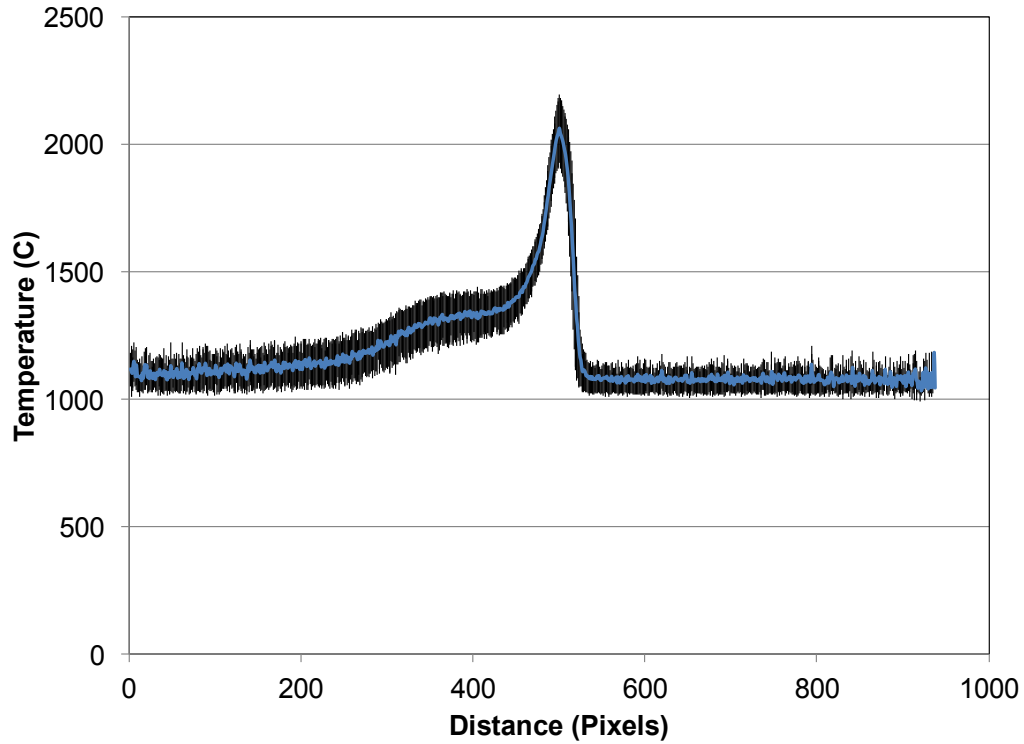


Figure 4.9. Average temperature profile with standard deviations from the High Exposure Experiment at a build height of 0.77 mm.

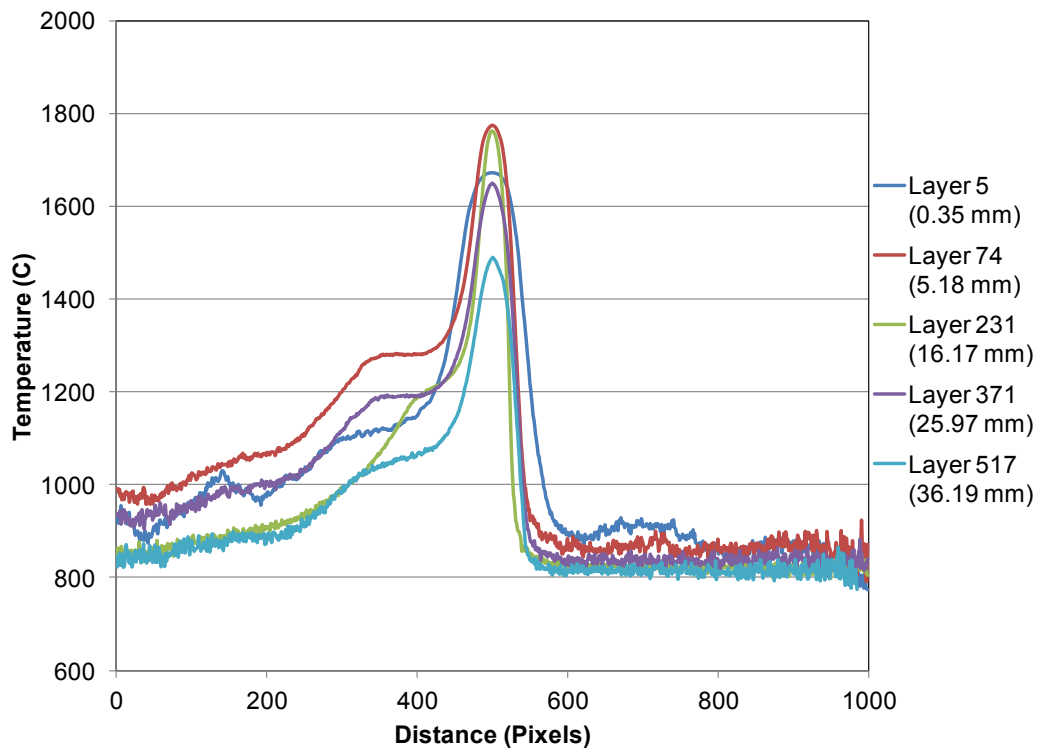


Figure 4.10. Average temperature profiles from the High Exposure Experiment at various build heights from the first build.

Limited Exposure Experiments

Based on the results from the High Exposure Experiment, several modifications to the experimental procedure were made for the Limited Exposure Experiment I. Three bars from the heat shield were cut to try to provide an unobstructed view of the build surface. Thirty-four NIR videos were made, but their length was shortened to around 10-15 seconds each, which cut the exposure time to almost to half of what was experienced in the High Exposure Experiment. As seen below in Figure 4.11, the metallization on the sacrificial glass was much less severe than what was seen in the High Exposure Experiment. The transmission rate was determined using the same experimental procedure described in the High Exposure Experiment section. Figure 4.12 shows the results of the metallization transmission rate experiment. The transmission loss due to the metallization was found to be in the range of 20-25%. Figure 4.13 shows an example NIR image of hatch melting taken at a build height of 20.93 mm (299 layers).

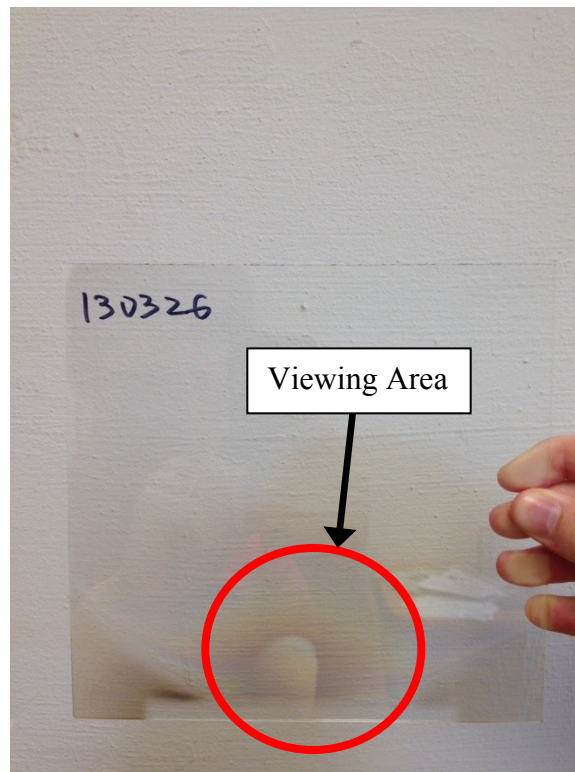


Figure 4.11. Sacrificial glass from Limited Exposure Experiment I.

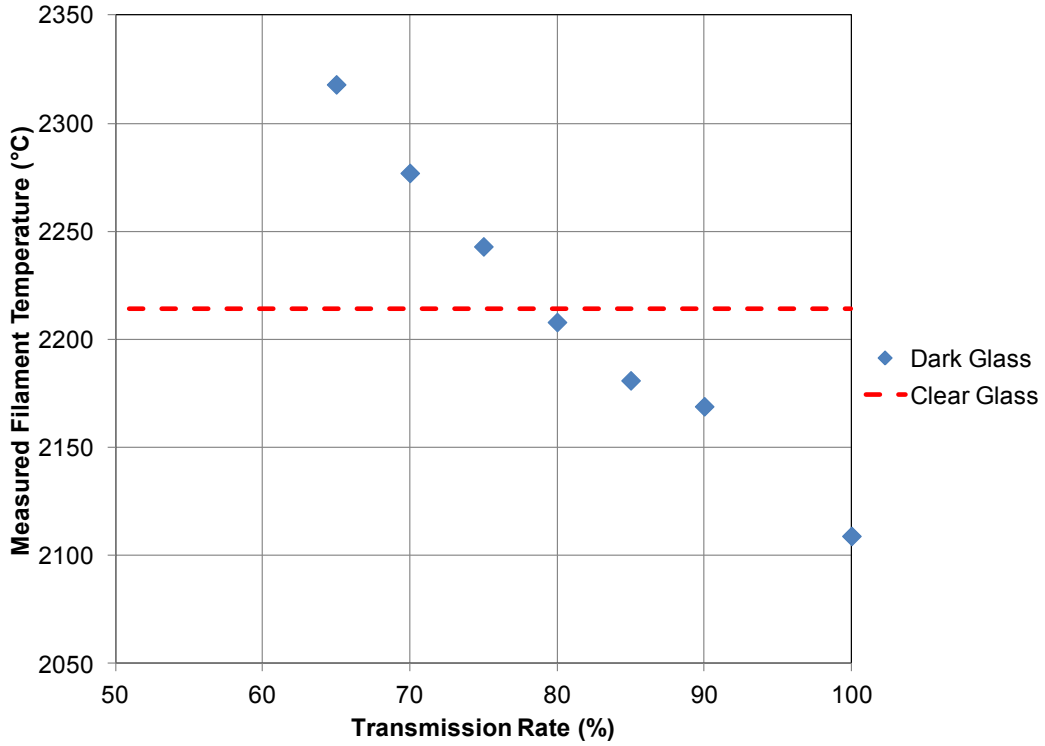


Figure 4.12. Metallization transmission rate experiment data from Limited Exposure Experiment I.

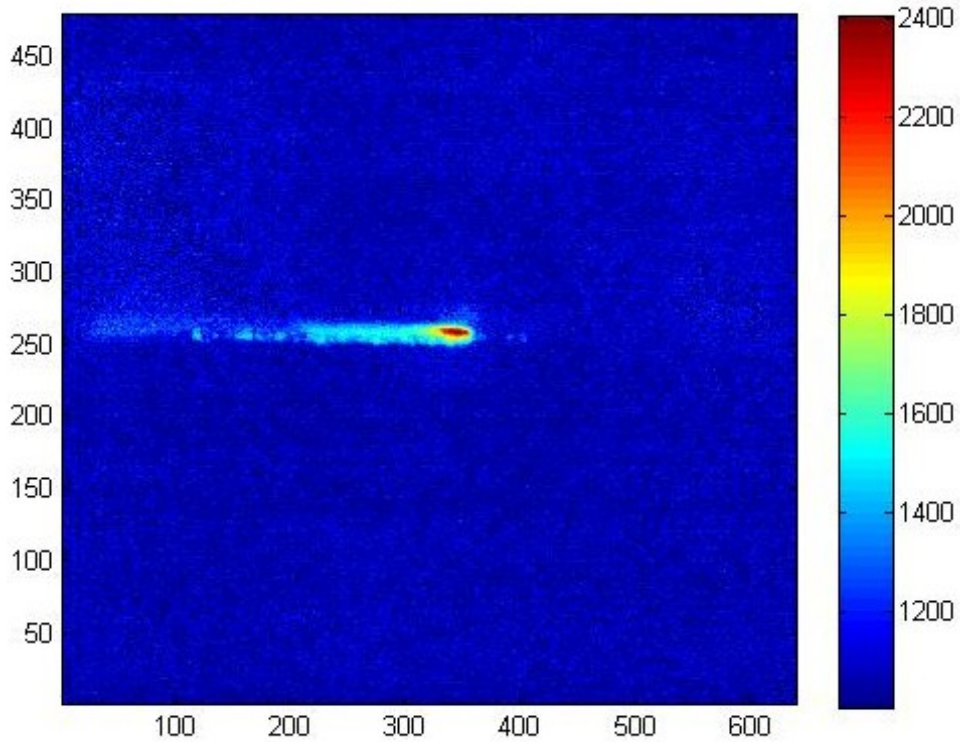


Figure 4.13. NIR image of hatch melting at a build height of 20.93 mm from Limited Exposure Experiment I.

Figure 4.14 shows a single average temperature profile with standard deviations from Limited Exposure Experiment I. The standard deviations are not as large as what was seen in the High Exposure Experiment because there was a smaller amount of interference from the heat shield. Figure 4.15 compares three average temperature profiles from layers that were located close to one another. The similarity of the profiles to one another shows that the repeatability of the temperature measurements is very high. Figure 4.16 compares average temperature profiles from a wider range of layers. With the exception of layer 299, the average measured peak temperatures decreased with build height. This was likely due mainly to transmission losses caused by metallization that occurred during the build. The length of the phase transition region of the cooling side of the curve reduced noticeably by around 2 mm between the build heights of 1.75 mm and 4.97 mm. This effect is believed to have been caused by changes in the beam speed and current that occurred during the fabrication of the first several millimeters of the part.

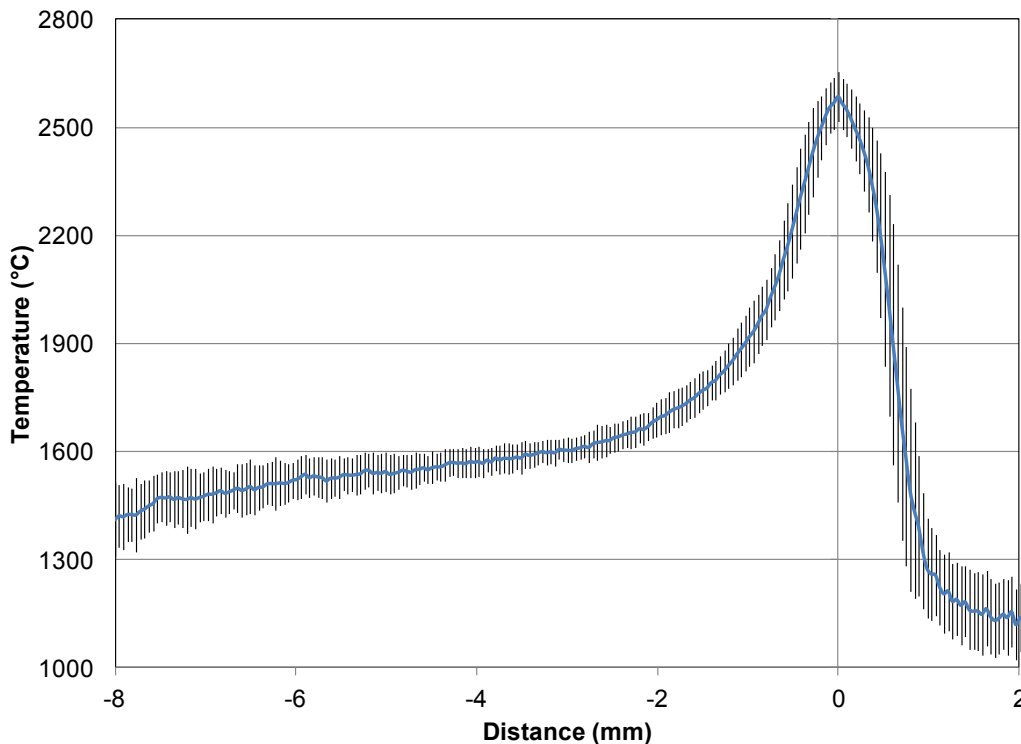


Figure 4.14. Average temperature profile with standard deviations from Limited Exposure Experiment I at a build height of 1.33 mm.

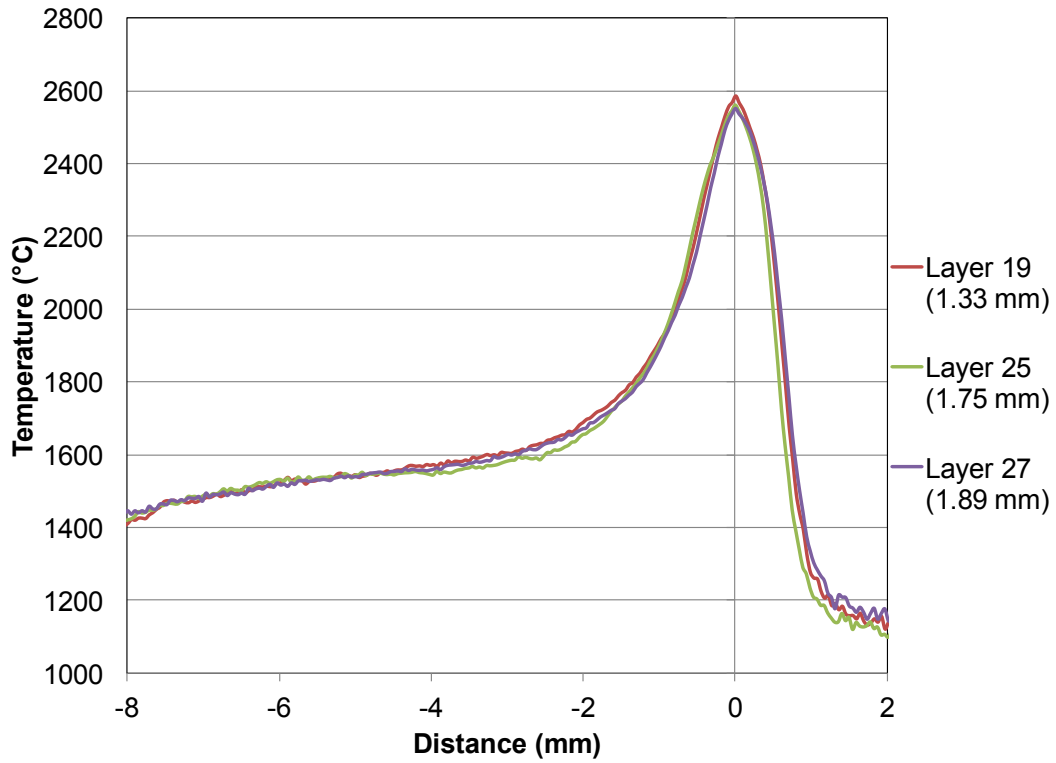


Figure 4.15. Average temperature profiles from Limited Exposure Experiment I that are within 9 layers of each other.

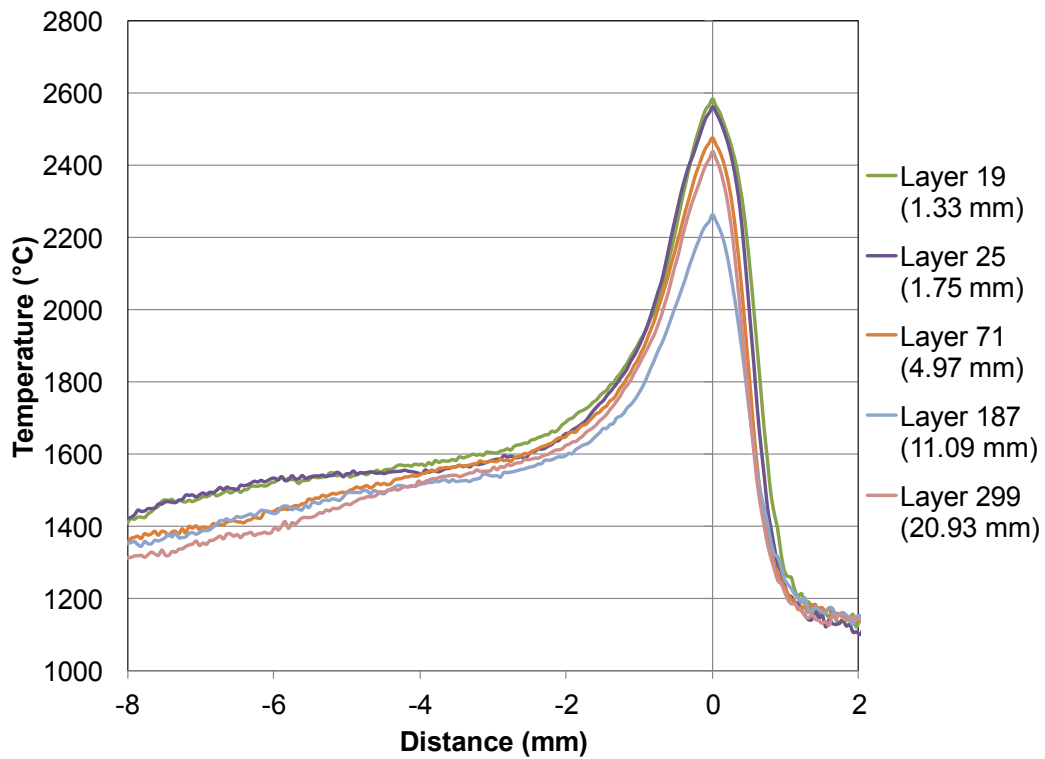


Figure 4.16. Average temperature profiles from Limited Exposure Experiment I at various build heights.

The size and shape of the molten pool are of interest because of their effects on the final properties and dimensional accuracy of the part. Ideally the true liquidus temperature of Ti-6Al-4V (1655 °C) could be used to identify the boundary of the molten pool, however, because of the uncertainty of the temperature measurements caused by transmission loss and estimated emissivity, this method would be inaccurate. Because the use of the true liquidus temperature was not possible, another method was developed that enabled an estimation of molten pool length and width. The temperature versus time graph of Ti-6Al-4V cooling during a casting process shown by Suzuki and Yao (2004) in Figure 4.17 shows how the cooling rate decreases during the phase transition region between the liquidus and solidus temperatures, then increases again once the solidus temperature is reached. Although the 2D temperature profiles generated from the NIR images are spatial temperature profiles, they can be converted to temperature versus time curves if the beam speed is known. Figure 4.18 shows a spatial temperature profile that has been converted to a temperature versus time curve. With the time scales adjusted it can be seen that the shape of the curve is very similar to the cooling curve in Figure 4.17.

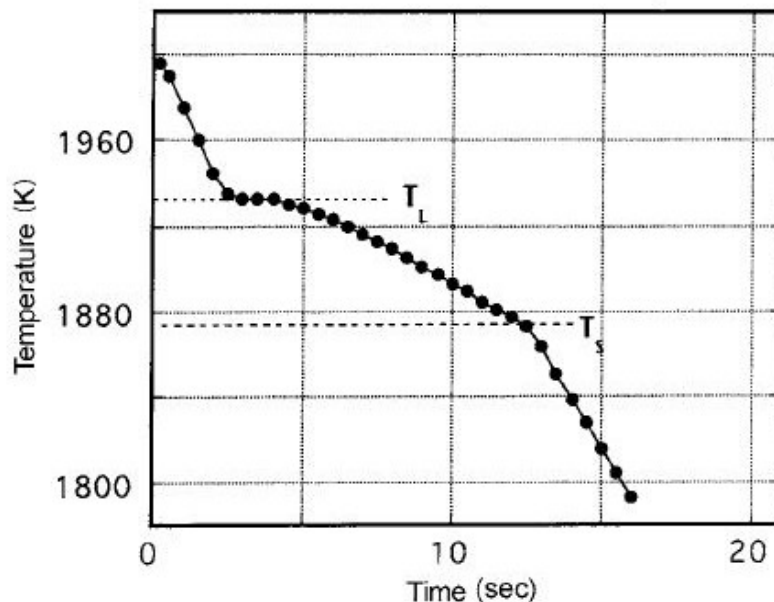


Figure 4.17. Identification of liquidus and solidus temperatures on a temperature vs. time graph of Ti-6Al-4V cooling during a casting process (Suzuki & Yao, 2004).

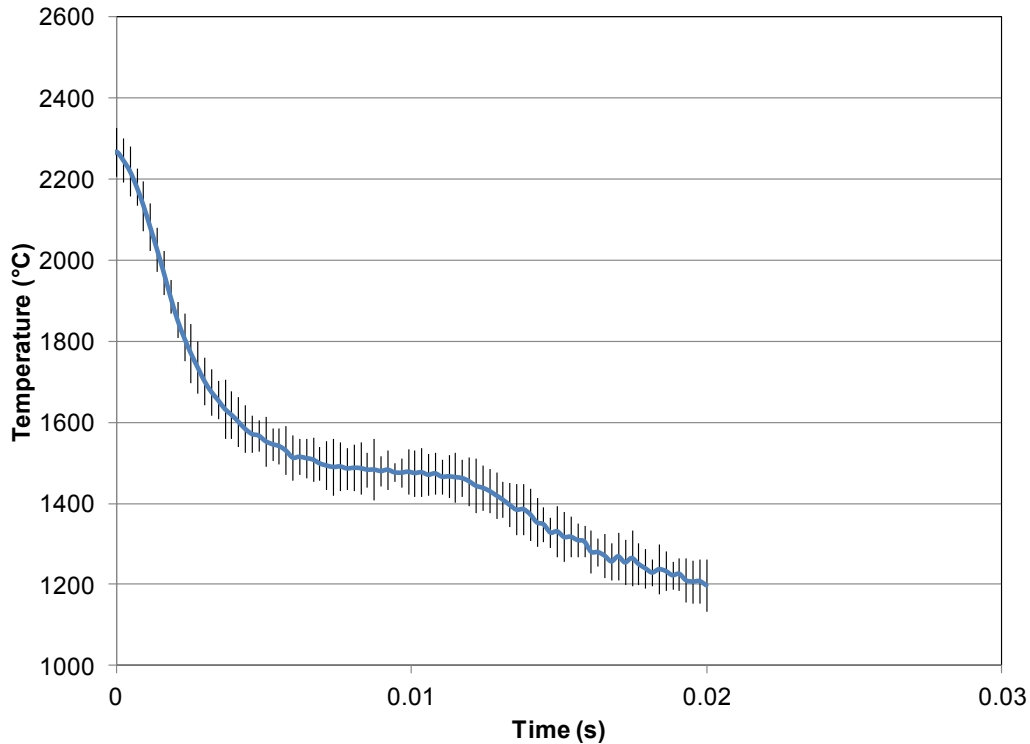


Figure 4.18. Example temperature versus time curve created from a spatial temperature profile.

Examination of the shape of a 2D temperature profile generated from an NIR image of hatch melting allows for an estimation of the location of the liquidus temperature. The leading edge of the temperature profile shows extreme heating followed by extreme cooling. The cooling rate decreases sharply once the liquidus temperature is reached. Once the solidus temperature has been reached, the cooling rate increases again. So by examination of a 2D temperature profile, the measured liquidus temperature was estimated and subsequently used to determine the average molten pool length and width. The distance between the liquidus temperatures on the heating and cooling sides of the average temperature profile along the scanning path was used to determine the average molten pool length. The standard deviation of the liquidus temperature was added to the liquidus temperature and the length was recalculated. The difference between this length and the average length was reported as the standard deviation of the length. Symmetry of this standard deviation was assumed because the low slope of the

phase transition region caused the standard deviation in the downward direction to appear much larger than reasonable. Figure 4.19 shows example average temperature profiles in the scanning and transverse directions in which the measured liquidus temperature was identified as 1595 °C. The solid lines indicate the average length and width and the dashed lines represent the lengths at the standard deviations of the liquidus temperature. The average molten pool dimensions were calculated at various build heights and the results are presented in Figure 4.20. Both the average molten pool length and width seem to be relatively stable over the range of build heights studied, however, the larger size of the standard deviations of the average molten pool lengths seems to indicate that the molten pool length fluctuated during each layer fabrication. The grand means of the average molten pool lengths and widths were 3.14 mm and 0.88 mm with standard deviations of 0.22 mm and 0.11 mm respectively.

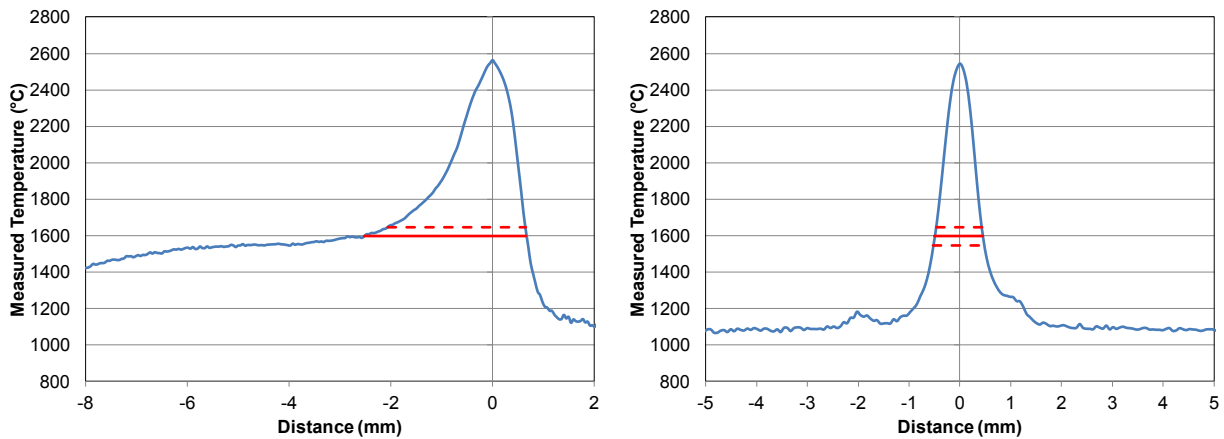


Figure 4.19. 2D average temperature profiles in the (a) scanning and (b) transverse directions from Limited Exposure Experiment I at a build height of 1.75 mm showing the locations of the average measured liquidus temperature.

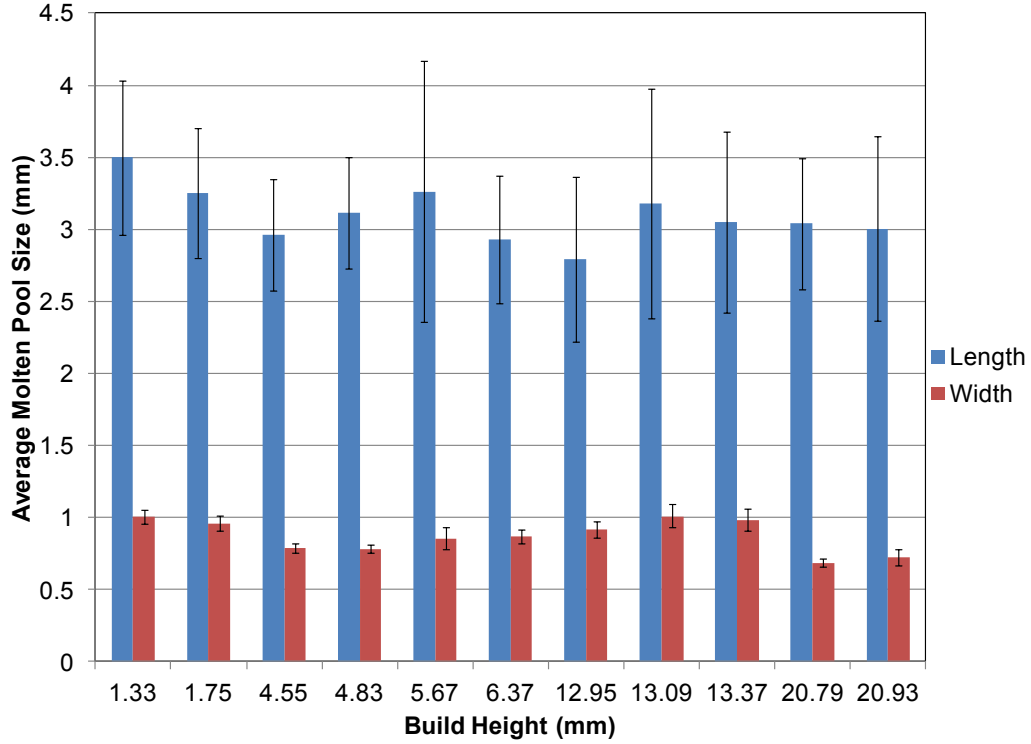


Figure 4.20. Average molten pool dimensions from Limited Exposure Experiment I.

The true emissivity of the molten pool was a parameter of interest due to its impact on the NIR temperature measurements. A method was developed to estimate the molten pool emissivity based on the NIR temperature results. As discussed earlier, the measured value of the liquidus temperature can be identified from a 2D temperature profile of the molten pool. Since the true value of Ti-6Al-4V's liquidus temperature is both constant and known, it is possible to determine what emissivity would give the true liquidus temperature. Equation 7 from Whitenton (2010) was used to calculate the emissivity:

$$M = \left[\int_{\lambda_1}^{\lambda_2} \frac{w_\lambda}{\lambda^5 \left(\frac{c_2}{e^{\lambda T_{app}} - 1} \right)} d\lambda \right] - \left[\varepsilon \int_{\lambda_1}^{\lambda_2} \frac{w_\lambda}{\lambda^5 \left(\frac{c_2}{e^{\lambda T_{true}} - 1} \right)} d\lambda \right] - \left[(1 - \varepsilon) \int_{\lambda_1}^{\lambda_2} \frac{w_\lambda}{\lambda^5 \left(\frac{c_2}{e^{\lambda T_{envir}} - 1} \right)} d\lambda \right] \quad (7)$$

where,

M = variable to minimize by adjusting other variables,

λ_1 = bottom of infrared camera's spectral range in μm ,

λ_2 = top of infrared camera's spectral range in μm ,
 λ = wavelength of light in μm ,
 w_λ = relative sensitivity of camera at wavelength λ ,
 c_2 = second radiation constant ($14388 \mu\text{m}\cdot\text{K}$),
 T_{app} = apparent temperature in K,
 T_{true} = true temperature in K,
 T_{envir} = surrounding environment temperature in K, and
 ε = emissivity.

The measured liquidus temperature was used as the true temperature and the assumed emissivity value input into the camera was used as the emissivity. The relative sensitivity of the camera at λ , w_λ , was assumed to be one because this information was not available from the camera manufacturer. The surrounding environment temperature was assumed to be room temperature. The equation was numerically solved for a range of apparent temperatures. The apparent temperature that resulted in the smallest value of M was the correct value. Next, using the calculated apparent temperature for the apparent temperature and the true liquidus temperature of Ti-6Al-4V for the true temperature, the equation was numerically solved again, this time solving for the emissivity that resulted in the smallest value of M. This emissivity was the true emissivity of the molten pool. The average molten pool emissivities calculated from Limited Exposure Experiment I are shown in Figure 4.21. The grand mean of the average emissivities was found to be 0.283 and the standard deviation was 0.018.

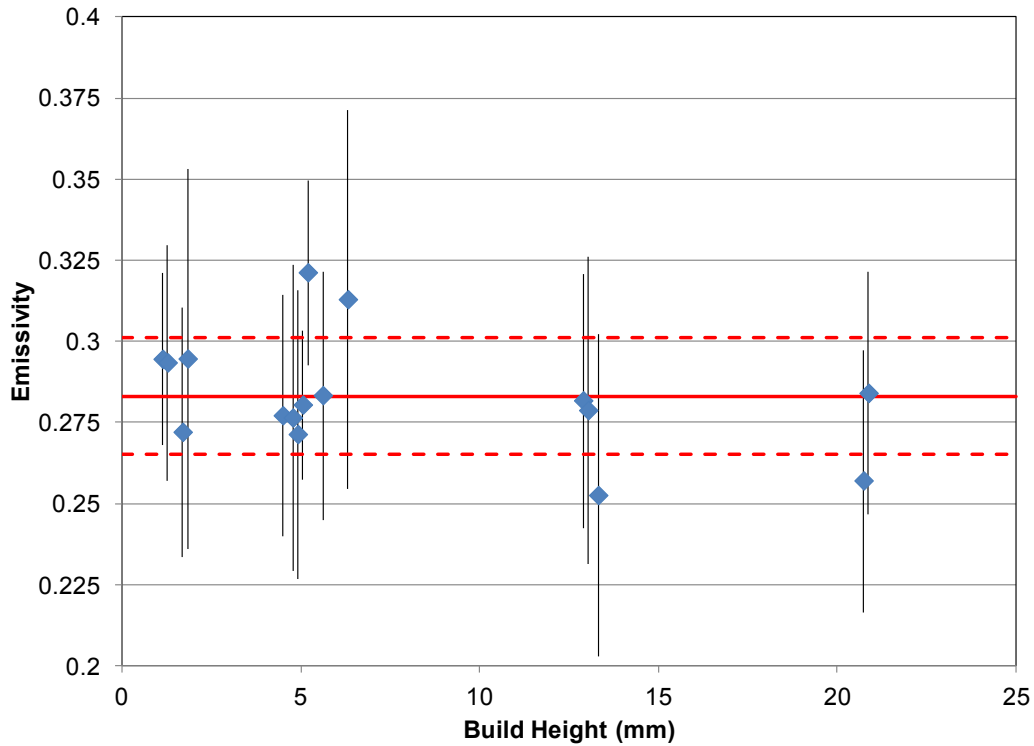


Figure 4.21. Average molten pool emissivities from Limited Exposure Experiment I.

In Limited Exposure Experiment II, five heat shield bars were cut in order to ensure that no bars would be visible in the NIR images. The metallization experienced during this experiment was a little worse than what occurred during Limited Exposure Experiment I. An image of the sacrificial glass from the experiment is shown in Figure 4.22 and the results of the transmission rate testing of the metallization are shown in Figure 4.23. The transmission loss due to the metallization was calculated to be between 35-40%.

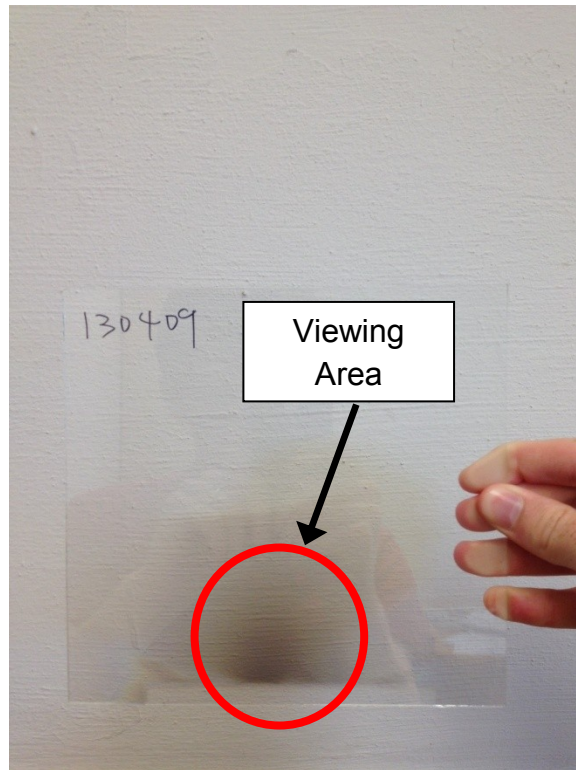


Figure 4.22. Sacrificial glass from Limited Exposure Experiment II.

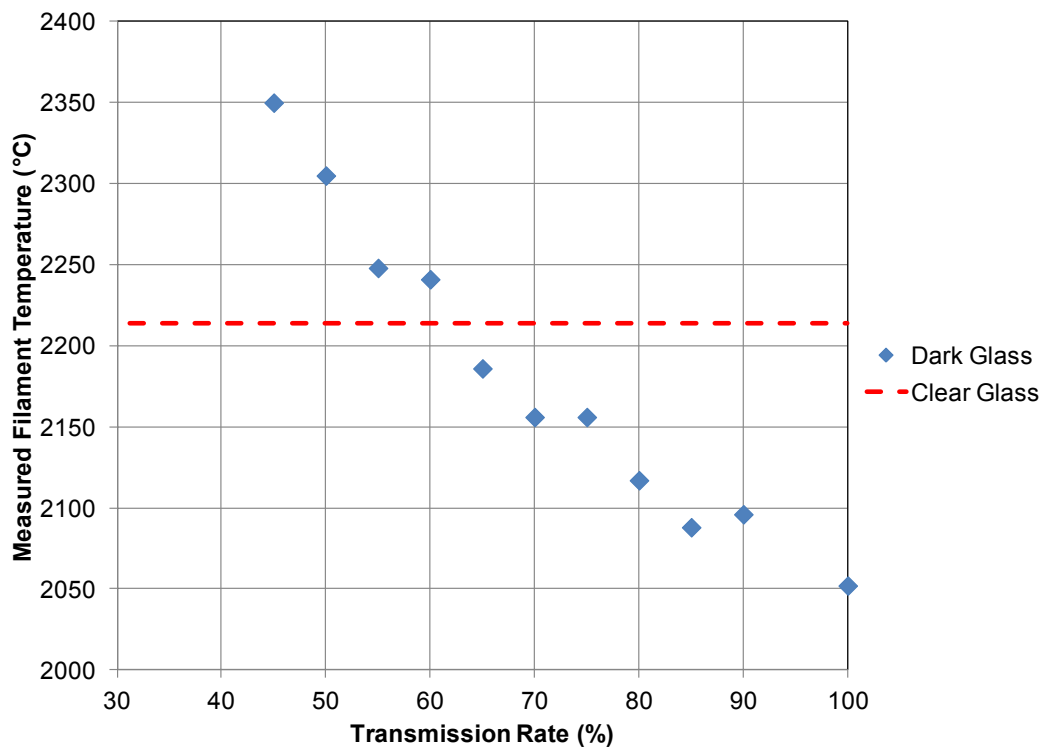


Figure 4.23. Metallization transmission rate experiment data from Limited Exposure Experiment II.

Figure 4.24 shows average temperature profiles from a variety of build heights. The measured peak temperatures decreased with build height as did the length of the phase transition region. The rate that these changes occurred appeared to decrease after the first few millimeters of the build were completed. The molten pool dimensions were determined using the procedure described in the previous section and the results are shown in Figure 4.25. The grand means of the molten pool length and width were 3.84 mm and 0.91 mm respectively with standard deviations of 0.22 mm and 0.08 mm. The average molten pool length began to decrease after about 1.5 mm of build height had been completed. Mahale (2009) found that both the beam speed and current start at high values and then quickly drop to almost steady state values after several millimeters of the part are built. Therefore, it is possible that the different process parameters at the beginning of the build were the cause of the initial change in molten pool dimensions. The average molten pool emissivity was calculated at a range of build heights as well and the grand mean was 0.211 and the standard deviation was 0.032. The calculated emissivities are shown in Figure 4.26. An important observation made from the emissivity results was that the value of the calculated emissivity decreased sharply early in the build similar to how the molten pool dimensions decreased. It was assumed that the decrease in calculated emissivity at the beginning of the build was due to transmission loss from the metallization forming on the sacrificial glass. The emissivity calculation assumes that the difference between the measured and true liquidus temperatures is completely due to incorrect assumed emissivity. Therefore, at the higher layers of the build when the transmission loss was greater, the emissivity calculation was more severely affected.

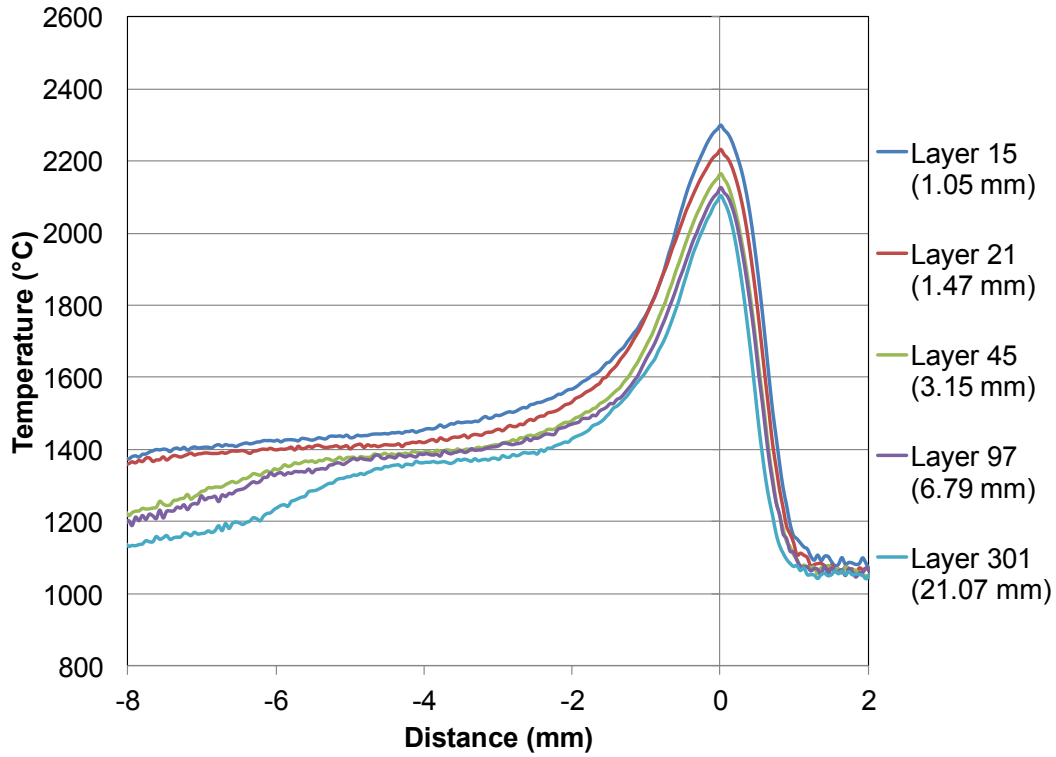


Figure 4.24. Average temperature profiles from Limited Exposure Experiment II at a variety of build heights.

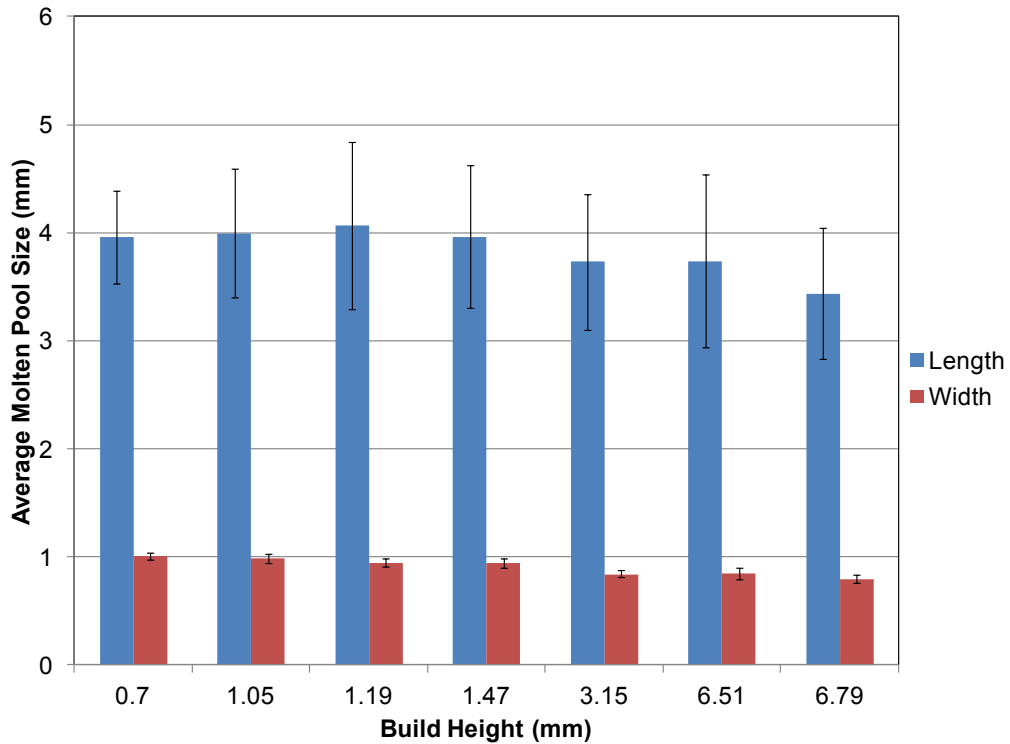


Figure 4.25. Average molten pool dimensions from Limited Exposure Experiment II.

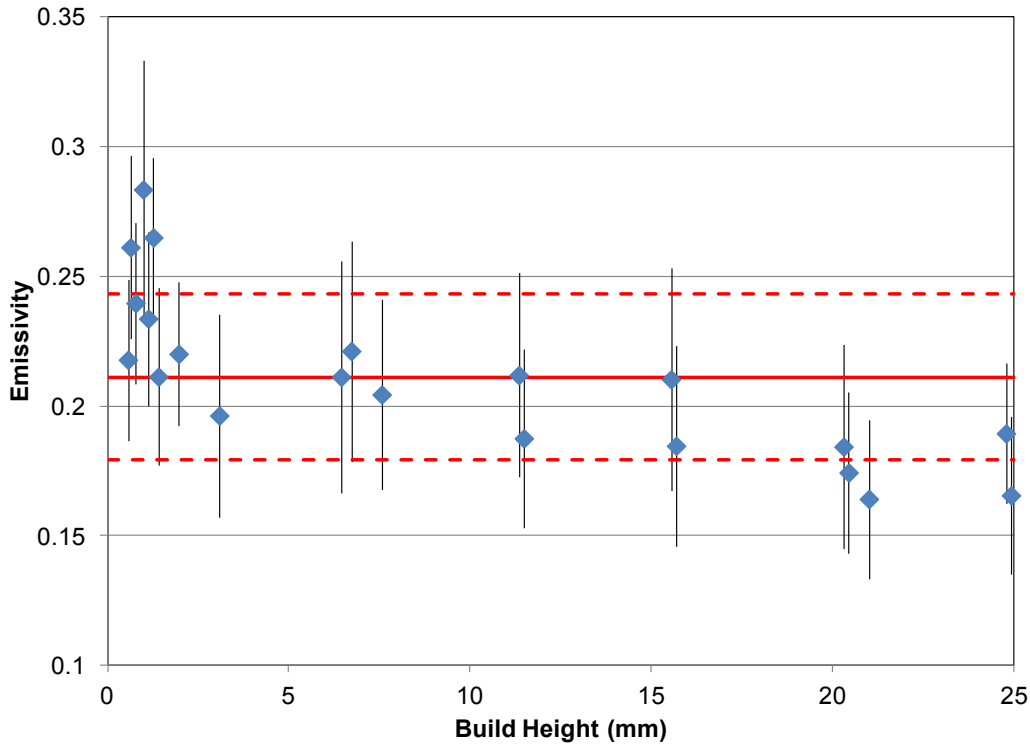


Figure 4.26. Average molten pool emissivities from Limited Exposure Experiment II.

Controlled Exposure Experiment

After seeing the impact of the metallization on the temperature measurements from the previous experiments it was decided to investigate the effects of metallization more thoroughly. An experimental procedure that required two builds was developed that would cause the sacrificial glass to have two different levels of metallization during the second build. A comparison of the measured temperatures of the molten pool as observed through both levels of metallization allowed the effects of the metallization on temperature measurements to be studied.

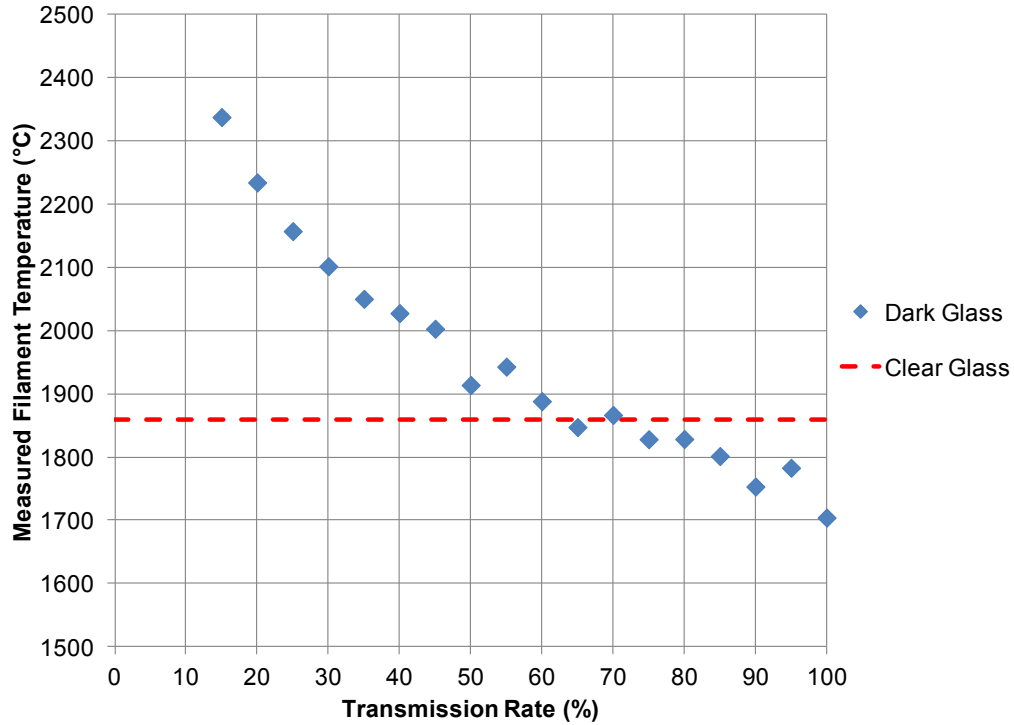
During the first build of this experiment, the left half of the sacrificial glass was covered with a plastic protective film to protect it from metallization and a part was fabricated. Ten videos were taken during this build at various heights. When the build was completed the transmission loss due to the metallization was determined, then the protective film was removed from the left side of the glass and it was returned to the machine. A second build was conducted

and eight videos were taken. After the build was completed, the transmission loss due to the metallization was determined for both sides of the glass. Two average temperature profiles were generated for each layer that was imaged, one from each side of the glass. These profiles were then compared to see the effects of the different levels of metallization. Figure 4.27 shows the sacrificial glass after the second build with two levels of metallization.

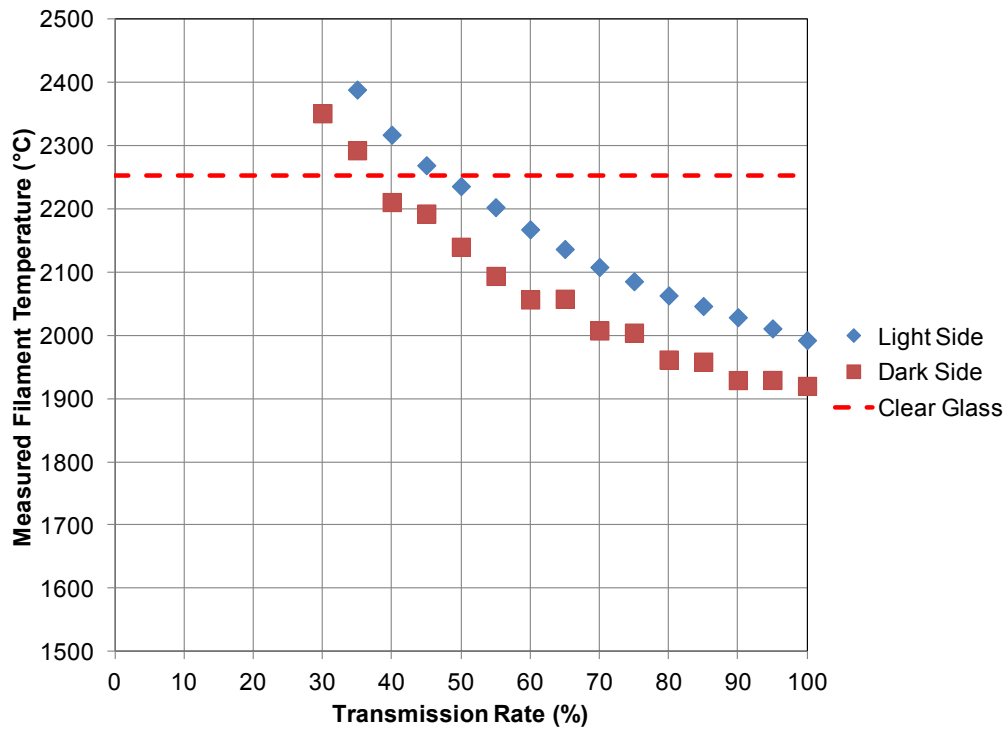


Figure 4.27. Sacrificial glass from Controlled Exposure Experiment with two levels of metallization.

The transmission losses due to metallization were calculated and the results are shown in Figure 4.28. The transmission loss due to metallization after the first build was between 30-40%. The transmission loss of the dark side of the glass after the second build was between 60-65% and the transmission loss of the light side of the glass was between 50-55%.



(a) First build



(b) Second Build

Figure 4.28. Transmission rate determination from the (a) first and (b) second builds of the Controlled Exposure Experiment.

The spatial resolutions of the NIR images were determined for both experiments and the plots used for the analysis are shown in Figure 4.29. The horizontal resolutions of the two experiments were found to be 40.7 and 41.2 $\mu\text{m}/\text{pixel}$ and the vertical resolutions were 65.3 and 62.5 $\mu\text{m}/\text{pixel}$ respectively.

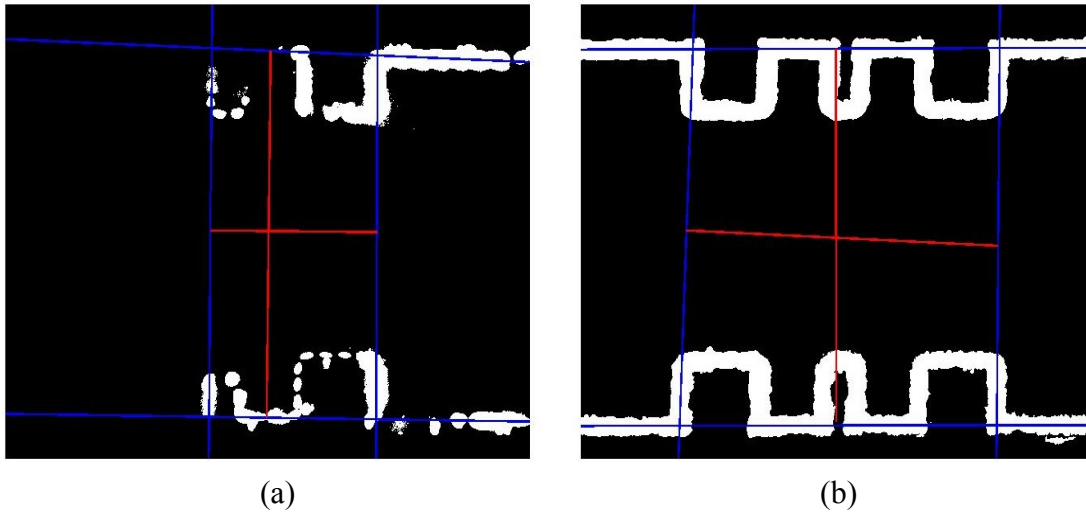


Figure 4.29. Contour melting data from the (a) first and (b) second builds of the Controlled Exposure Experiment used for spatial resolution analysis.

Average temperature profiles were calculated from both builds. The profiles from the second build are of particular interest because of the two dual transmission rates of the sacrificial glass. This enabled a comparison of the temperature profiles observed under different transmission rates. The average temperature profiles from the builds are shown in Figures 4.30 and 4.31. The average temperature profiles from both builds show similar trends to what was observed during the Limited Exposure Experiments. The measured peak temperature and length of the phase transition region both decreased with build height. The rate that the phase transition length shortens began to decrease quickly after the first 10-15 mm of the part was built. Comparison of the average temperature profiles from an individual layer of the second build in Figure 4.32 shows the effect that smaller transmission rates had on the temperature profiles. The molten pools viewed through the darker side of the glass appeared cooler than the molten pools

viewed through the lighter side of the glass. The difference was more significant at the higher temperatures of the profiles.

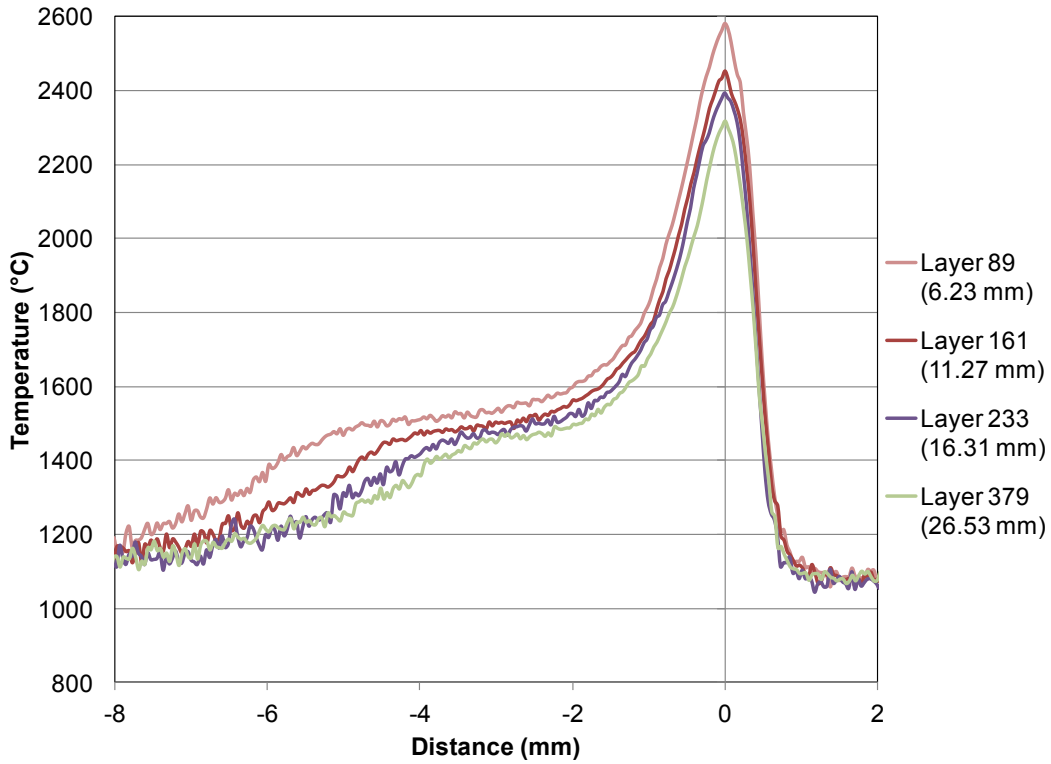
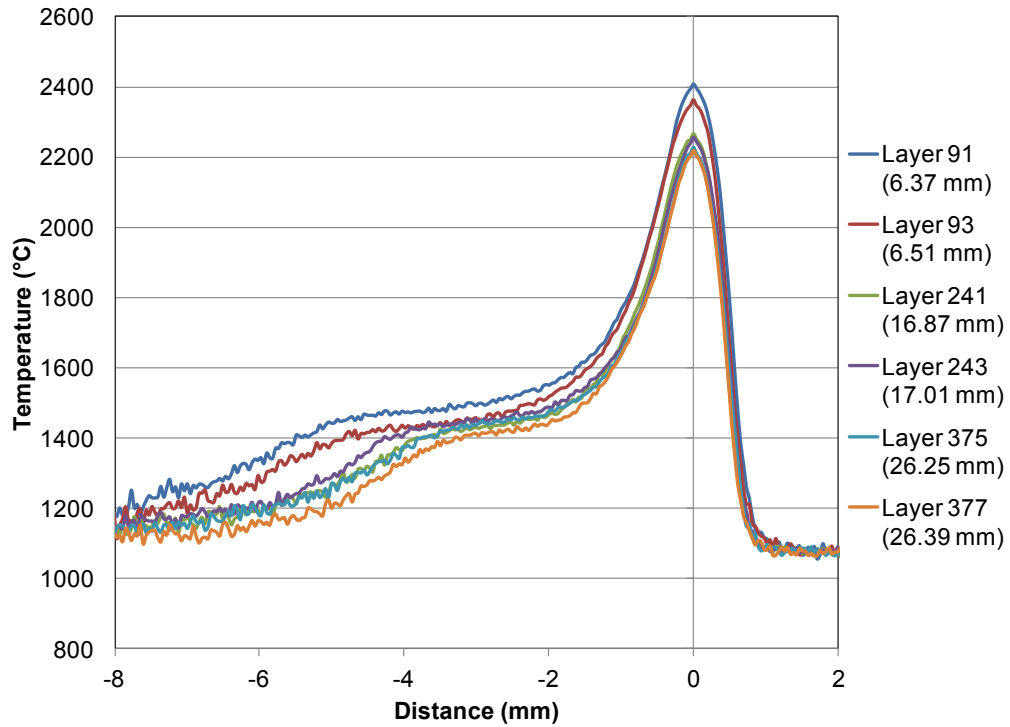
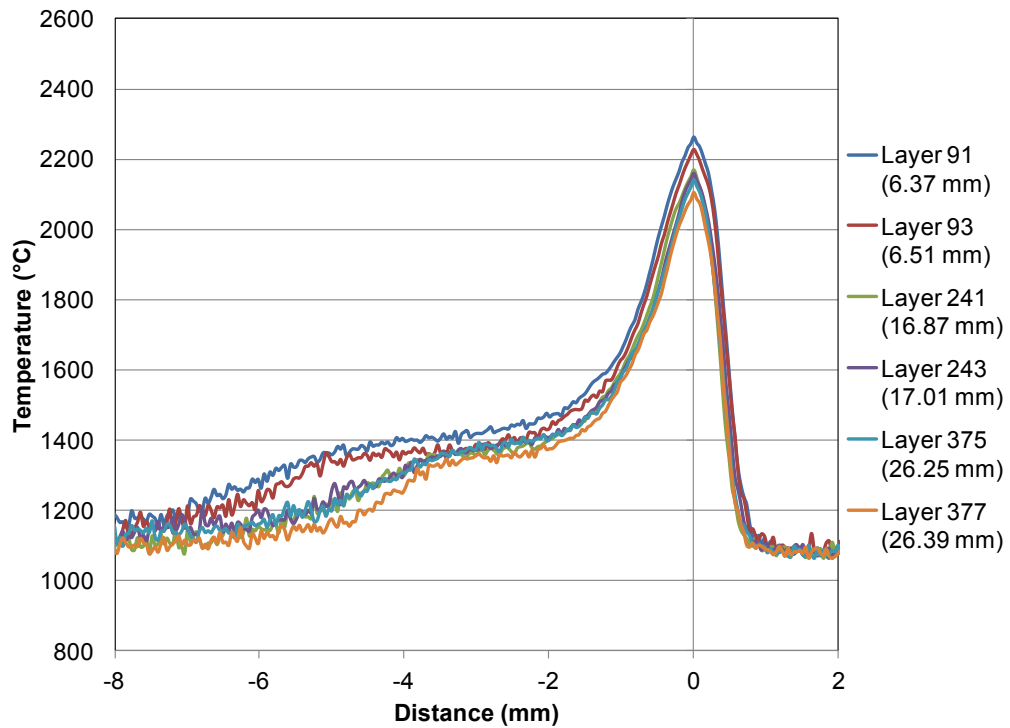


Figure 4.30. Average temperature profiles from the first build of the Controlled Exposure Experiment.

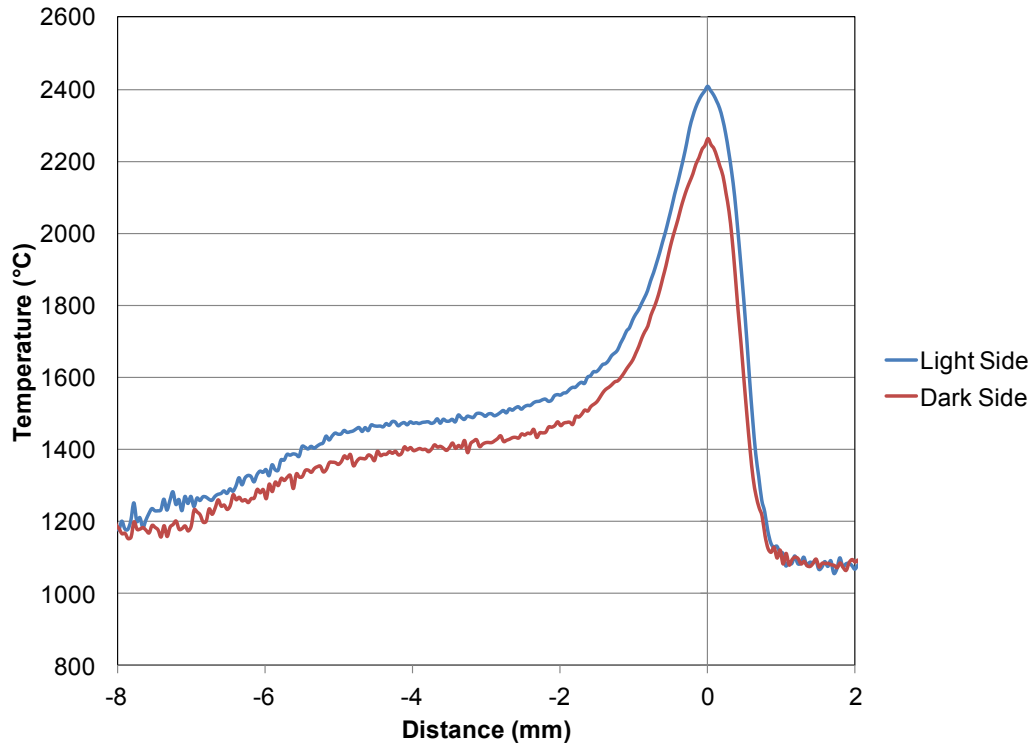


(a) Lighter Side

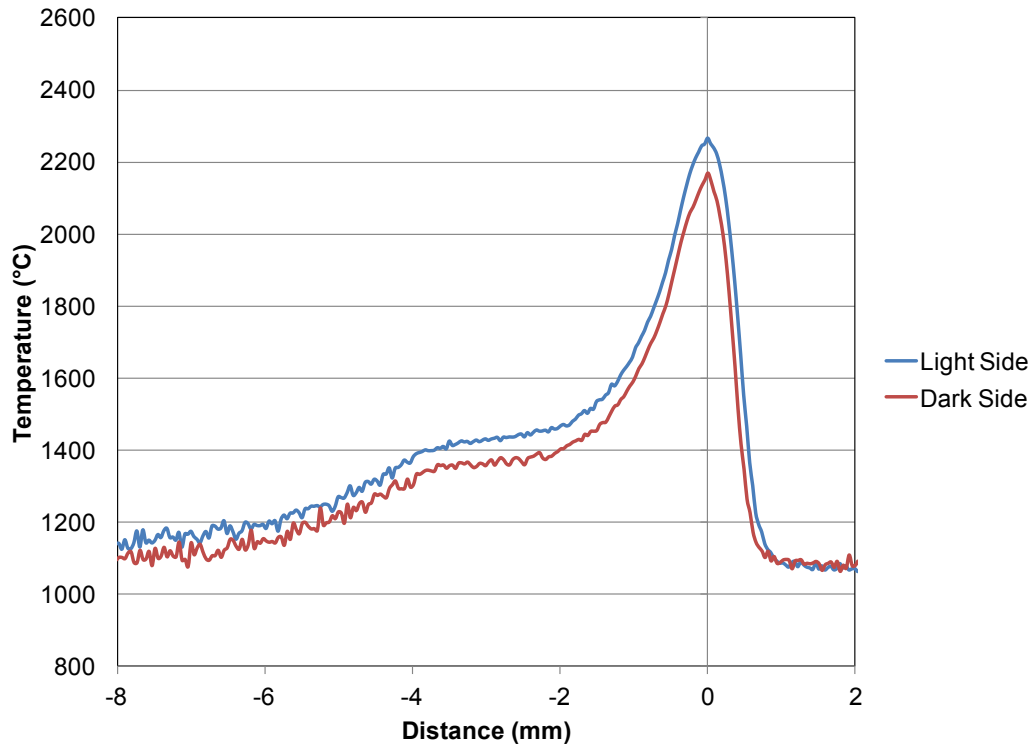


(b) Darker Side

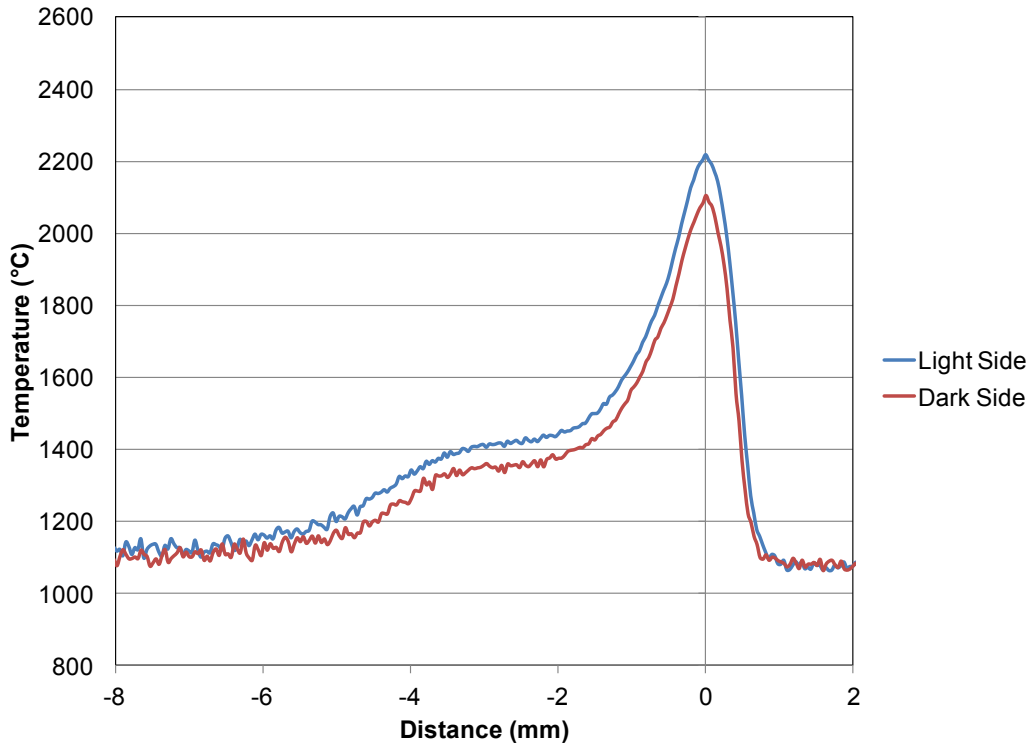
Figure 4.31. Average temperatures observed through the (a) lighter and (b) darker sides of the sacrificial glass from the second build of the Controlled Exposure Experiment.



(a) 6.37 mm



(b) 16.87 mm



(c) 26.39 mm

Figure 4.32. Average temperature profile comparisons from the second build of the Controlled Exposure Experiment at build heights of (a) 6.37 mm, (b) 16.87 mm, and (c) 26.39 mm.

The relationship between the temperatures observed at different transmission rates was investigated in order to study the effect of the metallization on the temperature measurements. The temperatures from the two average temperature profiles from the same layer, but different transmission rates were correlated to each other by their position on the average temperature profile and then plotted from coldest to hottest. Figure 4.33 shows that there is a linear relationship between the darker and lighter side temperatures at a build height of 6.37 mm from the second build. The trend shows that the higher temperatures are more significantly attenuated by the metallization. This trend was determined at other build heights as well and the relationship was found to be repeatable.

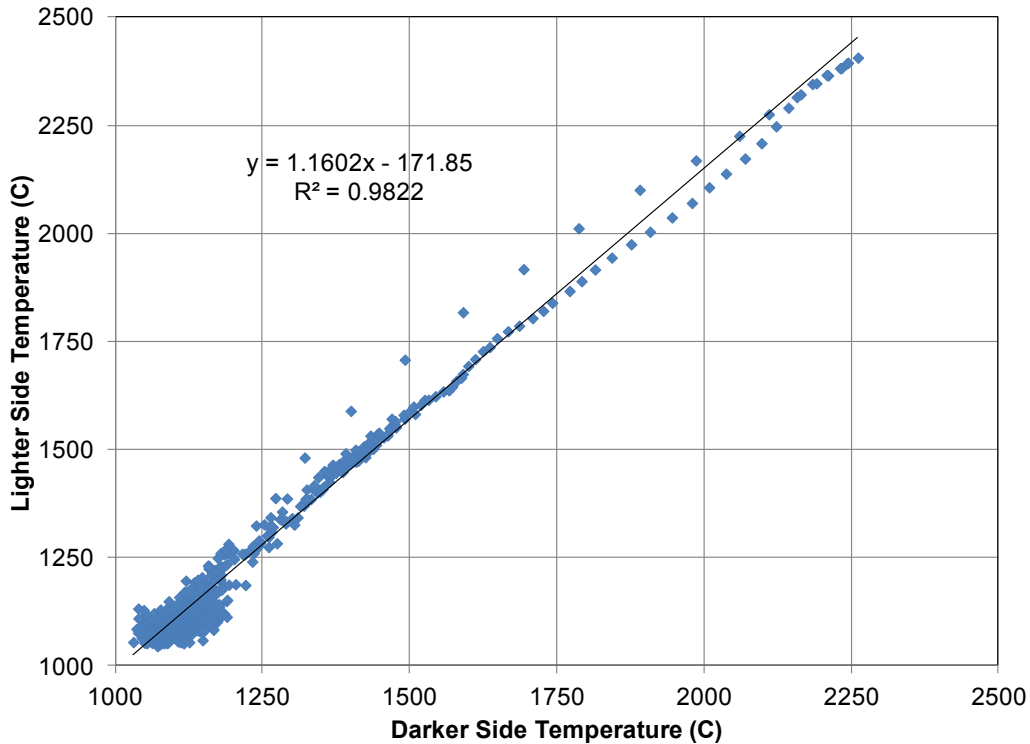


Figure 4.33. Relationship between temperatures observed through the lighter and darker sides of the sacrificial glass from the second build of the Controlled Exposure Experiment at a build height of 6.37 mm.

Since transmission loss was found to affect the temperatures linearly, a method for compensating the temperature profiles for the transmission loss was able to be developed. By assuming the emissivity of the molten pool should be 0.28, a slope was calculated that would convert the measured liquidus temperature to the temperature that would result in a calculated emissivity of 0.28. This slope was found at various build heights from the first build of the Controlled Exposure Experiment and the results are shown in Figure 4.34. After a temperature profile had been compensated for transmission loss, the true emissivity of the molten pool could be estimated and then used to convert the whole temperature profile. Figure 4.35 shows an original average temperature profile from the first build of the Controlled Exposure Experiment before and after transmission loss compensation as well as after emissivity compensation. Fully

compensated profiles from a variety of build heights are shown in Figure 4.36. The original profiles may be referenced from Figure 4.30.

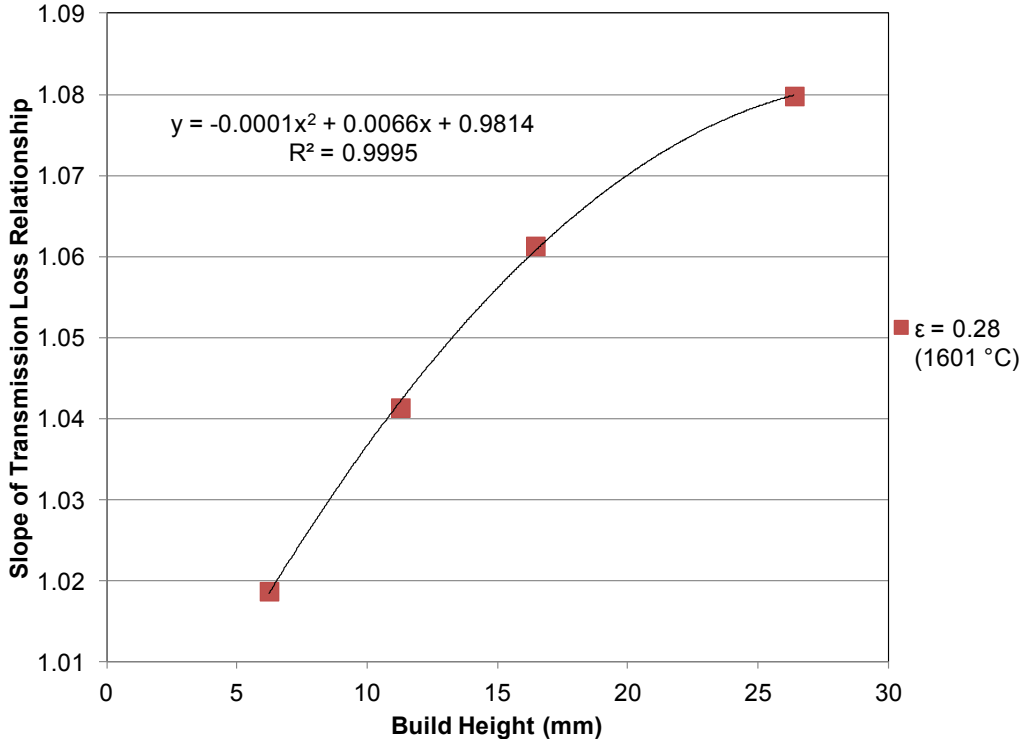


Figure 4.34. Slope of transmission loss relationship at different build heights from first build of the Controlled Exposure Experiment.

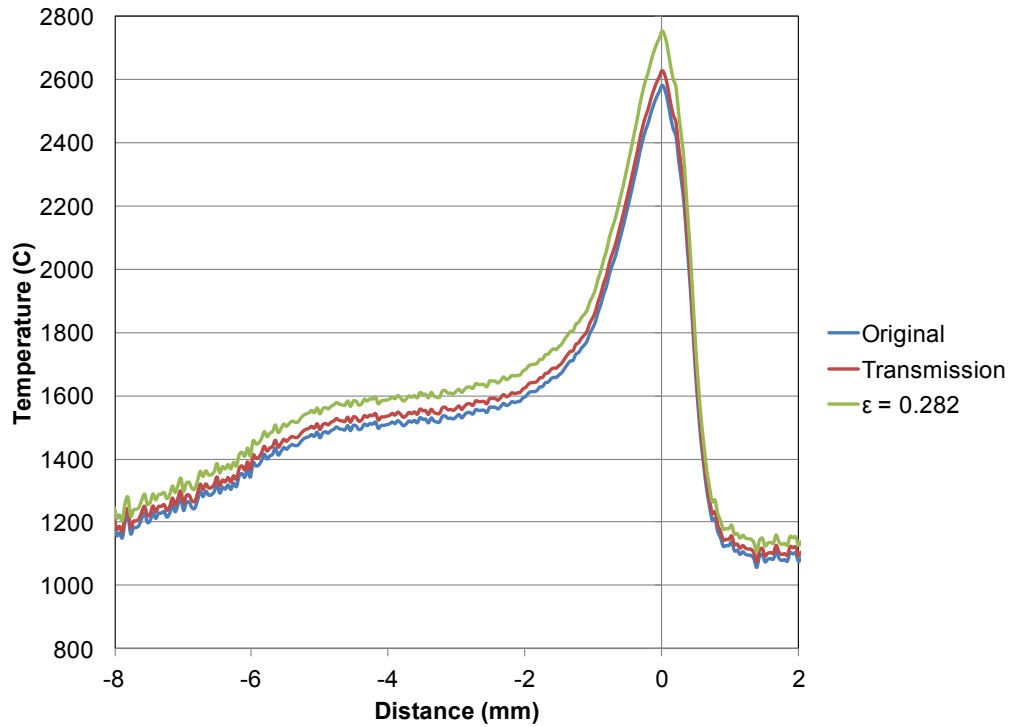


Figure 4.35. Results of transmission loss and emissivity compensation for the average temperature profile from the first build of the Controlled Exposure Experiment at a build height of 6.23 mm.

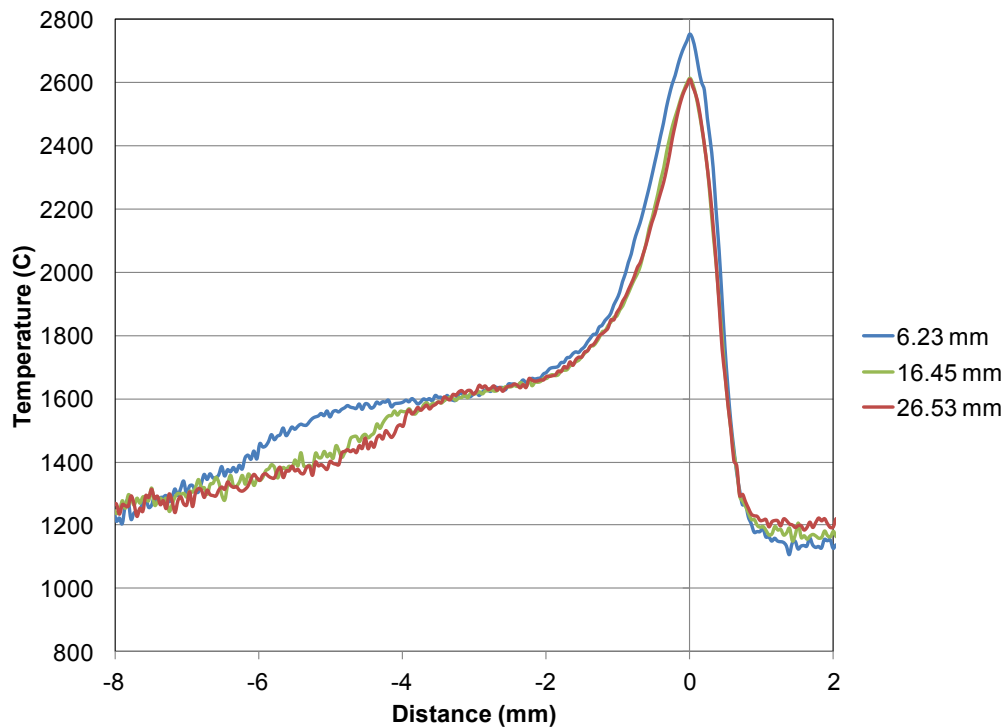
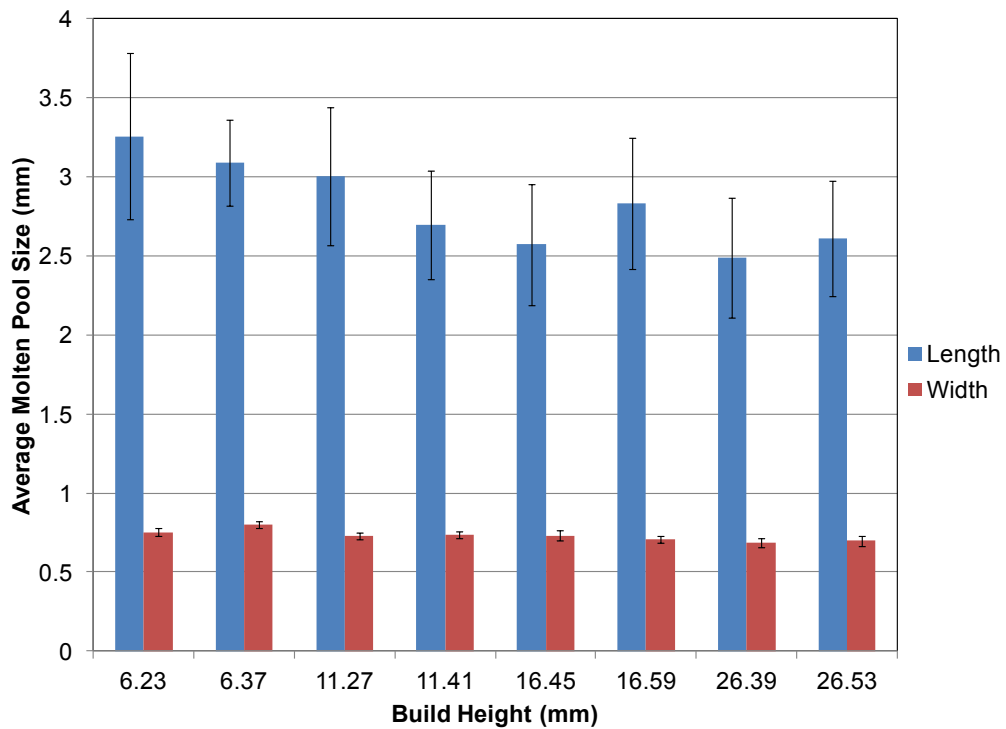
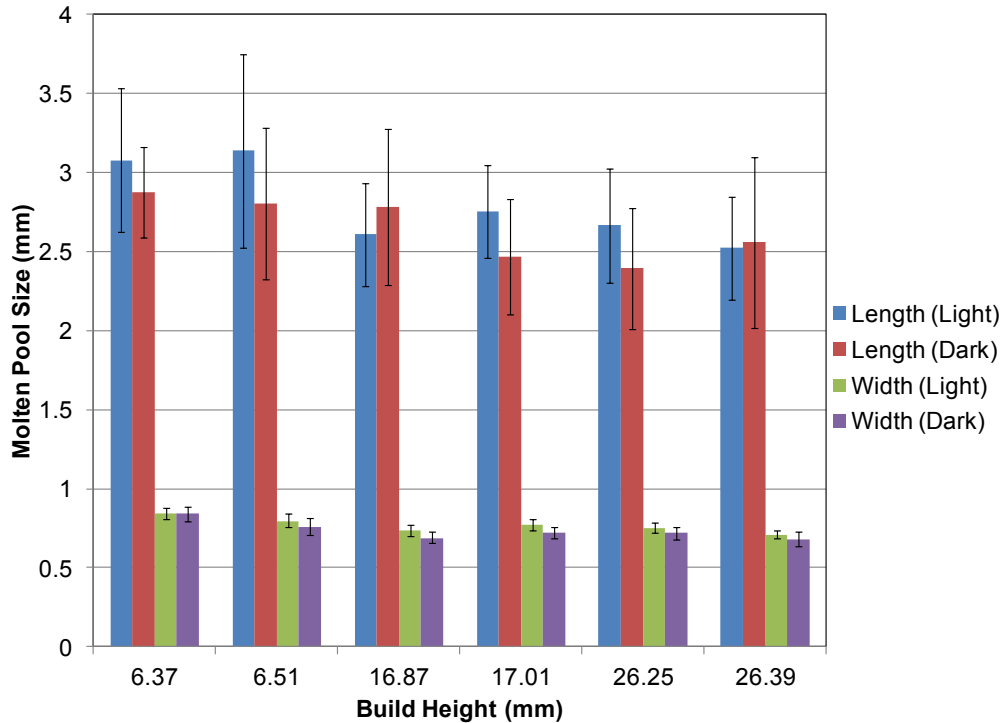


Figure 4.36. Compensated temperature profiles from the first build of the Controlled Exposure Experiment.

The average molten pool dimensions were calculated using the same procedure used in the previous experiments, and the results are shown in Figure 4.37. Both the average molten pool length and width decreased with build height, however the length decreased much more significantly. The grand means of the average molten pool lengths and widths from the first build were 2.82 mm and 0.73 mm and the standard deviations were 0.28 mm and 0.04 mm. The grand means of the average molten pool lengths and widths from the light side of the second build were 2.79 mm and 0.77 mm and the standard deviations were 0.26 mm and 0.05 mm. The grand means from the dark side were 2.65 mm and 0.73 mm with standard deviations of 0.20 mm and 0.06 mm respectively.



(a) First build

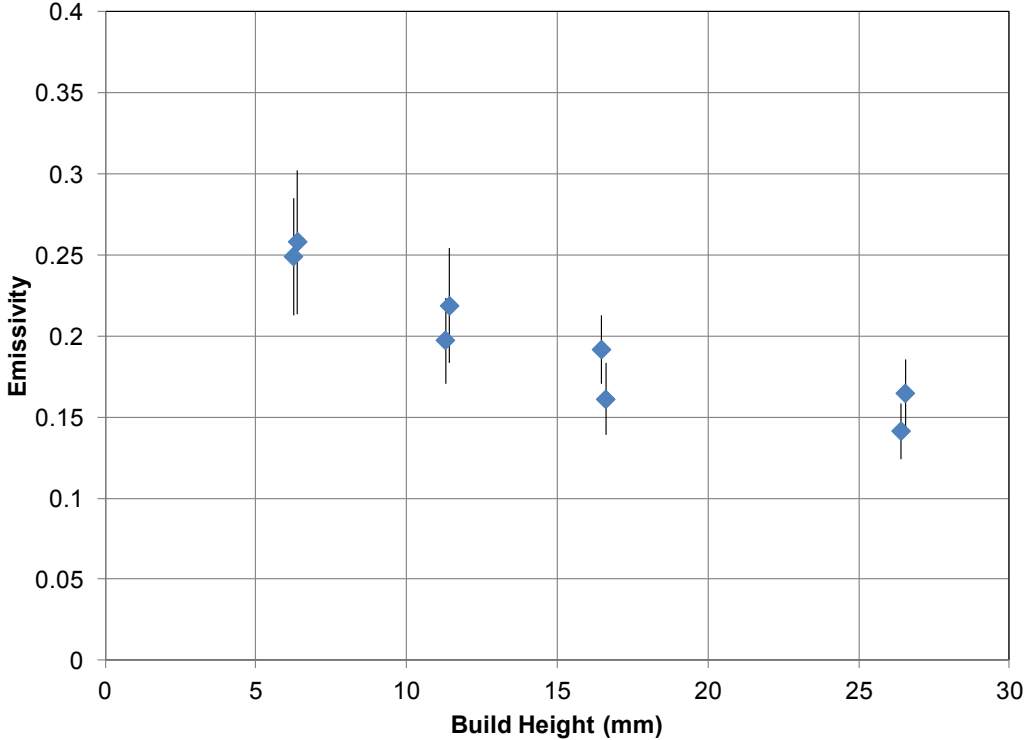


(b) Second build

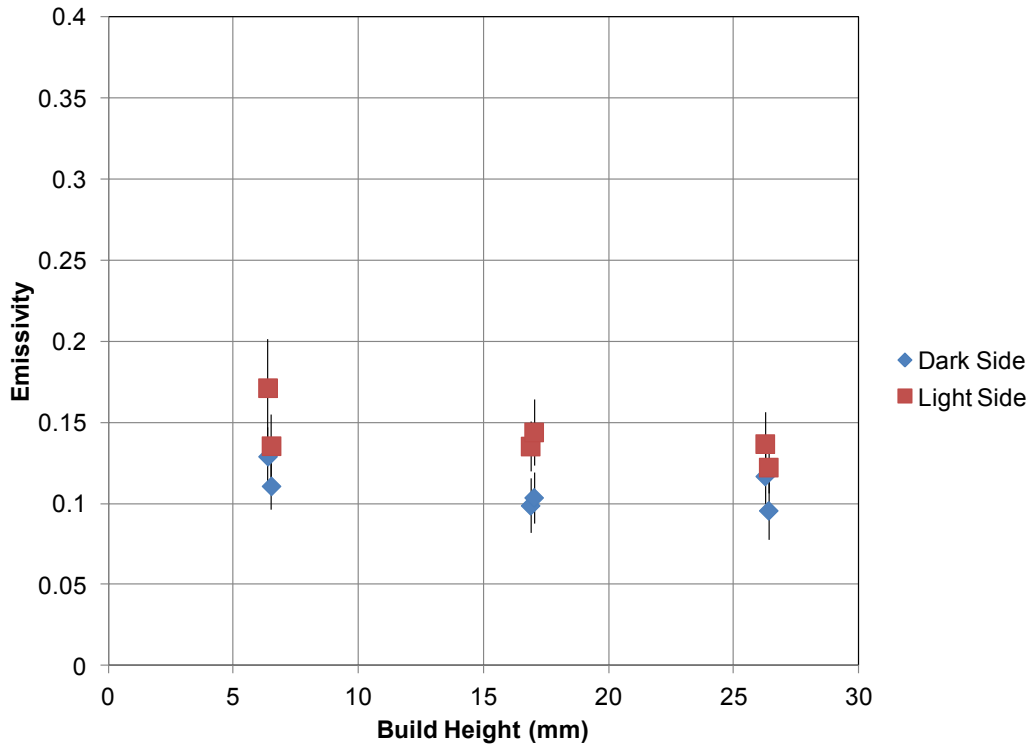
Figure 4.37. Average molten pool dimensions from the (a) first and (b) second builds of the Controlled Exposure Experiment.

The emissivity of the molten pool was also calculated using the same procedure used in the Limited Exposure Experiments. The calculated average molten pool emissivities from the builds are shown in Figure 4.38. The emissivities calculated from the first build showed a decrease with build height that slows down during the higher layers of the build. This apparent decrease in emissivity was due to the metallization of the sacrificial glass during the build. The emissivity was not truly decreasing, but the transmission loss caused the temperatures to appear cooler than they really were. Equation 7 was then used to find the emissivity that would convert that colder temperature to the true liquidus temperature. Two sets of emissivities were calculated from the second build. One set was from molten pools observed through the portion of the glass that was dark from the first build and another set was from the side that started the build clear. The calculated emissivities of the molten pool observed through the dark side of the glass were lower

than the emissivities of the molten pool observed through the light side of the glass. The difference in the results shows the impact that different levels of metallization can have on the emissivity calculation.



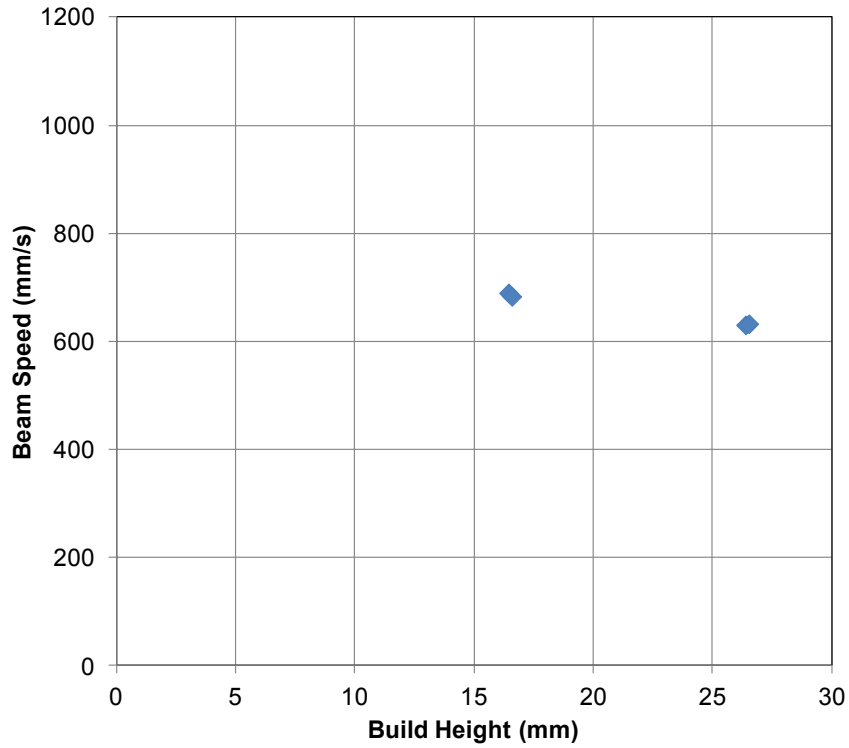
(a) First Build



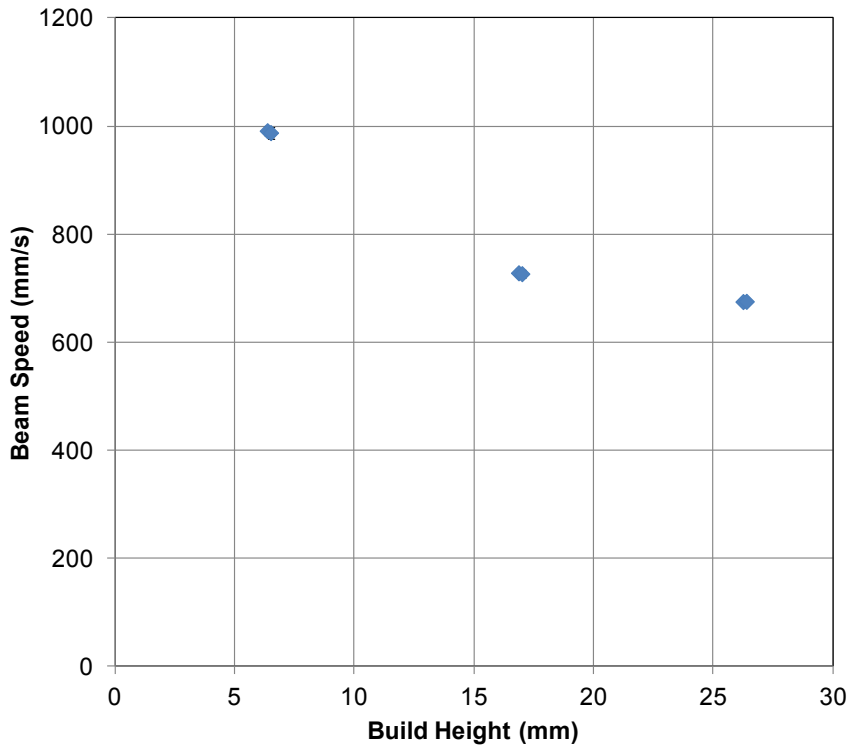
(b) Second Build

Figure 4.38. Average molten pool emissivities from the (a) first and (b) second builds of the Controlled Exposure Experiment.

The translational speed of the electron beam was also calculated by finding the distance between the hottest points of two molten pools on the same scan path from two consecutive frames. The beam speed could then be found by dividing the distance between molten pools by the reciprocal of the frame rate of the camera. The calculated beam speeds from the two experiments are shown in Figure 4.39. The results show that the Arcam speed function parameter slows the speed of the electron beam down as the height of the part increases. The rate at which the speed decreases was also found to be greater during the lower heights of the build. The steady state electron beam current was monitored from the screen of the Arcam machine and was found to drop from a value of 9.2 mA to 6.7 mA between the build heights of 6mm to 27 mm.



(a) First build



(b) Second build

Figure 4.39. Average beam speeds from the (a) first and (b) second builds of the Controlled Exposure Experiment.

Summary

Experiments were conducted that had high, limited, and controlled exposure of the sacrificial glass. The High Exposure Experiment revealed that the heat shield bars were causing interference with the temperature measurements. The results from Limited Exposure Experiment I proved the repeatability of the temperature measurements. Limited Exposure Experiment II led to the discovery that the length of the phase transition area of the molten pool temperature profile decreases with build height. It was found that minimizing the exposure time of the sacrificial glass is critical in ensuring that the metallization of the sacrificial glass does not become severe. Based on the rapid decrease in calculated emissivity during the beginning of Limited Exposure Experiment II, the rate of metallization appeared to be higher during the first several millimeters of the build, therefore keeping the shutter closed until at least 5 mm of build height have been completed was found to be helpful in limiting the severity of the metallization. In the Controlled Exposure Experiment, the effects of transmission loss from metallization on the measured temperatures were studied and a method to compensate for the losses was developed.

CHAPTER V

PROCESS CONDITION EFFECTS

This chapter presents the results of experiments conducted to study the effects that beam speed and current as well as overhang geometry have on the temperatures and dimensions of the molten pool. These experiments also provided a better understanding of the Arcam S12 EBAM machine speed function and current algorithms as well.

Speed Function Experiment

The process parameters used by the Arcam EBAM machine can be modified from their default values in two different ways. One option is to input fixed values for parameters such as beam current and speed. The second option is to change the value of the speed function index. While using constant values of beam current and speed would have allowed more control over the magnitude of the process parameters, it was suggested that modifying the speed function index value had a higher chance of resulting in a successful build.

Four parts with 60 mm x 5.25 mm cross-sections that were 25 mm tall were fabricated in the in both builds conducted for this experiment. Each part was assigned a different speed function. The speed functions selected were 20, 36 (default value), 50, and 65. Sample NIR images of the molten pool during hatch melting at each speed function are shown in Figure 5.1.

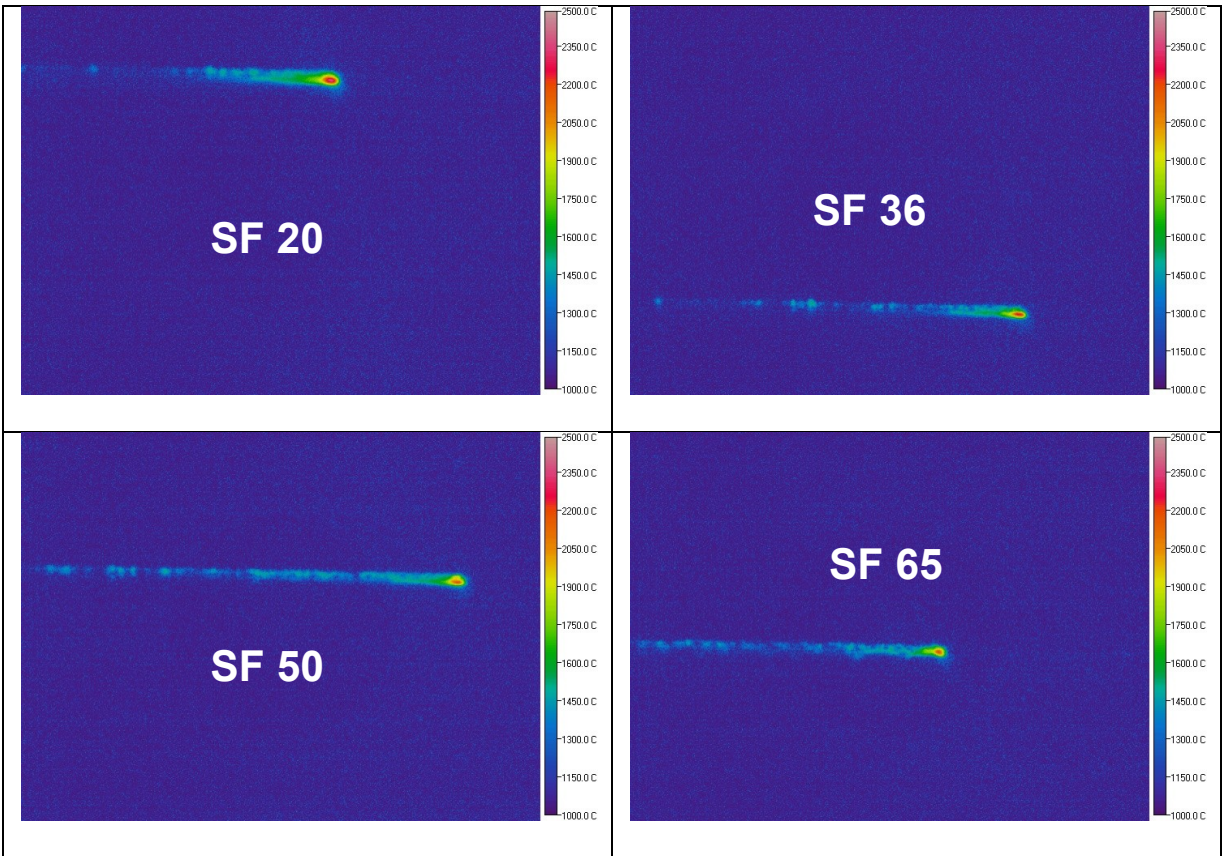


Figure 5.1. Molten pool during hatch melting at different speed functions.

The spatial resolutions were calculated using the same procedure discussed in the previous chapter. The plots from the feature detection Matlab code are shown in Figure 5.2. The horizontal resolutions were 48.5 and 49.2 $\mu\text{m}/\text{pixel}$ and the vertical resolutions were 65.2 and 65.8 $\mu\text{m}/\text{pixel}$ respectively for the first and second builds.

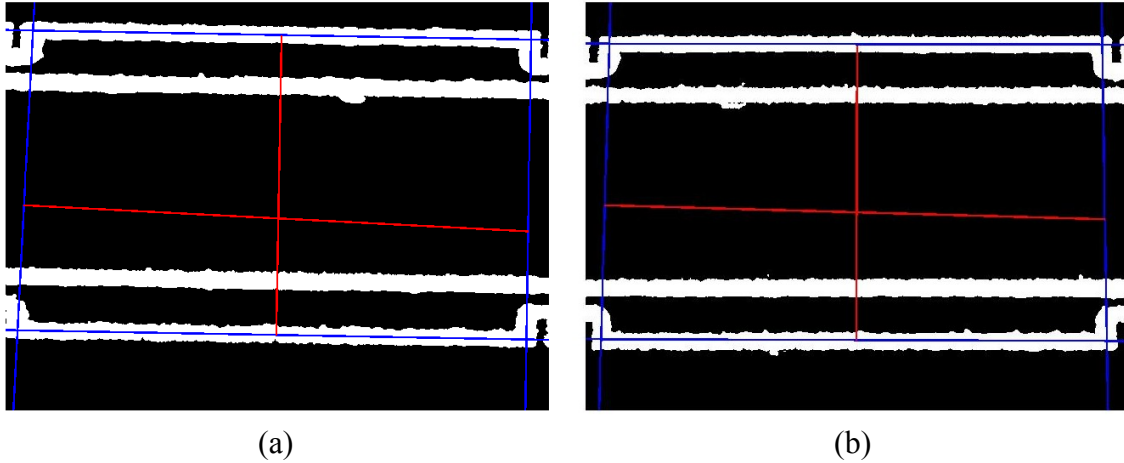


Figure 5.2. Spatial resolution determination for the (a) first and (b) second builds of the Speed Function Experiment.

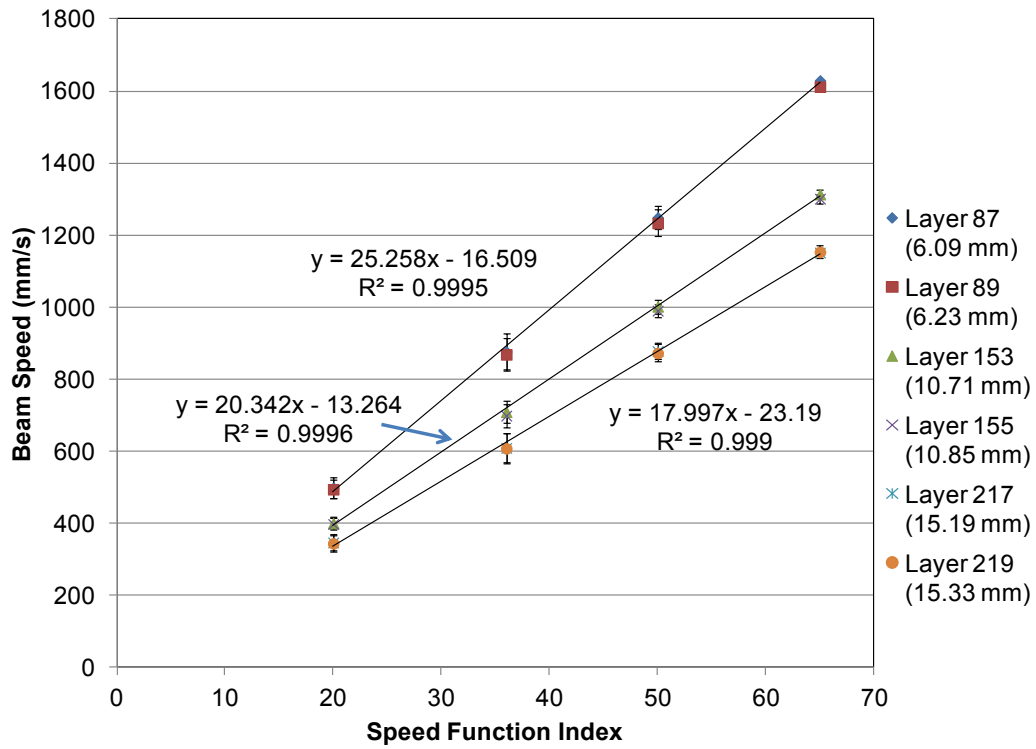
The beam speeds were calculated using the method developed in the Controlled Exposure Experiment. The calculated beam speeds are shown in Figure 5.3. The data revealed that at each specific build height, the beam speeds generated by different speed function indices were linearly related. As the build height increased, it was also found that the slope of this linear relationship decreased linearly, shown in Figure 5.4. Equations were developed from the experimental data that could calculate the beam speed as a function of build height and speed function index. Each equation was found by multiplying the equation of the linear fit of the slopes of the speed function relationships at different build heights by the speed function index. The beam speed estimation equations found from the Speed Function Experiment data are shown as Equations 8 and 9.

$$V = (-0.814h + 29.52)SF \quad (8)$$

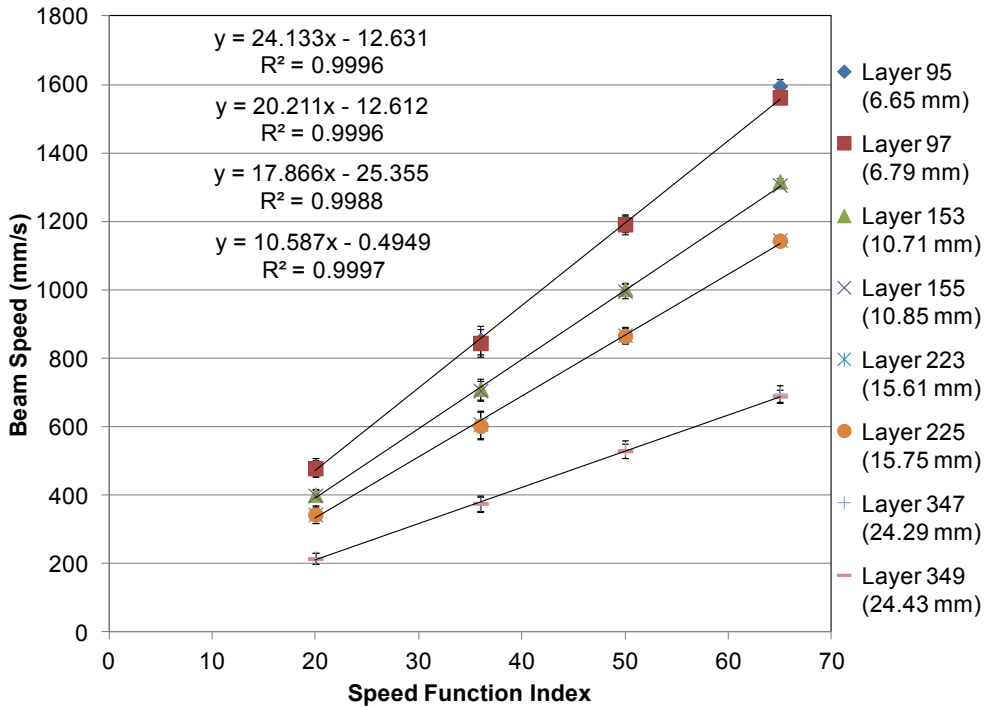
$$V = (-0.7343h + 28.554)SF \quad (9)$$

V is the translational beam speed in mm/s, h is the build height in mm, and SF is the speed function index. The beam speeds calculated using these equations were compared to the experimental data and were found to match closely, with a maximum error of 6.6%. The speed

function algorithm is believed to be sensitive to other variables as well so these equations are only valid for parts with constant cross-sections and similar size. Plots comparing the beam speeds calculated from Equations 8 and 9 with the experimental data are shown in Figure 5.5.

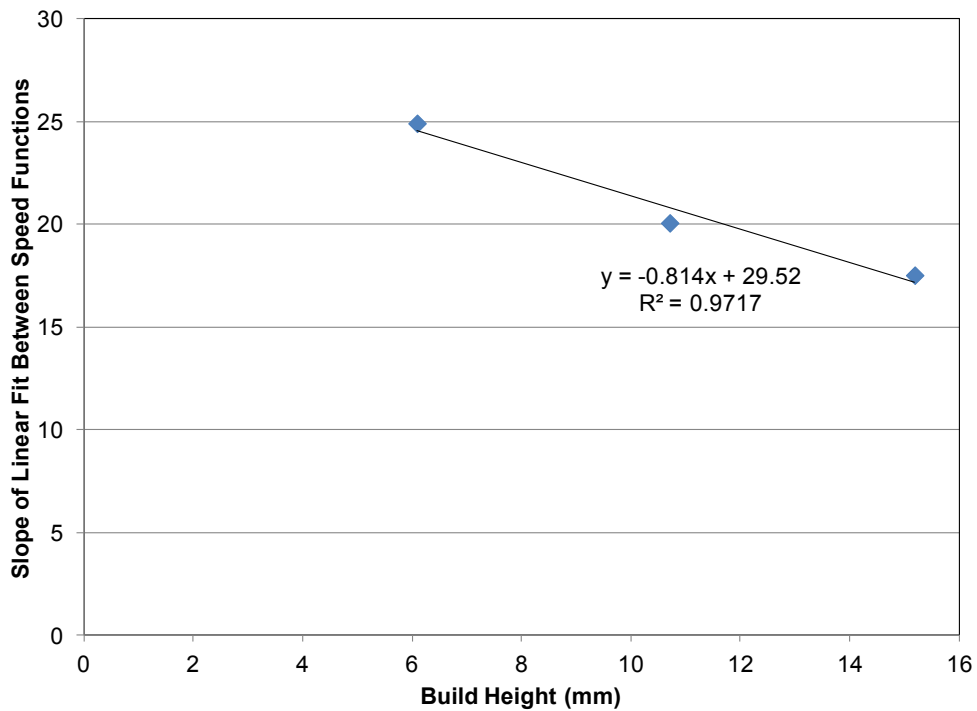


(a) First build

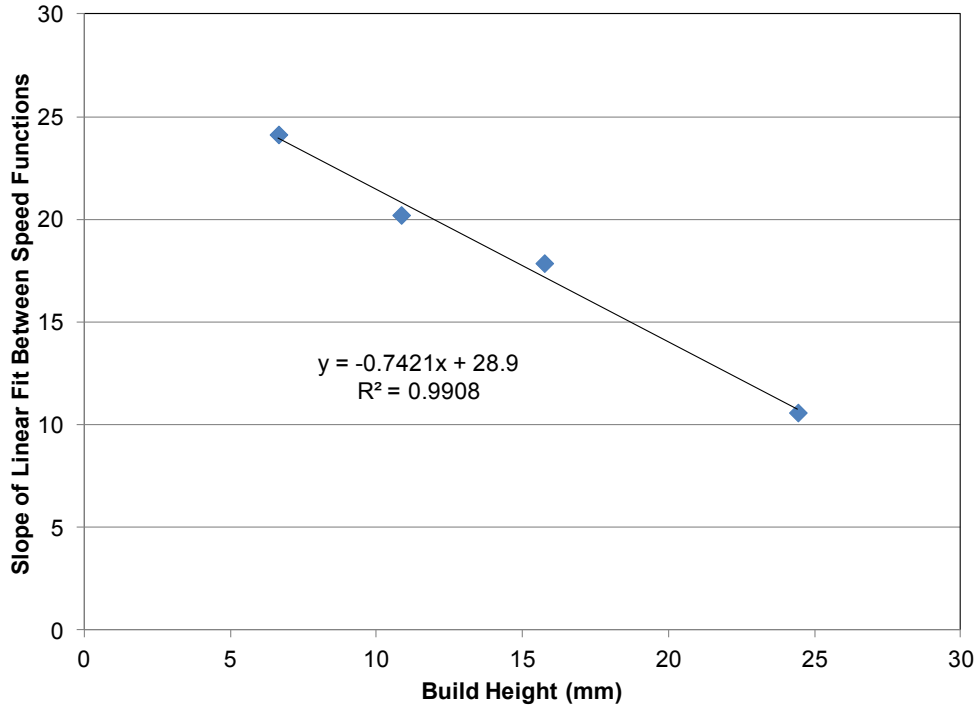


(b) Second build

Figure 5.3. Average beam speeds from the (a) first and (b) second builds of the Speed Function Experiment.

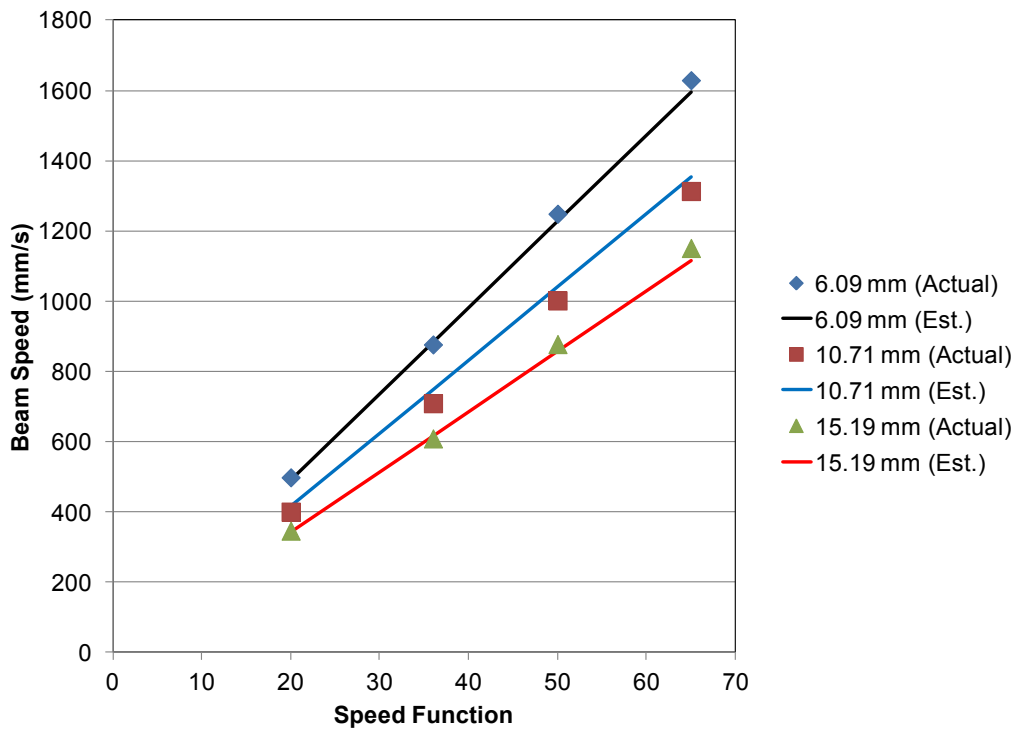


(a) First build

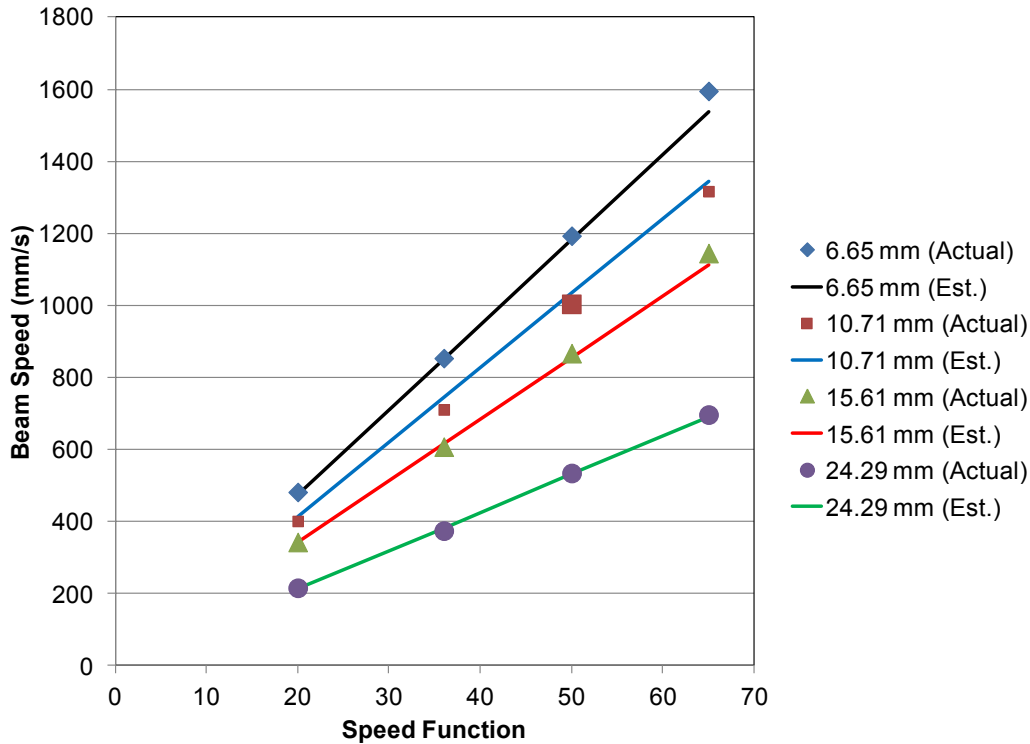


(b) Second build

Figure 5.4. Slopes of linear fits between speed functions from the (a) first and (b) second builds of the Speed Function Experiment.



(a) First build



(b) Second build

Figure 5.5. Comparison of estimated beam speeds with actual beam speeds from the (a) first and (b) second builds of the Speed Function Experiment.

The beam speeds determined for the fabrication of the part built with a speed function index of 36 were lower than what was calculated at similar build heights from the Controlled Exposure Experiment. It is possible that the speed function algorithm may have decreased the beam speed overall in response to the small size of the test parts. Another effect noticed was that the beam speed decreased when scanning between the notches (Figure 3.7b) in the part that were used for spatial resolution determination. Figure 5.6 shows a plot of every beam speed calculated from one layer of the part fabricated with a speed function index of 20. The dashed red line indicates the raster where the transition from normal rasters to scanning between the notches occurred. As the graph shows, the speed is slower when scanning between the notches.

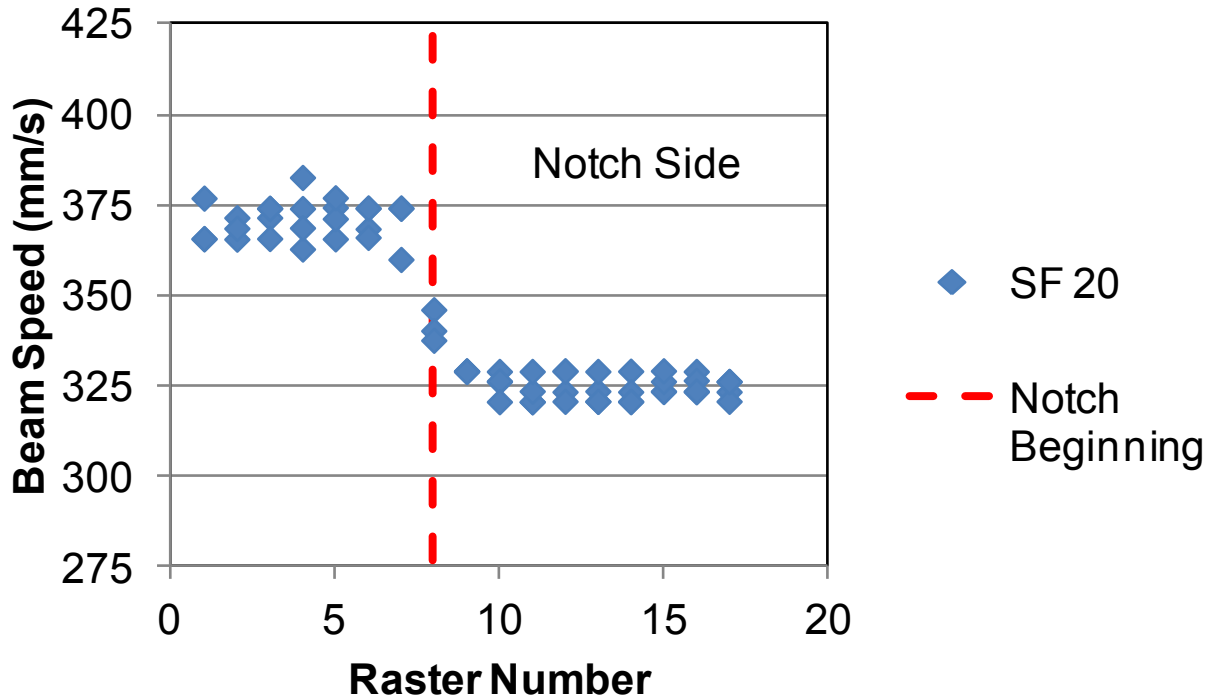


Figure 5.6. Beam speeds from speed function 20 part from second build of the Speed Function Experiment showing notch effect.

The beam current during steady state hatch melting was recorded from a readout on screen of the Arcam machine during the builds and plotted in Figure 5.7 in order to show how the beam current changes with build height. The beam current was found to be 15.9 mA until a build height of 1.5 mm was reached. The beam current then quickly dropped, slowing at 10 mA at 2 mm of build height. The beam current then began to decrease much slower during the rest of the build.

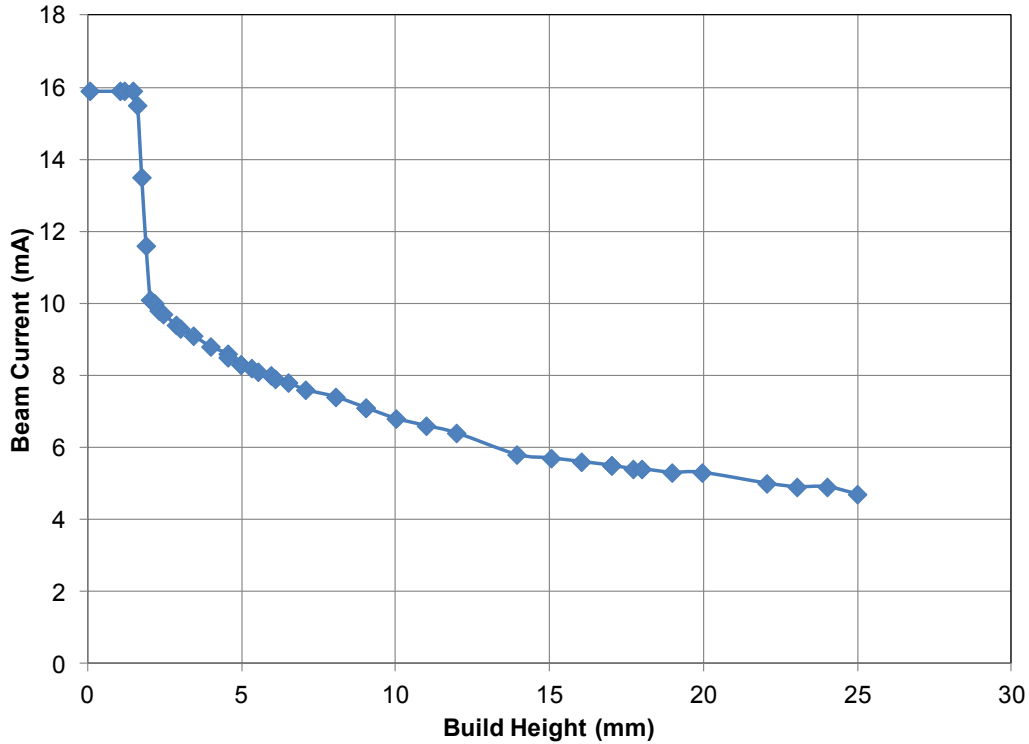
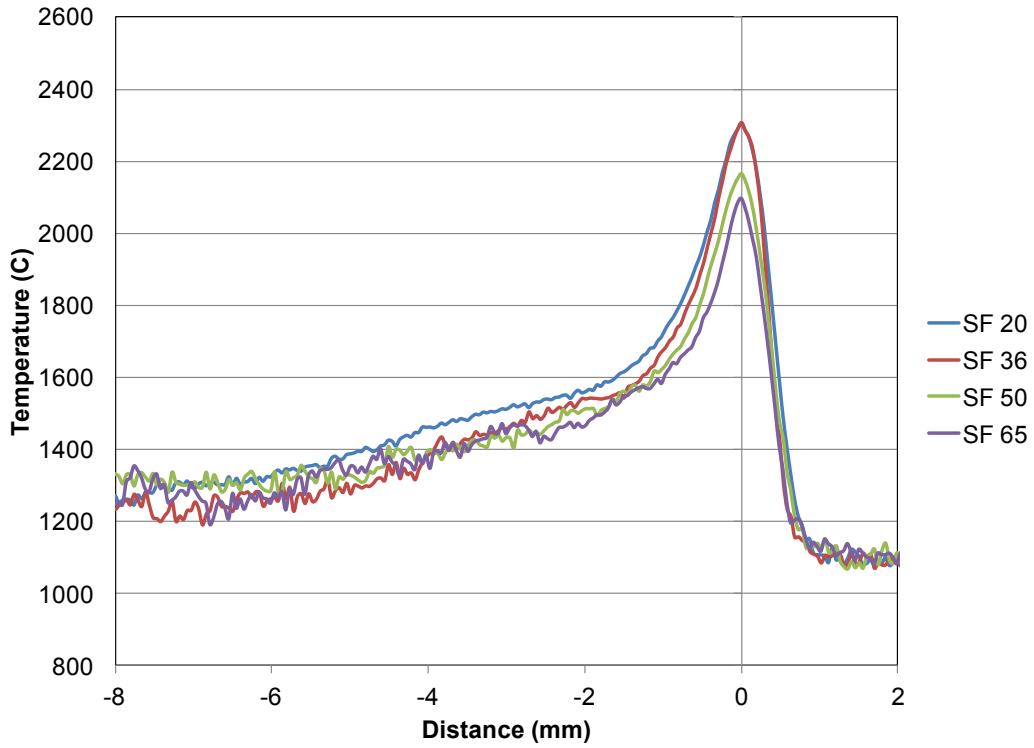
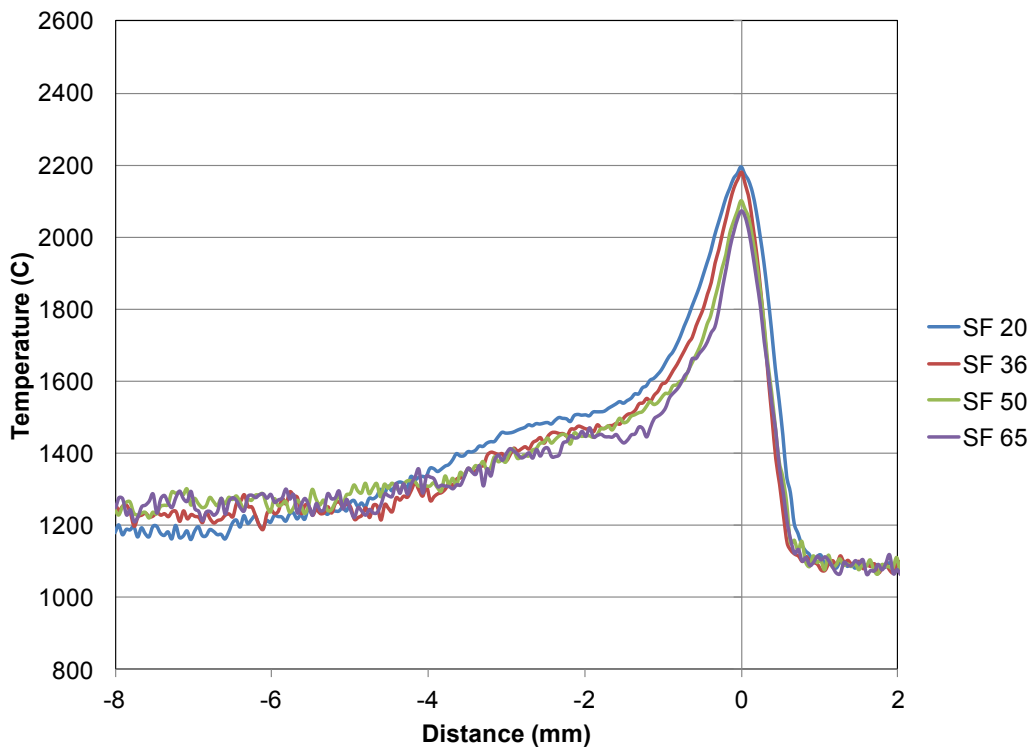


Figure 5.7. Beam current versus build height from the Speed Function Experiment.

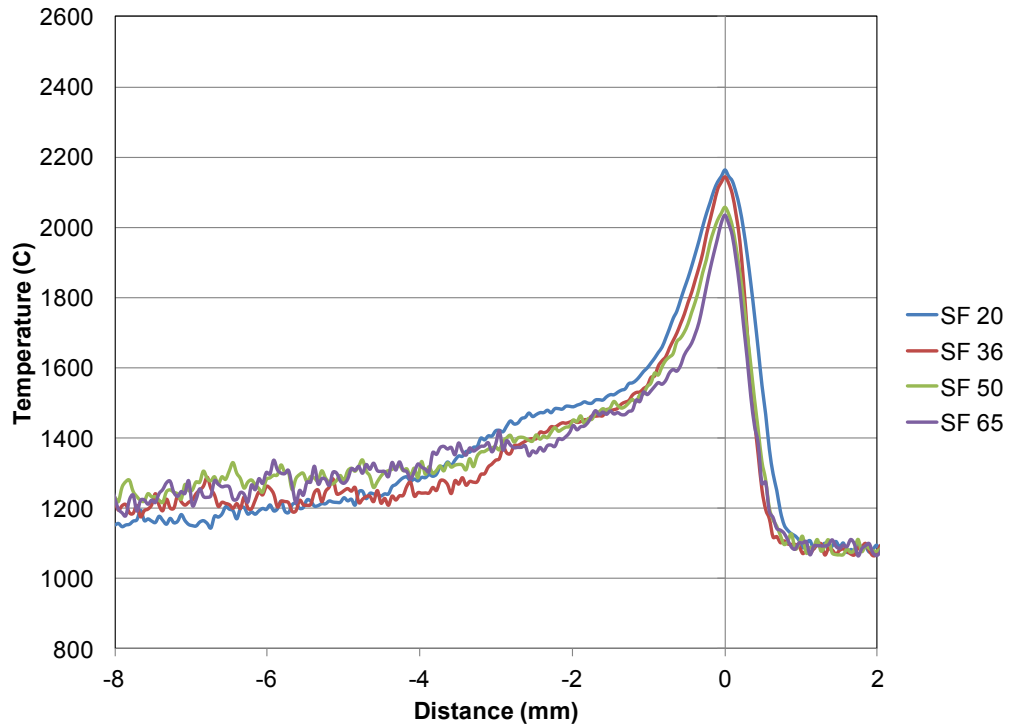
Average temperature profiles were determined for each speed function at various heights. Comparisons of these profiles at individual heights from the first build are show in Figure 5.8. The average temperature profiles from the second build are shown in Figure 5.9. In the first build, the maximum temperatures from the speed function 20 and 36 cases were very close and in the second build the maximum temperatures from the speed function 36 and 50 cases were very close. The results also show that the phase transition region of the cooling curve from the speed function 20 case was longer than those from the higher speed function cases.



(a) 6.09 mm

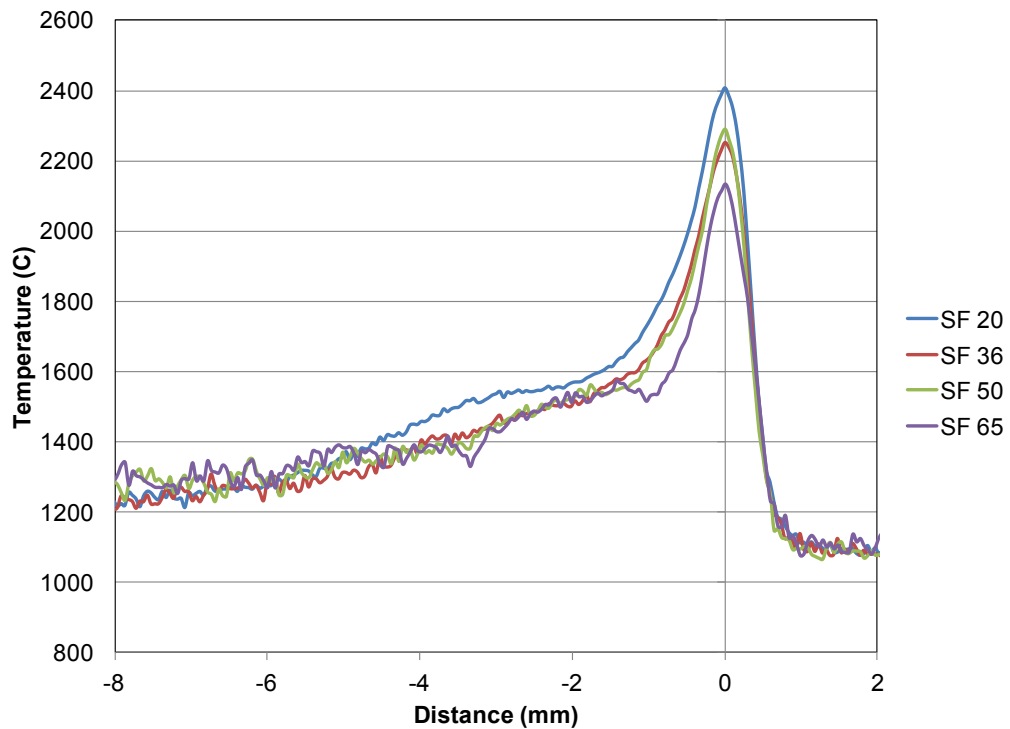


(b) 10.71 mm

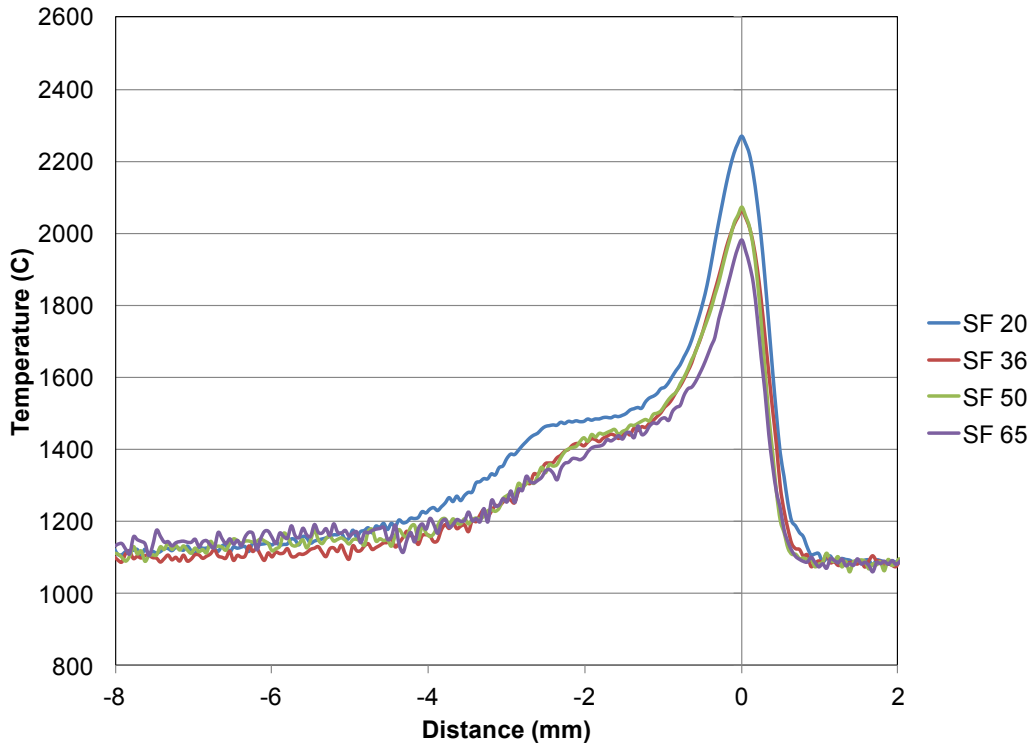


(c) 15.19 mm

Figure 5.8. Average temperature profiles from the first build of the Speed Function Experiment at build heights of (a) 6.09 mm, (b) 10.71 mm, and (c) 15.19 mm.



(a) 6.65 mm



(b) 24.43 mm

Figure 5.9. Average temperature profiles from the second build of the Speed Function Experiment at build heights of (a) 6.65 mm and (b) 24.43 mm.

The compensation technique developed in the Controlled Exposure Experiment was applied to several of the temperature profiles from the Speed Function Experiment in order to correct them for transmission loss due to metallization and estimated emissivity. The transmission loss effect curve is shown in Figure 5.10. In Figure 5.11, the original average temperature profiles for the SF 20 case at different build heights are shown as well as their compensated profiles. After compensation, it can be seen that the differences in maximum temperatures were not as significant as they appeared before compensation. Figure 5.12 compares the compensated temperature profiles from one build height and different speed function indices. The original profiles can be referenced from Figure 5.9(a).

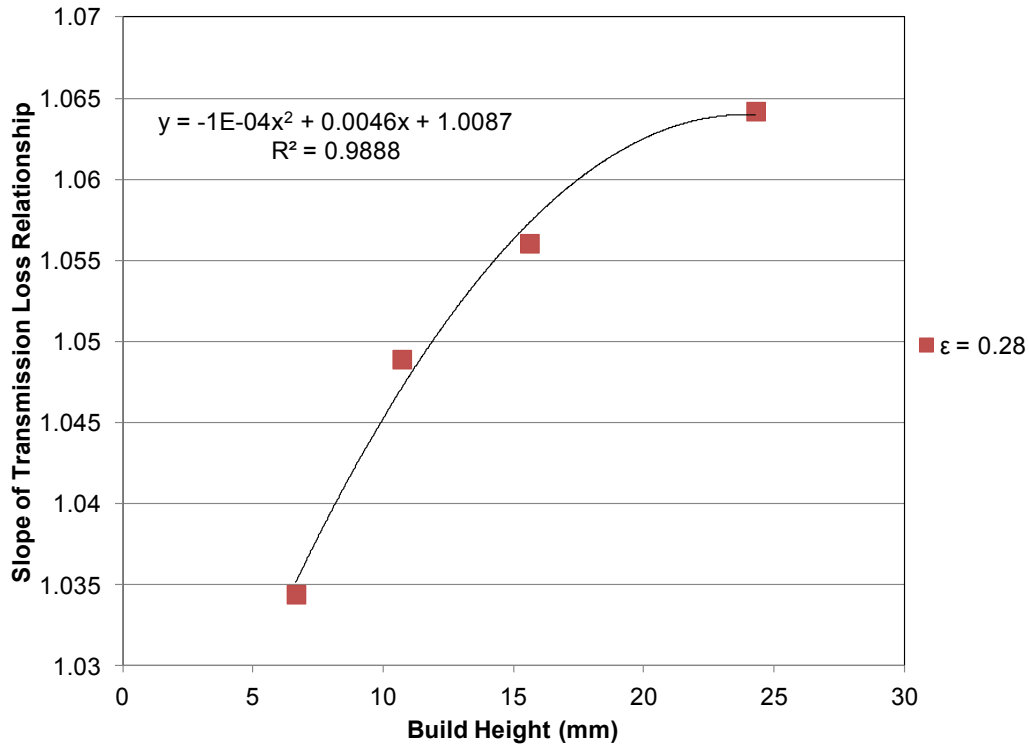
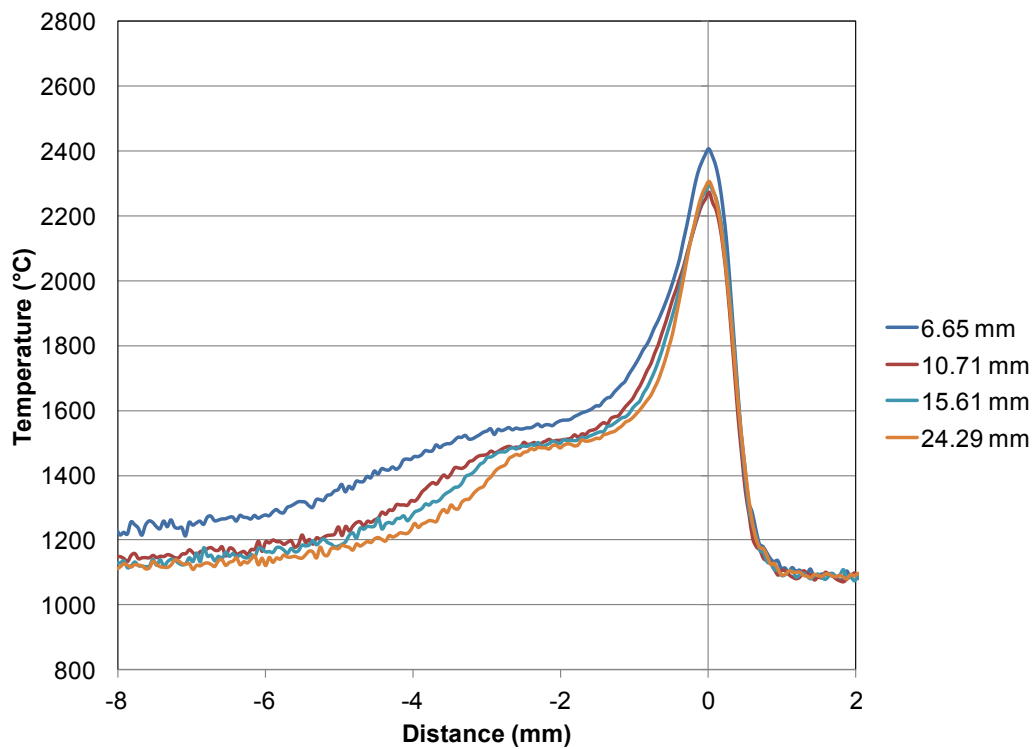
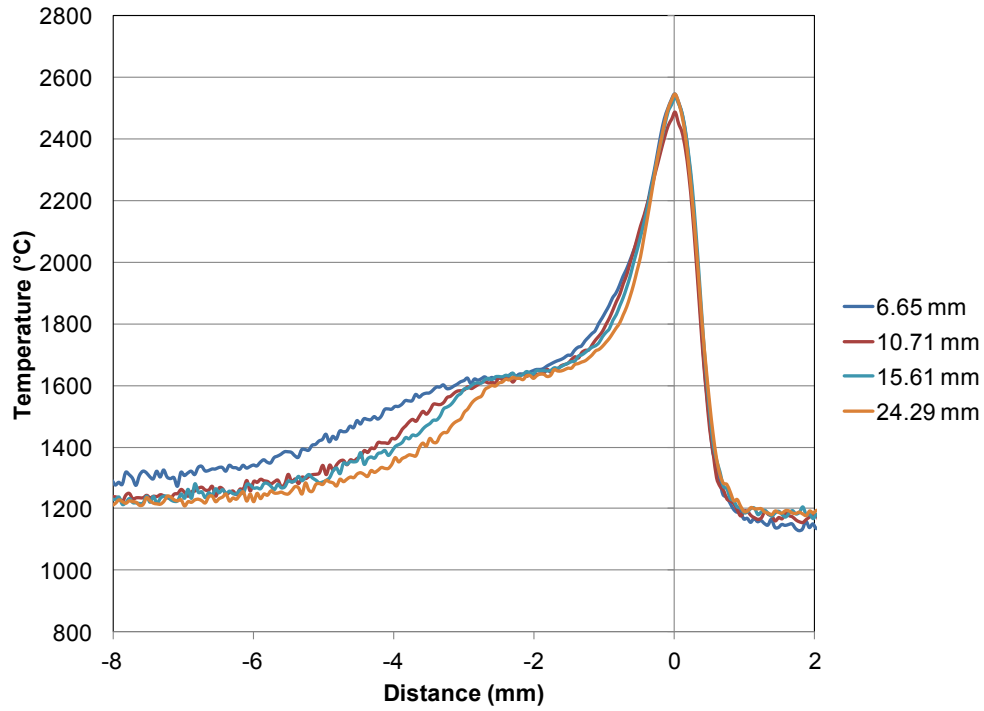


Figure 5.10. Slope of transmission loss relationship at different build heights from the second build of the Speed Function Experiment.



(a) Original



(b) Compensated

Figure 5.11. (a) Original and (b) compensated average temperature profiles from the second build of the speed function experiment.

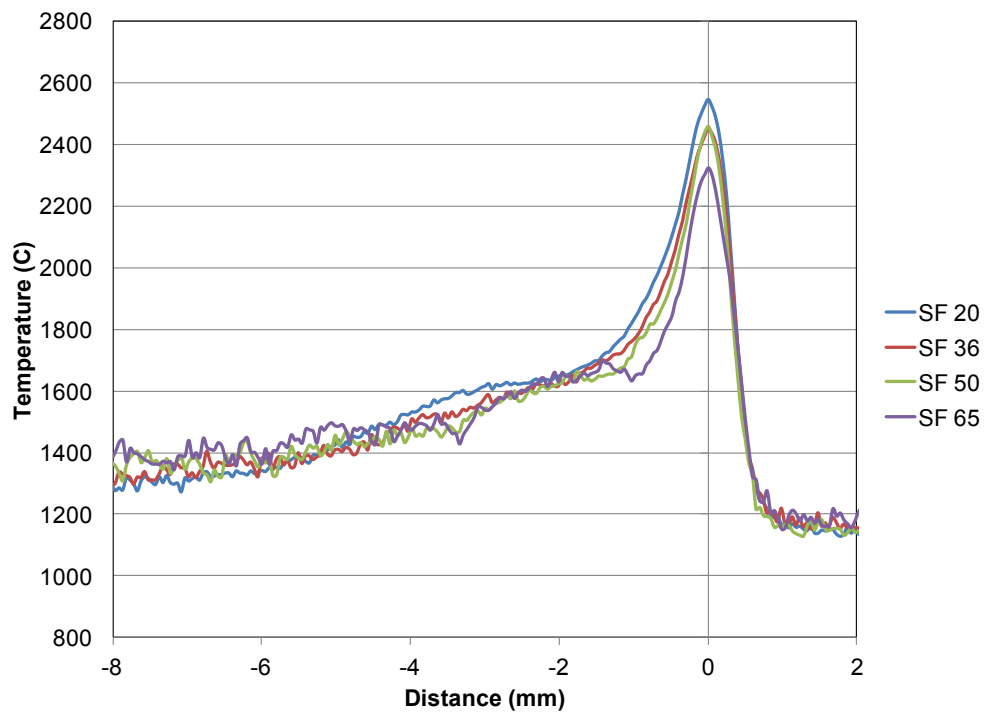
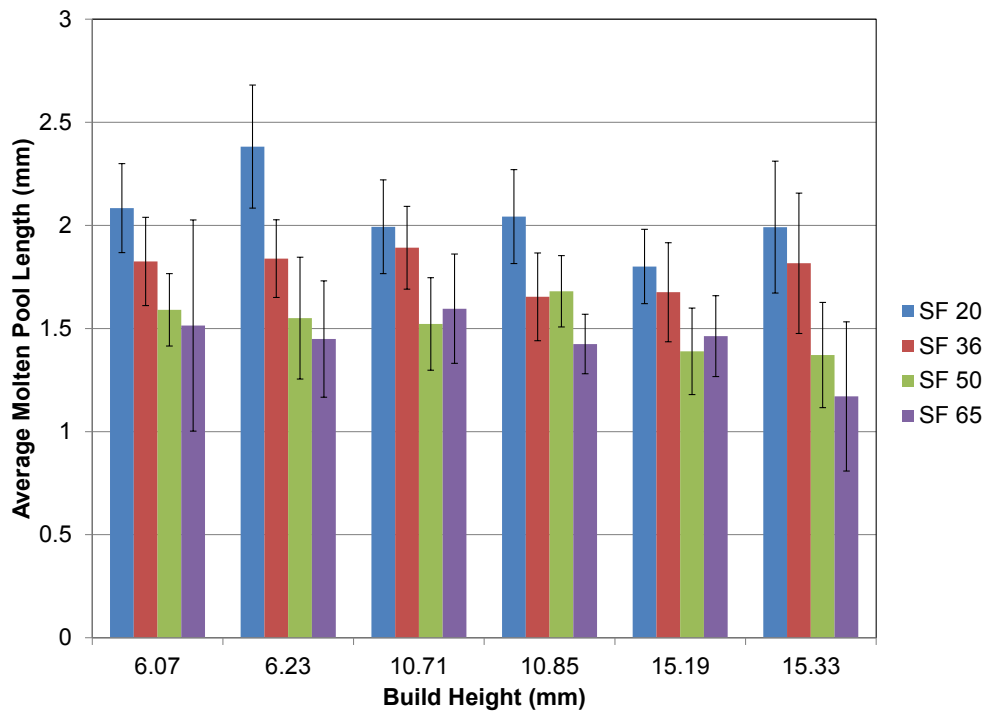
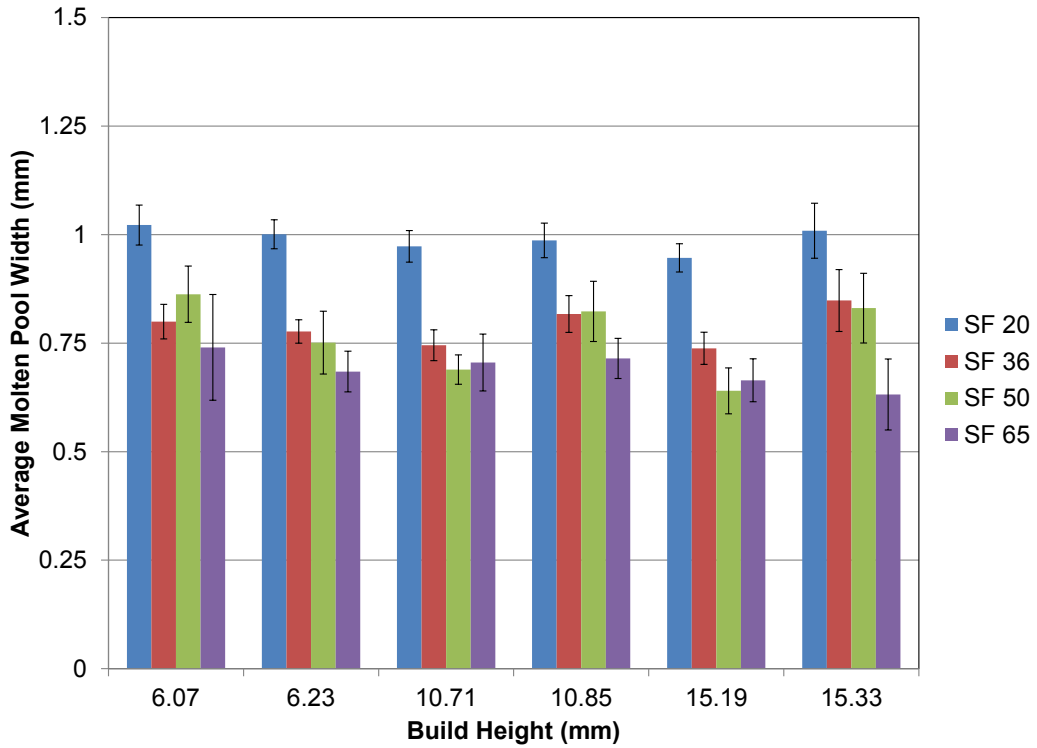


Figure 5.12. Compensated profiles from the second build of the Speed Function Experiment at 6.65 mm.

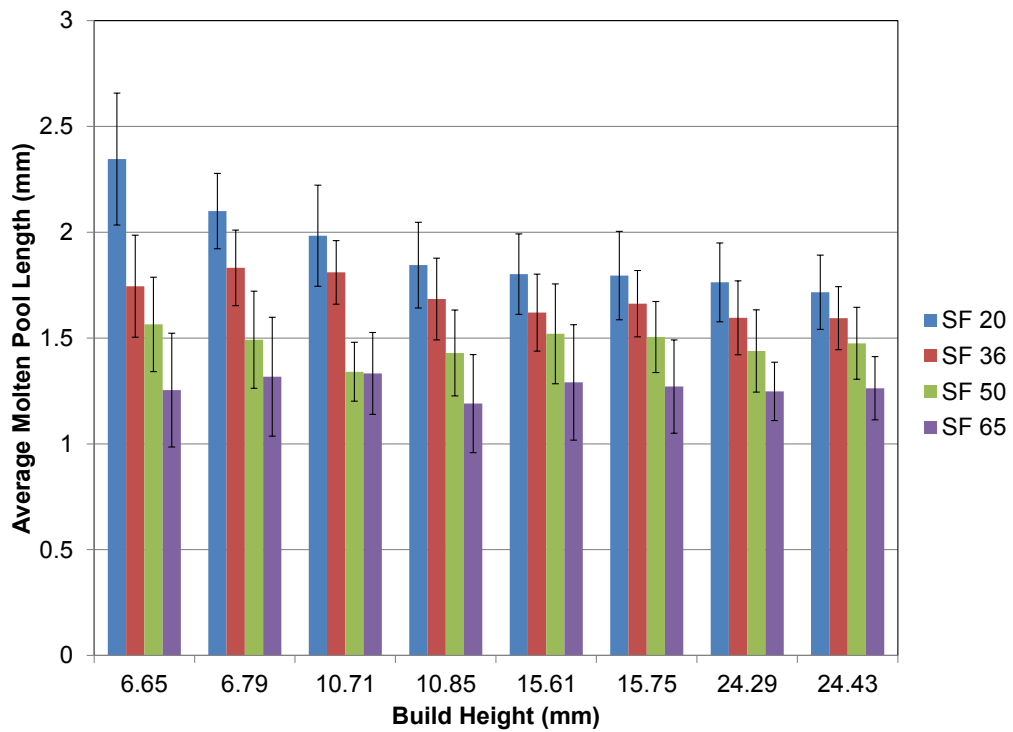
The average molten pool dimensions were calculated for each speed function at various build heights and are shown in Figure 5.13. An overall trend was seen that both the molten pool length and width decrease as the speed function index is increased. Many of the average molten pool lengths of the SF 36 case are over 1 mm shorter than the average molten pool lengths calculated in the previous experiments. This is possibly due to the lower beam current used by the EBAM machine in this experiment due to the small size of the parts. The beam current in the Controlled Exposure Experiment was around 1-2 mA larger at similar build heights. The average molten pool widths were very similar to those measured in the previous experiments. Figure 5.14 shows the average molten pool lengths and widths as a function of beam speed from the second build at build heights of 6.65 mm and 24.43 mm. Figure 5.15 shows the repeatability of the molten pool dimensions between the two builds. The points are the averages of the lengths and widths from the two builds at similar heights. The error bars show the range of the values from the two builds.



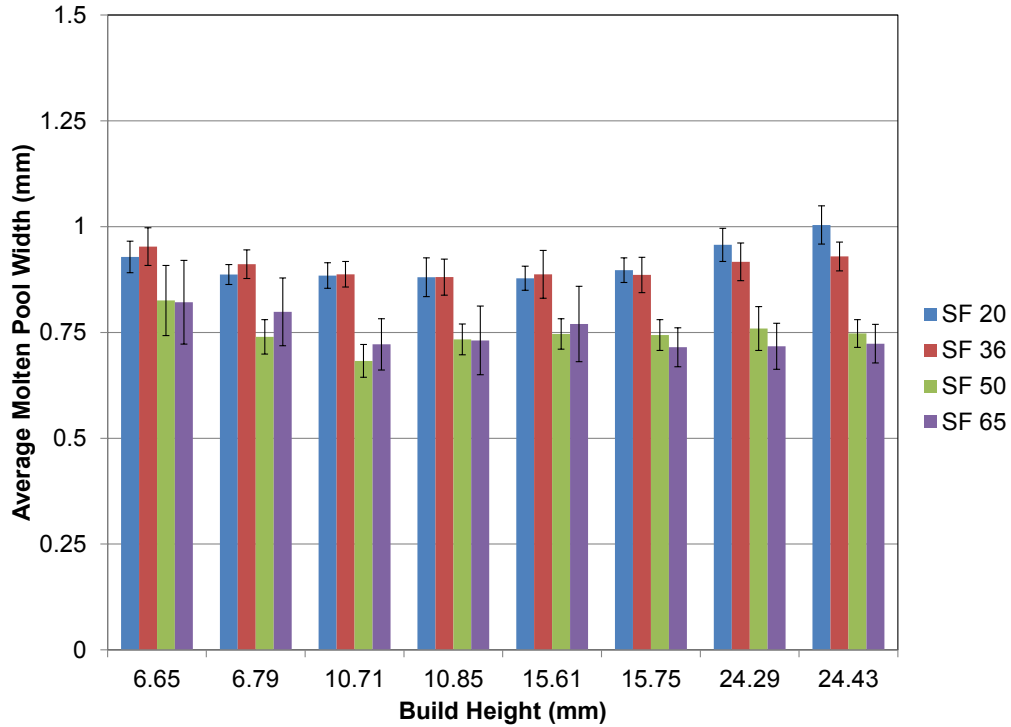
(a) First build lengths



(b) First build widths

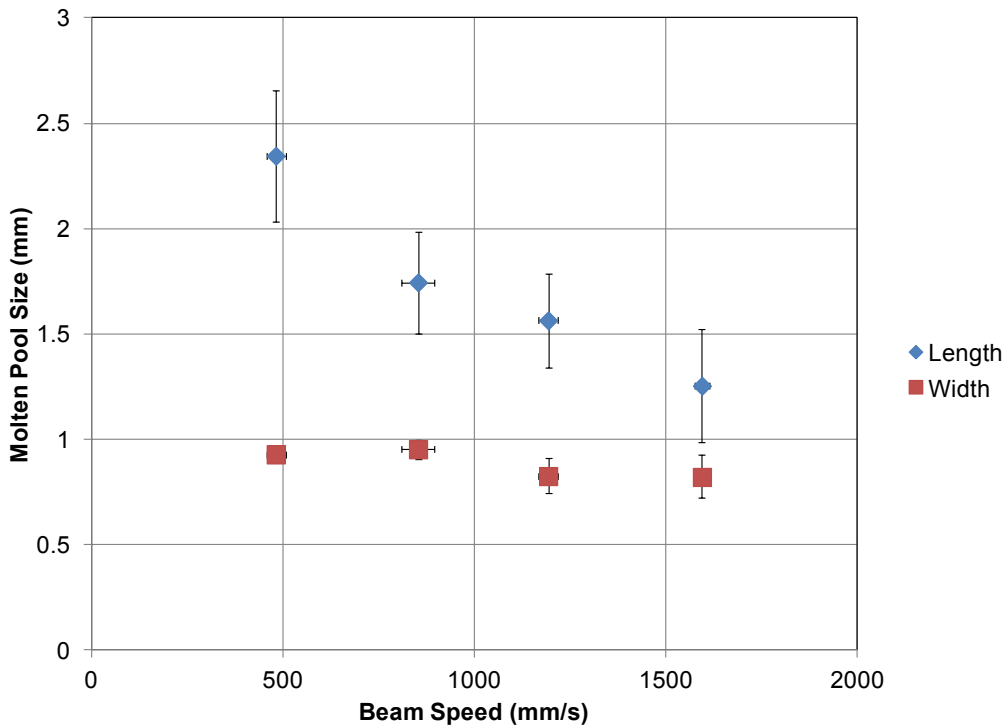


(c) Second build lengths

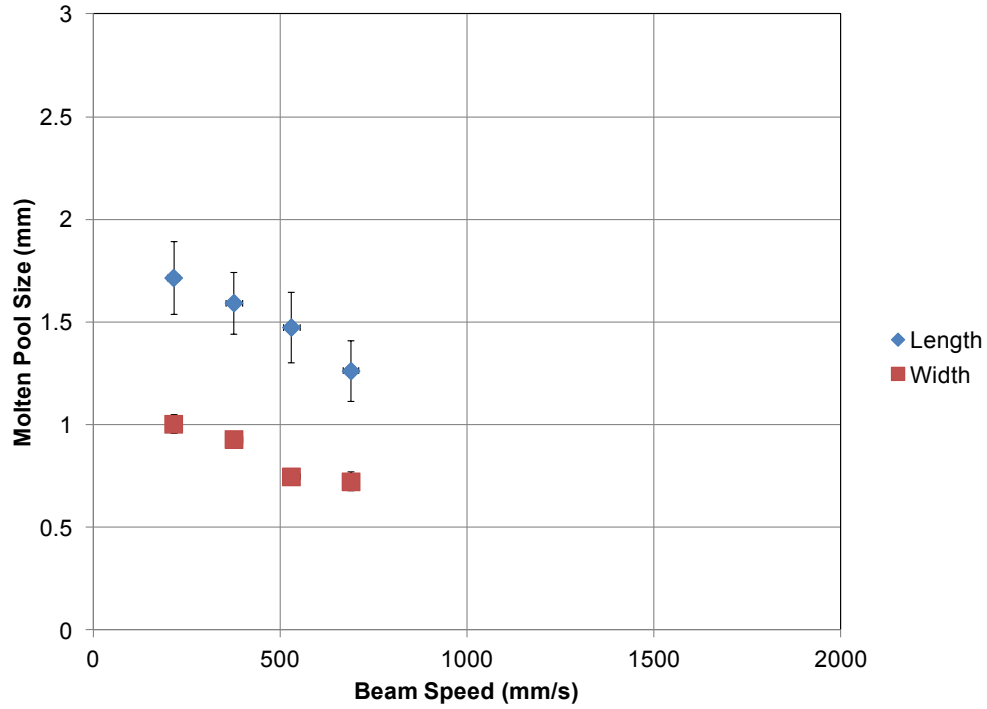


(d) Second build widths

Figure 5.13. Average molten pool lengths from the (a) first and (b) second builds and average molten pool widths from the (c) first and (d) second builds of the Speed Function Experiment.



(a) 6.65 mm



(b) 24.43 mm

Figure 5.14. Average molten pool lengths and widths as function of beam speed from the second build of the Speed Function Experiment at build heights of (a) 6.65 mm and (b) 24.43 mm.

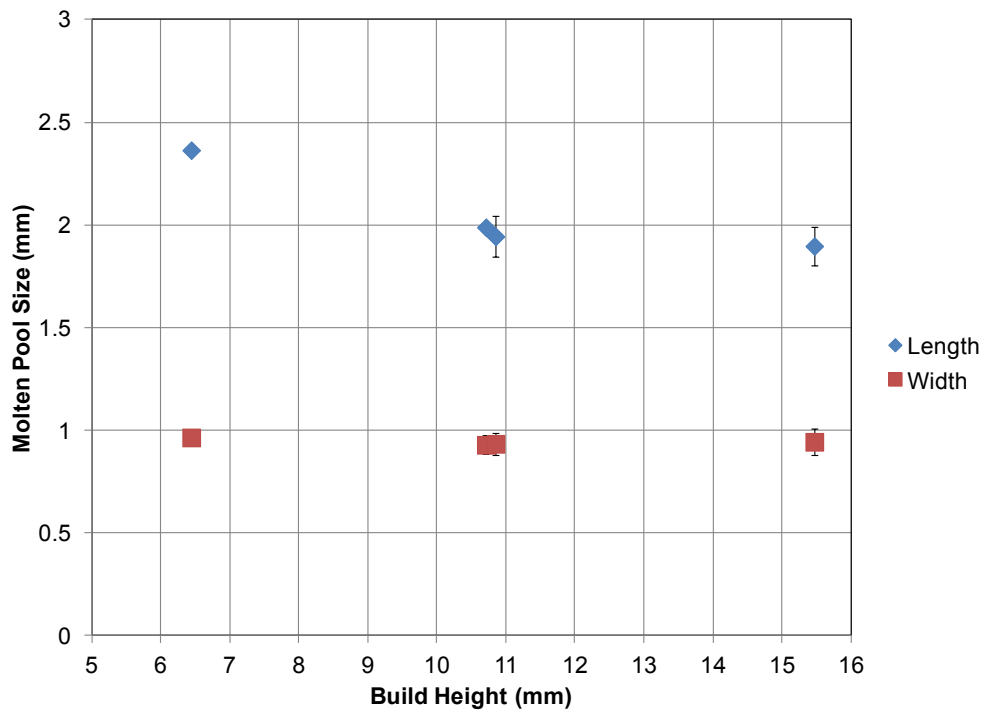


Figure 5.15. Averages and ranges of the molten pool dimensions at similar build heights from both builds of the Speed Function Experiment.

Overhang Part Experiment

A powder substrate is sometimes encountered during the build process because sintered powder serves as support material under overhang features of the part. The thermal conductivity of the sintered powder substrate is lower than that of solid Ti-6Al-4V which leads to different thermal histories for overhang structures than for structures with a solid substrate. The thermal effects of melting over a powder substrate were investigated in order to better understand this common fabrication scenario. The CAD model of the test part and the final fabricated part that were used in the experiment are shown in Figure 5.16. The two thin shelves in the upper two-thirds of the part are the overhang structures. The cavities between these shelves were filled with sintered powder during the EBAM process.

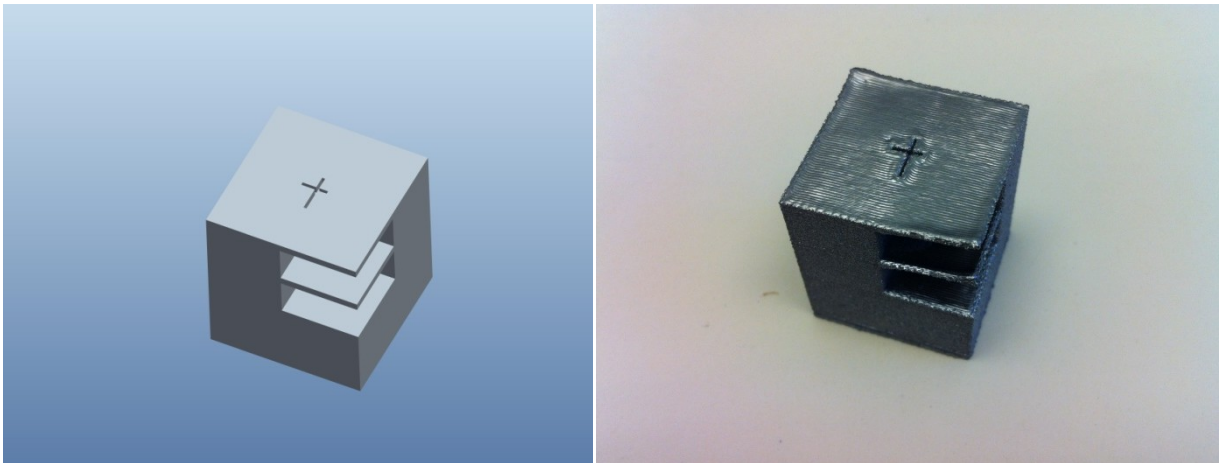


Figure 5.16. Overhang CAD model and part fabricated during Overhang Part Experiment.

Figure 5.17 shows the layout of the substrates in the NIR images of the fabrication of the middle “shelf” of the part shown in Figure 5.16. The top-right quarter of each image in Figure 5.18 had a solid substrate and the bottom-right quarter of each image had a powder substrate. The images from the first overhang layer show that cooling occurs much slower over the powder substrate when compared with the solid substrate. However, this effect is almost completely diminished by the third layer above the powder substrate. In order to study the slower cooling

over the powder substrate 2D temperature profiles were generated from frames from the first overhang layer footage. The profiles were aligned at the interface of the solid and powder substrates and oriented so that the common scanning direction was rightward, then averaged together. 2D temperature profiles were generated parallel to the scanning path at intervals of 2 mm out to 8 mm in order to show the cooling effect. The left image in Figure 5.19 shows an example of the locations of these temperature profiles and the right image shows the average temperature profiles. At 8 mm from the scan path, the part had almost cooled to the same temperature as the surrounding area. Figure 5.20 compares individual temperature profiles from molten pools over solid and powder substrates. The temperature profile of the molten pool over the powder substrate was is much more irregular and jagged than the temperature profile of the molten pool over the solid substrate.

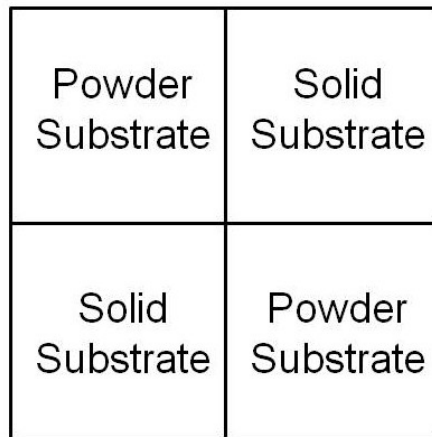


Figure 5.17. Substrate layout of imaged layer.

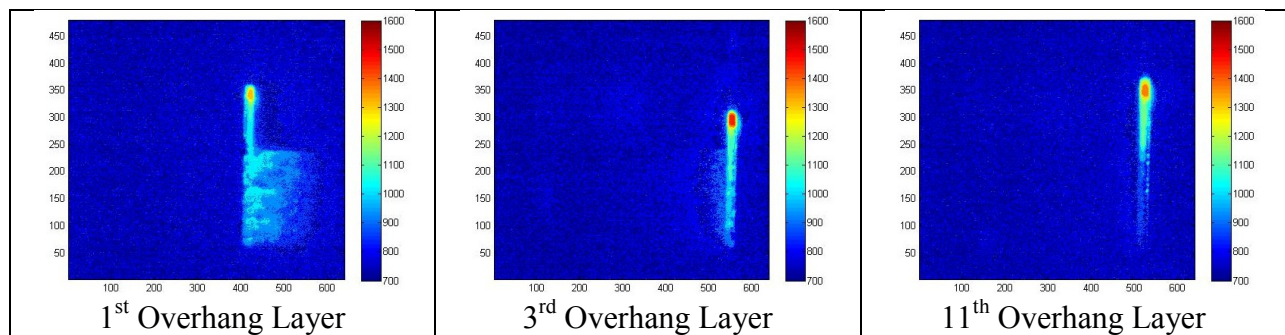


Figure 5.18. Temperature maps showing hatch melting over a half powder-half solid substrate.

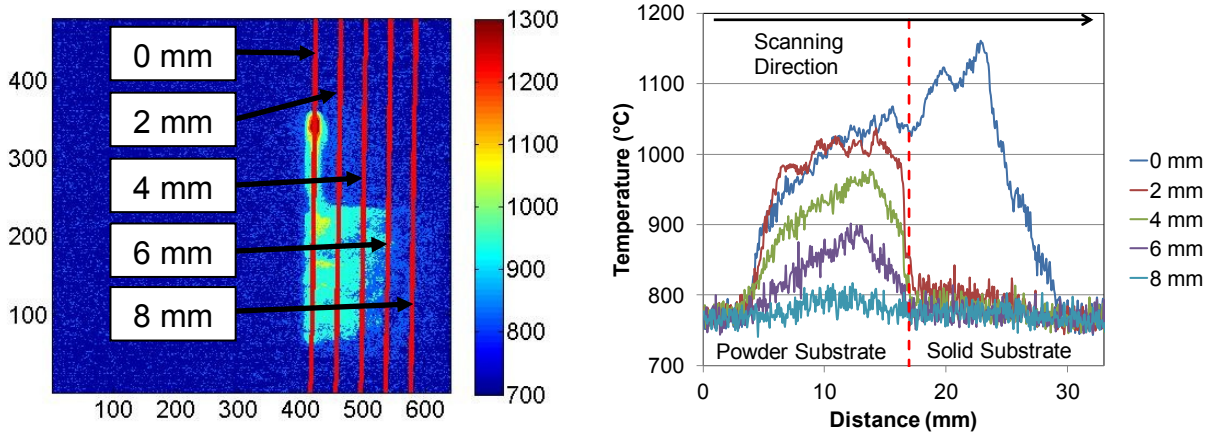


Figure 5.19. Average temperature profiles from first overhang layer of the Overhang Part Experiment.

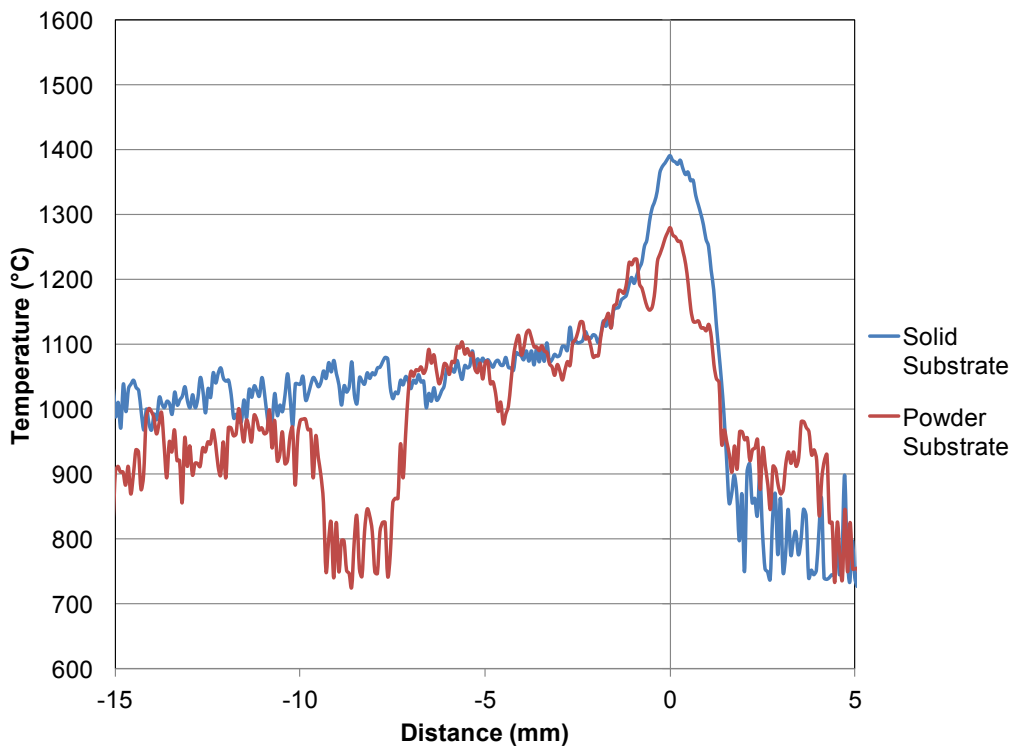


Figure 5.20. Comparison of individual temperature profiles over different substrates from the first overhang layer of the Overhang Part Experiment.

A similar analysis was conducted from the data collected during the Limited Exposure II Experiment. In the layer studied, the left and right thirds of the cross-section had powder substrates and the middle section had a solid substrate. As shown in Figure 5.21, the same phenomenon of a highly reduced cooling rate over the powder substrate was seen. Figure 5.22

compares individual temperature profiles from molten pools over solid and powder substrates. The temperature profile of the molten pool over the powder substrate is jagged, similar to what was seen in the Overhang Part Experiment.

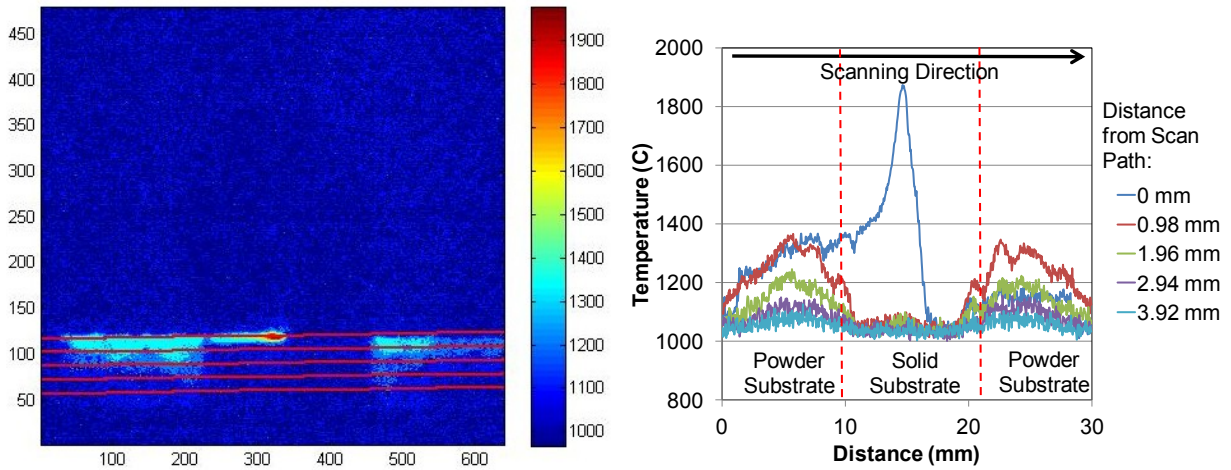


Figure 5.21. Average temperature profiles from the from the first overhang layer of the Limited Exposure II Experiment.

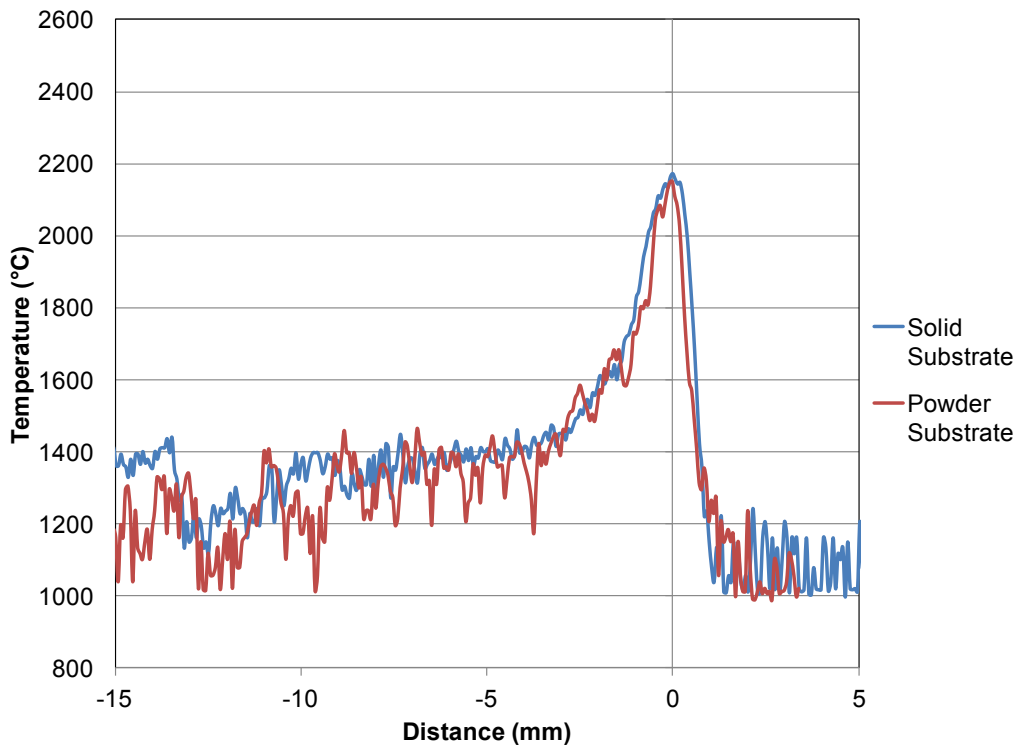


Figure 5.22. Comparison of individual temperature profiles over different substrates from the first overhang layer of the Limited Exposure Experiment II.

Summary

The Arcam speed function algorithm was experimentally studied by fabricating several parts at different speed function indices and monitoring their fabrication with a NIR camera. The beam speed was determined for each part at various build heights and was used to gain an understanding of the relationship between the speed function index, beam speed, and build height. The average temperature profiles and average molten pool dimensions from the different parts were determined so the relationships between the speed function index, build height, and molten pool size could be studied. The effects of melting over a powder substrate were also studied.

CHAPTER VI

CONCLUSIONS AND RECOMMENDATIONS

Conclusions

In this study, an NIR thermal imager was employed to measure the build surface temperatures during an EBAM fabrication process. Many of the challenges in temperature measurements and analyses of the EBAM process such as metallization of the sacrificial glass, associated transmission loss, and uncertainty of the emissivity were addressed and explored. The impact of metallization on the temperature measurements was investigated and an imaging methodology was developed that reduced the amount of transmission loss encountered. A post-processing technique for converting the measured temperatures along the electron beam scanning path to true temperatures by compensating for the experienced transmission loss and estimating the true emissivity was developed. Two-dimensional temperature profiles during hatch melting from various build heights were compared in order to study how their shape changes with the build height. The molten pool dimensions were also experimentally determined at various build heights.

Moreover, the effects of process parameters on the process temperatures and the melt-pool size during hatch melting were evaluated. Several parts were fabricated using different speed function indices. The beam speeds during hatch melting were determined for each speed function at various build heights. The average temperature profiles and dimensions of the molten pools for different speed function values were calculated as well. These studies have

helped provide a better understanding of the speed and beam current function algorithms of Arcam's EBAM systems. The thermal effects in fabricating an overhang feature were also studied by the NIR thermal imager. Temperature distributions from hatch melting of the overhang layers were captured and 2D temperature profiles were obtained to examine the decreased heat dissipations above the powder substrate.

A summary of the major findings from this research is listed below:

1. Metallization on the glass may become severe for a large amount of exposures to the process and may significantly reduce the transmission rate and thus measurement quality. An experiment with controlled exposures was designed to estimate, quantitatively, the transmission loss effects on temperature measurements. For a transmission loss of 15% difference, the temperatures measured appear about 120 °C lower, also a slight function of temperature.
2. In general, the maximum process temperatures during EBAM with Ti-6Al-4V powder are in the range of 2400 °C to 2800 °C, and the length and width of molten pools are in the range of 1.5 to 3.5 mm and 0.6 to 1.0 mm, respectively.
3. The beam speed and the beam current decrease with the build height in EBAM, but the decreasing rate becomes much smaller once the build height reaches about 15 to 20 mm.
4. The larger the speed function, the higher the beam speed, and the smaller the molten-pool size, e.g., for length, 2.4 mm for SF20 vs. 1.25 mm for SF65 at a build height of 6.35 mm.
5. In building an overhang feature, the heat dissipation on the overhang side is much worse due to the low thermal conductivity of the powder. However, such an effect only dominates during the building of the first few layers of the overhang feature.

Recommendations and Future Work

The following are recommendations for future work in the field of temperature measurements of the EBAM process:

1. Development of a technique to prevent the metallization of the sacrificial glass would greatly improve the ease and accuracy of EBAM temperature measurements using NIR thermography.
2. A design of experiments to test different process parameter combinations could be used to generate predictive equations for the molten pool length and width. This information would be very useful for optimizing process parameters to achieve certain microstructures.
3. Further study should be conducted into how the Arcam speed function adjusts the beam speed in response to part geometry. These effects could have impacts on local part properties and users of the EBAM process should be aware of these impacts.

REFERENCES

- Ageorges, C., Ye, L., & Hou, M. (2000). Experimental investigation of the resistance welding for thermoplastic-matrix composites. part I: Heating element and heat transfer. *Composites Science and Technology*, 60(7), 1027-1039.
- Al-Bermani, S. S., Blackmore, M. L., Zhang, W., & Todd, I. (2010). The origin of microstructural diversity, texture, and mechanical properties in electron beam melted ti-6Al-4V. *Metallurgical and Materials Transactions*, 41(A), 3422-3434.
- Alkemper, J., Buchholz, T., Murakami, K., & Ratke, L. (1995). Solidification of aluminum alloys in aerogel moulds. *Journal of Non-Crystalline Solids*, 186, 395-401.
- Arcam AB. Acetabular cup and turbine blade manufactured by EBAM. Retrieved January 6, 2014, from http://ir.arcam.se/files/cup_turbine_blade-1024x843.jpg
- Arcam AB. Arcam S12 EBAM machine. Retrieved January 6, 2014, from <http://www.arcam.eu/>
- Arcam AB. Schematic of Arcam S12 EBAM machine. Retrieved January 6, 2014, from <http://www.arcam.com/wp-content/uploads/schematic-ebm-setup.jpg>
- ASTM Standard F2924-12a, 2012a, "Standard Terminology for Additive Manufacturing Technologies," ASTM International, West Conshohocken, PA, 2012, DOI: 10.1520/F2792-12A, www.astm.org.
- Chivel, Y., & Smurov, I. (2007). SLS-process monitoring and adaptive control. *Proceedings of the Fourth International WLT-Conference on Lasers in Manufacturing*, Munich, Germany. 553-557.
- Cormier, D., Harrysson, O., & West, H. (2004). Characterization of H13 steel produced via electron beam melting. *Rapid Prototyping Journal*, 10(1), 35-41.
- Cormier, D., West, H., Harrysson, O., & Knowlson, K. (2004). Characterization of thin walled ti-6Al-4V components produced via electron beam melting. *Solid Freeform Fabrication Symposium*, Austin, TX. 440-447.
- Craeghs, T., Clijsters, S., Yasa, E., Bechmann, F., Berumen, S., & Kruth, J. P. (2011). Determination of geometrical factors in layerwise laser melting using optical process monitoring. *Optics and Laser in Engineering*, 49, 1440-1446.

- Davies, M. A., Ueda, T., M'Saoubi, R., Mullany, B., & Cooke, A. L. (2007). On the measurement of temperature in material removal processes. *CIRP Annals-Manufacturing Technology*, 52(2), 581-604.
- Del Campo, L., Pérez-Sáez, R. B., González-Fernández, L., Esquisabel, X., Fernández, I., González-Martín, P., & Tello, M. J. (2010). Emissivity measurements on aeronautical alloys. *Journal of Alloys and Compounds*, 489, 482-487.
- Fischer, P., Locher, M., Romano, V., Weber, H. -, Kolossov, S., & Glardon, R. (2004). Temperature measurements during selective laser sintering of titanium powder. *International Journal of Machine Tools and Manufacture*, 44(12), 1293-1296.
- Fischer, P., Romano, V., Weber, H. P., & Kolossov, S. (2004). Pulsed laser sintering of metallic powders. *Thin Solid Films*, 453-454, 139-144.
- Gao, X., You, D., & Katayama, S. (2012). Infrared image recognition for seam tracking monitoring during fiber laser welding. *Mechatronics*, 22, 370-380.
- Gao, Y., Xing, J., Zhang, J., Luo, N., & Zheng, H. (2008). Research on measurement method of selective laser sintering (SLS) transient temperature. *Optik-International Journal for Light and Electron Optics*, 119(13), 618-623.
- Gibson, I., Rosen, D. W., & Stucker, B. (2010). *Additive manufacturing technologies: Rapid prototyping to direct digital manufacturing* Springer.
- Gong, H., Rafi, K., Starr, T., & Stucker, B. (2013). The effects of processing parameters on defect regularity in ti-6Al-4V parts fabricated by selective laser melting and electron beam melting. *Solid Freeform Fabrication Symposium*, Austin, TX. 424-439.
- Gong, X. (2014). *Report of EDS-1016 test*. Unpublished manuscript.
- Gong, X., Anderson, T., & Chou, K. (2012). Review on powder-based electron beam additive manufacturing technology. *ASME 2012 International Symposium on Flexible Automation*, , 1-9.
- Gong, X., Cheng, B., Price, S., & Chou, K. (2013). Powder-bed electron-beam-melting additive manufacturing: Powder characterization, process simulation and metrology. *2013 ASME Early Career Technical Conference*, Birmingham, AL.
- Gong, X., & Chou, K. (2013). Characterization of sintered ti-6Al-4V powders in electron beam additive manufacturing. *ASME 2013 International Manufacturing Science and Engineering Conference*, Madison, WI.
- González-Fernández, L., Risueño, E., Pérez-Sáez, R. B., & Tello, M. J. (2012). Infrared normal spectral emissivity of ti-6Al-4V alloy in the 500-1150 K temperature range. *Journal of Alloys and Compounds*, 541, 144-149.

- Griffith, M. L., Schlienger, M. E., Harwell, L. D., Oliver, M. S., Baldwin, M. D., Ensz, M. T., . . . Nelson, D. V. (1999). Understanding thermal behavior in the LENS process. *Materials and Design*, 20, 107-113.
- Griffith, M., Schlienger, M. E., Harwell, L. D., Oliver, M. S., Baldwin, M. D., Ensz, M. T., & Nelson, D. V. (1998). Thermal behavior in the LENS process. *Solid Freeform Fabrication Symposium*, Austin, TX. 89-96.
- Hagqvist, P., Sikström, F., & Christiansson, A. K. (2013). Emissivity estimation for high temperature radiation pyrometry on ti-6Al-4V. *Measurement*, 46, 871-880.
- Hjertsen, D., Sjöström, J., Bergström, J., & Näsström, M. (2004). Finite element simulation of the tool steel stress response as used in a hot forging. *AIP Conference Proceedings*, 712, 560-565.
- Ho, H. C., Cheung, W. L., & Gibson, I. (2002). Effects of graphite powder on the laser sintering behaviour of polycarbonate. *Rapid Prototyping Journal*, 8, 233-242.
- Hrabe, N., & Quinn, T. (2013). Effects of processing on microstructure and mechanical properties of a titanium alloy (ti-6Al-4V) fabricated using electron beam melting (EBM), part 1: Distance from build plate and part size. *Materials Science & Engineering A*, 573, 564-570.
- Hu, D., & Kovacevic, R. (2003). Modelling and measuring the thermal behavior of the molten pool in closed-loop controlled laser-based additive manufacturing. *Proceedings of the Institution of Mechanical Engineers, Part B: Journal of Engineering Manufacture*, 217(4), 441-452.
- Hu, D., & Kovacevic, R. (2003). Sensing, modeling and control for laser-based additive manufacturing. *International Journal of Machine Tools and Manufacture*, 43(1), 51-60.
- Hu, D., Mei, H., & Kovacevic, R. (2001). Closed loop control of 3D laser cladding based on infrared sensing. *Solid Freeform Fabrication Symposium*, Austin, TX. 129-137.
- Hu, D., Mei, H., & Kovacevic, R. (2002). Improving solid freeform fabrication by laser-based additive manufacturing. *Proceedings of the Institution of Mechanical Engineers, Part B: Journal of Engineering Manufacture*, 216(9), 1253-1264.
- Hua, T., Jing, C., Xin, L., Fengying, Z., & Weidong, H. (2008). Research on molten pool temperature in the process of laser rapid forming. *Journal of Materials Processing Technology*, 198(2), 454-462.
- Kahnert, M., Lutzmann, S., & Zaeh, M. F. (2007). Layer formations in electron beam sintering. *Solid Freeform Fabrication Symposium*, Austin, TX. 88-99.

- Kaschnitz, E., Reiter, P., & McClure, J. L. (2002). Thermophysical properties of solid and liquid 90Ti-6Al-4V in the temperature range from 1400 to 2300 K measured by millisecond and microsecond pulse-heating techniques. *International Journal of Thermophysics*, 23(1), 267-275.
- Kolossov, S., Boillat, E., Glardon, R., Fischer, P., & Locher, M. (2004). 3D FE simulation for temperature evolution in the selective laser sintering process. *International Journal of Machine Tools and Manufacture*, 44, 117-123.
- Li, J. J. (2009). *Study of liquid metals by electrostatic levitation*. (Ph.D.). California Institute of Technology, USA.
- M'Saoubi, R., & Chandrasekara, H. (2004). Investigation of the effects of tool micro-geometry and coating on tool temperature during orthogonal turning of quenched and tempered steel. *International Journal of Machine Tools and Manufacture*, 44(2), 213-224.
- M'Saoubi, R., & Chandrasekara, H. (2011). Experimental study and modelling of tool temperature distribution orthogonal cutting of AISI 316L and AISI 3115 steels. *International Journal of Advanced Manufacturing Technology*, 56(9), 865-877.
- Mahale, T. R. (2009). *Electron beam melting of advanced materials and structures*. (Unpublished Ph.D.). North Carolina State University, Raleigh, NC.
- Miller, J. L. (1994). *Principles of infrared technology: A practical guide to the state of the art*. New York: Van Nostrand Reinhold.
- Miller, S. F., Li, R., Wang, H., & Shih, A. (2006). Experimental and numerical analysis of the friction drilling process. *Journal of Manufacturing Science and Engineering*, 128, 802-810.
- O'Sullivan, D., & Cotterell, M. (2001). Temperature measurement in single point turning. *Journal of Materials Processing Technology*, 118, 301-308.
- Outeiro, J. C., Dias, A. M., & Lebrun, J. L. (2004). Experimental assessment of temperature distributions in three-dimensional cutting process. *Machining Science and Technology*, 8, 357-376.
- Pasandideh-Fard, M., Bhola, R., Chandra, S., & Mostaghimi, J. (1998). Deposition of tin droplets on a steel plate: Simulations and experiments. *International Journal of Heat and Mass Transfer*, 41, 2929-2945.
- Pittalà, G. M., & Monno, M. (2011). A new approach to the prediction of temperature of the workpiece of face milling operations of ti-6Al-4V. *Applied Thermal Engineering*, 31, 173-180.
- Pomfret, M. B., Steinhurst, D. A., & Owrutsky, J. C. (2010). Thermal imaging of a solid oxide fuel cell anode process. *Journal of Power Sources*, 195(1), 257-262.

- Qian, L., Mei, J., Liang, J., & Wu, X. (2005). Influence of position and laser power on thermal history and microstructures of direct laser FabricatedTi-6Al-4V samples. *Materials Science and Technology*, 21(5), 597-605.
- Rodriguez, E., Medina, F., Espalin, D., Terrazas, C., Muse, D., Henry, C., . . . Wicker, R. B. (2012). Integration of a thermal imaging feedback control system in electron beam melting. *Solid Freeform Fabrication Symposium*, Austin, TX. 945-961.
- Schwerdtfeger, J., Singer, R. F., & Kömer, C. (2012). In situ flaw detection by IR-imaging during electron beam melting. *Rapid Prototyping Journal*, 18(4), 259-263.
- Shen, N., & Chou, K. (2012). Thermal modeling of electron beam additive manufacturing process – powder sintering effects. *ASME 2012 International Manufacturing Science and Engineering Conference*, Notre Dame, IN.
- Shur, B. A., & Peletskii, V. E. (2004). The effect of alloying additions on the emissivity of titanium in the neighborhood of polymorphous transformation. *High Temperature*, 42(3), 414-420.
- Sun, Q., Rizvi., G. M., Bellehumeur, C. T., & Gu, P. (2008). Effect of processing conditions on the bonding quality of FDM polymer filaments. *Rapid Prototyping Journal*, 14, 72-80.
- Suzuki, K., & Yao, M. (2004). Simulation of mold filling and solidification during centrifugal precision casting of ti-6Al-4V alloy. *Metal and Materials International*, 10(1), 33-38.
- Tan, H., Chen, J., Zhang, F., Lin, X., & Huang, W. (2010). Estimation of laser solid forming process based on temperature measurement. *Optics & Laser Technology*, 42, 47-54.
- Wang, L., Felicelli, S. D., & Craig, J. E. (2007). Thermal modeling and experiment validation in the LENS process. *Solid Freeform Fabrication Symposium*, Austin, TX. 100-111.
- Wang, L., Felicelli, S. D., & Craig, J. E. (2009). Experimental and numerical study of the LENS rapid fabrication process. *Journal of Manufacturing Science and Engineering*, 131
- Wegner, A., & Witt, G. (2011). Process monitoring in laser sintering using thermal imaging. *Solid Freeform Fabrication Symposium*, Austin, TX. 405-414.
- Whitenton, E. (2010). *High-speed dual-spectrum imaging for the measurement of metal cutting temperatures*. (No. NISTIR 7650).National Institute of Standards and Technology.
- Zäh, M. F., & Lutzmann, S. (2010). Modelling and simulation of electron beam melting. *Production Engineering*, 4(1), 15-23.
- Zalameda, J. N., Burke, E. R., Hafley, R. A., Taminger, K. M., Domack, C. S., Brewer, A., & Martin, R. E. (2013). Thermal imaging for assessment of electron-beam free form fabrication (EBF³) additive manufacturing welds. *SPIE Defense, Security, and Sensing Conference*, Baltimore, MD.

APPENDIX

Sample Matlab Code for Spatial Resolution Calculation

```
map = zeros(480,640); %matrix for storing locations of hot pixels

%finds and stores the locations of the hot pixels from the contour melting frames
for files = 1:75
    filename = ('F:/131030 Text Files/131030-test_1-Contour-Melting-SF20-' num2str(files)
'.txt'); %generates the filename
    thermal = dlmread(filename); %imports thermal data
    maxtemp = max(thermal(:)); %finds maximum temperature
    [y x] = ind2sub(size(thermal),find(thermal>=(maxtemp-25))); %finds the coordinates of the
hot pixels
    xsize = length(x); %number of hot pixels
    %turns the map matrix in a binary matrix where 1 is hot and 0 is cold
    if maxtemp>1000
        for i = 1:xsize
            map(y(i),x(i)) = 1;
        end
    end
end

for files = 1:75
    filename = ('F:/131030 Text Files/131030-test_1-Contour-Melting-SF36-' num2str(files)
'.txt'); %generates the filename
    thermal = dlmread(filename); %imports thermal data
    maxtemp = max(thermal(:)); %finds maximum temperature
    [y x] = ind2sub(size(thermal),find(thermal>=(maxtemp-25))); %finds the coordinates of the
hot pixels
    xsize = length(x); %number of hot pixels
    %turns the map matrix in a binary matrix where 1 is hot and 0 is cold
    if maxtemp>1000
        for i = 1:xsize
            map(y(i),x(i)) = 1;
        end
    end
end

imshow(map) %plots map of hot regions
```

```

hold on
[y1 x1] = ind2sub(size(map),find(map==1)); %finds the coord. of every hot pixel

%identifies the top side
disp(['Select two points on top side']);
figure(1)
top_coord = ginput(2);
m_top = (top_coord(2,2)-top_coord(1,2))/(top_coord(2,1)-top_coord(1,1)); %slope of the top
trendline
b_top = top_coord(1,2)-(m_top*top_coord(1,1)); %y intercept of the top trendline
x_trend = 1:640; %x values for trendlines
y_top = (m_top*x_trend)+b_top; %y values for top trendline
%figure(2)
axis([0 640 0 480])
plot(x_trend,y_top,'LineWidth',2) %plots the top trendline
hold on

%identifies the bottom side
disp(['Select two points on bottom side']);
figure(1)
bottom_coord = ginput(2);
m_bottom = (bottom_coord(2,2)-bottom_coord(1,2))/(bottom_coord(2,1)-bottom_coord(1,1));
%slope of the top trendline
b_bottom = bottom_coord(1,2)-(m_bottom*bottom_coord(1,1)); %y intercept of the top
trendline
x_trend = 1:640; %x values for trendlines
y_bottom = (m_bottom*x_trend)+b_bottom; %y values for top trendline
%figure(2)
plot(x_trend,y_bottom,'LineWidth',2) %plots the bottom trendline

%identifies the left side
disp(['Select two points on left side']);
figure(1)
left_coord = ginput(2);
m_left = (left_coord(2,2)-left_coord(1,2))/(left_coord(2,1)-left_coord(1,1)); %slope of the top
trendline
b_left = left_coord(1,2)-(m_left*left_coord(1,1)); %y intercept of the top trendline
y_trend = 1:480;
x_left = (y_trend-b_left)/m_left;
%figure(2)
plot(x_left,y_trend,'LineWidth',2) %plots the left trendline

%identifies the right side
disp(['Select two points on right side']);
figure(1)
right_coord = ginput(2);

```

```

m_right = (right_coord(2,2)-right_coord(1,2))/(right_coord(2,1)-right_coord(1,1)); %slope of the
top trendline
b_right = right_coord(1,2)-(m_right*right_coord(1,1)); %y intercept of the top trendline
x_right = (y_trend-b_right)/m_right;
%figure(2)
plot(x_right,y_trend,'LineWidth',2) %plots the left trendline

%finds a perpendicular line between the bottom and top sides
m_perp_vert = -1/m_bottom; %slope of the perpendicular line
x_perp_vert_start = 320; %x coordinate that the perpendicular line starts at
y_perp_vert_start = (x_perp_vert_start*m_bottom)+b_bottom; %y coordinate that the
perpendicular line starts at
b_perp_vert = y_perp_vert_start-(x_perp_vert_start*m_perp_vert); %y intercept of the
perpendicular line
I2 = inv([m_top -1; m_perp_vert -1])*[-b_top; -b_perp_vert]; %finds coordinates of the intercept
of perpendicular line and top trendline
xtop_int = I2(1); %x coordinate of the intercept of perpendicular line and top trendline
ytop_int = I2(2); %y coordinate of the intercept of perpendicular line and top trendline
x_perp_vert = x_perp_vert_start:0.01:xtop_int; %x cords. of the perp line
y_perp_vert = (m_perp_vert*x_perp_vert)+b_perp_vert; %y cords. of the perpendicular line
plot(x_perp_vert,y_perp_vert,'-r','LineWidth',2); %plots the perp. line

%finds a perpendicular line between the left and right sides
m_perp_horiz = -1/m_left; %slope of the perpendicular line
y_perp_horiz_start = 240; %y coordinate that the perpendicular line starts at
x_perp_horiz_start = (y_perp_horiz_start-b_left)/m_left; %x coordinate that the perpendicular
line starts at
b_perp_horiz = y_perp_horiz_start-(x_perp_horiz_start*m_perp_horiz); %y intercep of the
perpendicular line
I3 = inv([m_right -1; m_perp_horiz -1])*[-b_right; -b_perp_horiz]; %finds coordinates of the
intercept of perpendicular line and right trendline
xright_int = I3(1); %x coordinate of the intercept of perpendicular line and right trendline
yright_int = I3(2); %y coordinate of the intercept of perpendicular line and right trendline
x_perp_horiz = x_perp_horiz_start:0.01:xright_int; %x coordinates of the perpendicular line
y_perp_horiz = (m_perp_horiz*x_perp_horiz)+b_perp_horiz; %y coordinate of the
perpendicular line
plot(x_perp_horiz,y_perp_horiz,'-r','LineWidth',2);

%calculates the vertical spatial resolution
x_perp_vert_len = xtop_int-x_perp_vert_start; %horizontal leg of the perpendicular line
y_perp_vert_height = ytop_int - y_perp_vert_start; %vertical leg of the perpendicular line
perp_vert_length = sqrt(x_perp_vert_len^2+y_perp_vert_height^2); %pythagorean theorem,
finds length of the perpendicular line
vertresolution = (23/perp_vert_length)*1000; %pixel resolution in  $\mu\text{m}/\text{pixel}$ , actual distance
between top and bottom is 23 mm
disp(['vertical resolution = ' num2str(vertresolution) '  $\mu\text{m}/\text{pixel}$ ']) %displays the resolution

```

```
%calculates the horizontal spatial resolution
x_perp_horiz_len = xright_int-x_perp_horiz_start; %horizontal leg of the perpendicular line
y_perp_horiz_height = yright_int-y_perp_horiz_start; %vertical leg of the perpendicular line
perp_horiz_length = sqrt(x_perp_horiz_len^2+y_perp_horiz_height^2); %pythagorean theorem,
finds length of the perpendicular line
horizresolution = (29/perp_horiz_length)*1000; %pixel resolution in  $\mu\text{m}/\text{pixel}$ , actual distance
between left and right is 29 mm
disp(['horizontal resolution = ' num2str(horizresolution) '  $\mu\text{m}/\text{pixel}$ ']) %displays the resolution
```

Sample Matlab Code for Temperature Profile Determination and Averaging

```
clear all
close all
clc

framecount = [105 60 45 34;104 61 44 34;106 60 45 35;106 62 45 35;130 76 55 43;131 76 55
43;149 88 63 47;149 88 62 48]; % # of frames in each video
videonum = input('What video number would you like to process: ');
speedfunc = input('What speed function: ');
if speedfunc == 20
    ident = 1;
elseif speedfunc == 36
    ident = 2;
elseif speedfunc == 50
    ident = 3;
elseif speedfunc == 65
    ident = 4;
end
data = ['F:/131029 Text Files/131029-test_' num2str(videonum) '-Hatch-Melting-SF'
num2str(speedfunc) '-'];
c = 1;
d = 1;
for imagenum = 1:framecount(videonum,ident);
    clear therm
    filename = [data num2str(imagenum) '.txt'];
    thermal = dlmread(filename);
    maxtemp = max(thermal(:));
    [y x] = ind2sub(size(thermal),find(thermal>=(maxtemp-750)));
    xsize = max(x)-min(x);
    ysize = max(y)-min(y);
    [ypeak xpeak] = ind2sub(size(thermal),find(thermal>=maxtemp-2));
    xsub = xpeak;
    ysub = ypeak;
    if length(xpeak)>1
        clear xpeak ypeak
        xpeak = round((max(xsub)+min(xsub))/2);
        ypeak = round((max(ysub)+min(ysub))/2);
    end
    if maxtemp>1800
        [direction] = direction_finder(thermal,xsize,ysize);
    end
    if xsize>ysize; %Condition for horizontal streak
        %the following section identifies valid pixels for generating a
        %trendline that represents the scan path
        rows = zeros(640,1); %matrix for storing y coordinates used for trending
```

```

columns = zeros(640,1); %matrix for storing x coordinates used for trending
rowtemps = zeros(640,1); %matrix for storing temperatures at these coordinates

for a=1:640
    maxcolumnntemp = max(thermal(:,a)); %find maximum values for each row
    [y1 x1] = ind2sub(size(thermal(:,a)),find(thermal(:,a)>=(maxcolumnntemp-2))); %find
locations of the hottest pixels in each row
    rows(a,:) = round((max(y1)+min(y1))/2); %y coordinates
    columns(a,:) = a; %x coordinates
    rowtemps(a,:) = thermal(rows(a,1),a); %temperatures at these coordinates
end
badtemps = (rowtemps<1400); %identifies low irrelevant temperatures
rows(badtemps) = []; %deletes y coordinates of irrelevant temperatures
columns(badtemps) = []; %deletes x coordinates of irrelevant temperatures

%%This section determines if scan is leftwards or rightwards
peak = find(rowtemps==max(rowtemps)); %finds peak temperature in rowtemps
if length(peak)>1
    peak = round((max(peak)+min(peak))/2);
end

a = 1;
while peak+a<641
    right(a) = rowtemps(peak+a); %vector of the temperatures located to the right of the peak
temp coordinate
    a = a+1;
end
a = 1;
while peak-a>0
    left(a) = rowtemps(peak-a); %vector of the temperatures located to the left of the peak
temp coordinate
    a = a+1;
end

if peak == 640 %case where molten pool intersects the right edge, the "if" statement avoids
an error
    right = 0;
end

left_size = length(find(left>1400)); %number of high temps to the right of the peak
coordinate
right_size = length(find(right>1400)); %number of high temps to the left of the peak
coordinate
good_check = 0;
if left_size>right_size & xpeak>=200 & xpeak<590 & maxtemp>1800
    usable_frames(c,:) = imagenum;

```

```

c = c+1;
if xpeak>200
    xmin = xpeak-200;
else
    xmin = 1;
end
if xpeak<606
    xmax = xpeak+35;
else
    xmax = 640;
end
if ypeak>30
    ymin = ypeak-30;
else
    ymin = 1;
end
if ypeak<451
    ymax = ypeak+30;
else
    ymax = 480;
end
good_check = 1;
end
if left_size<right_size & xpeak<=440 & xpeak>50 & maxtemp>1600
    usable_frames(c,:) = imagenum;
    c = c+1;
    if xpeak>35
        xmin = xpeak-35;
    else
        xmin = 1;
    end
    if xpeak<441
        xmax = xpeak+200;
    else
        xmax = 640;
    end
    if ypeak>30
        ymin = ypeak-30;
    else
        ymin = 1;
    end
    if ypeak<451
        ymax = ypeak+30;
    else
        ymax = 480;
    end
end

```

```

    good_check = 1;
end

if good_check == 1
    scrap = excludedata(columns,rows,'box',[xmin xmax ymin ymax]); %identifies
temperature that are out if the valid region
    streakline = polyfit(columns(~scrap),rows(~scrap),1); %generates trendline
    mstreak = streakline(1); %trendline slope
    bstreak = streakline(2); %trendline y intercept
    xstreak = 1:640; %x values of trendline
    ystreak = round((mstreak*xstreak)+bstreak); %y values of trendline
    a = 1;
    while a <= 640
        therm(1,a) = thermal(ystreak(a),xstreak(a)); %temps to be plotted
        a = a+1;
    end
    figure(1)
    plot(therm)
    human_check = input('Push enter if frame is good and 1 if it is not: ');
    close
    if human_check == 1
    else
        imageplothoriz_master %script that standarizes the temeperature profiles
        final_frames(d,:) = imagenum;
        d = d+1;
    end
    %generates plot of all the temperature profiles plotted
    figure(2);
    plot(temp);
    set(gca,'FontSize',18)
    %legend({legendm(files,:)},'Interpreter','none')
    axis([0 1000 600 3000]);
    xlabel('Pixels','fontsize',18);
    ylabel('Temperature (°C)','fontsize',18);
    hold off
end
end

end

%generates average temperature profile plot
n = sum(temp'~=0); %calucates number of profiles that have a temperature greater than 0 for
each column
avgtemp = transpose(sum(temp') ./ n); %average temperature profile
figure(3);
plot(avgtemp);

```

```

axis([0 1000 600 3000]);
set(gca,'FontSize',18)
xlabel('Pixels','fontsize',18);
ylabel('Temperature (°C)','fontsize',18);
hold off

%generates standard deviation plot
a = 1;
while a <= 1000
    rowpixeltemps = temp(a,:); %temperature of the same pixel for multiple profiles
    temp_id = rowpixeltemps>0; %identifies non-zero temps
    pos_temps = rowpixeltemps(temp_id); %matrix of just the non-zero temps
    standdev(a,:) = std(pos_temps); %standard deviation of profiles
    clear rowpixeltemps temp_id pos_temps
    a = a+1;
end
figure(4)
plot(standdev)
axis([0 1000 0 400])
set(gca, 'FontSize',18)
xlabel('Pixels','fontsize',18)
ylabel('Standard Deviation','fontsize',18)

```

imageplohoriz_master Fucntion Called by Temperature Averaging Code

```
heat = zeros(1000,1); %matrix for storing temperatures
therm_max = max(therm(:)); %maximum temperature in therm matrix
[y_thermpeak1 x_thermpeak1] = ind2sub(size(therm),find(therm>=(therm_max-2))); %finds the
locations of the maximum temperatures along the trendline
if length(x_thermpeak1)>1
    mid = round(length(x_thermpeak1)/2); %finds the center of the hottest region of the trendline
    indtempmax = x_thermpeak1(mid); %the index of the center of the hottest region
    x = xstreak(indtempmax); %x coordinate of the center of the hottest region
    y = ystreak(indtempmax); %y coordinate of the center of the hottest region
else
    indtempmax = x_thermpeak1; %the index of the center of the hottest region
end
peak_temp = therm(1,indtempmax); %hottest temperature on the trendline
heat(500,1) = peak_temp; %place max value at the center of the heat matrix

%this section fills in the heat matrix with the rest of the
%temperatures
i=1;
while i>0;
    if indtempmax<640
        heat(500+i,1) = therm(1,indtempmax+i); %fills in the temperatures above the center
        i = i+1;
        if (indtempmax+i) == 641 %turns off loop once the end of the therm matrix is reached
            i = 0;
        end
    end
    if indtempmax == 640
        i = 0;
    end
end

j=1;
while j>0;
    heat(500-j,1) = therm(1,indtempmax-j); %fills in the temperatures below the center
    j = j+1;
    if (indtempmax-j) == 0 %turns off loop once beginning of therm matrix is reached
        j = 0;
    end
    if (500-j) == 0
        j = 0;
    end
end

if left_size>right_size %condition for rightward scan
```

```

    b=1;
    while b <= 1000
        temp(b,d)=heat(b,1); %fills temp matrix with temperature profile data
        b=b+1;
    end
else %condition for leftward scan
    heat1 = zeros(1000,1);
    heat1(500,1) = heat(500,1);
    i = 1;
    while i > 0 %flips the data,so the plots will match up
        heat1(500+i,1) = heat(500-i,1);
        i = i+1;
        if (500-i) == 0
            i = 0;
        end
    end
end

j = 1;
while j > 0
    heat1(500-j,1) = heat(500+j,1); %flips the data,so the plots will match up
    j = j+1;
    if (500+j) == 1001
        j = 0;
    end
    if (500-j) == 0
        j = 0;
    end
end

b=1;
while b <=length(heat1)
    temp(b,d)=heat1(b,1); %fills temp matrix with temperature profile data
    b=b+1;
end
end

```

Sample Matlab Code for Molten Pool Dimension Calculation

```
clear all
close all
clc

videonum = input('What video number would you like to process: ');

data = xlsread('130904 Hatch Melting Average Temperature Profiles.xlsx','Data');
data_cross = xlsread('130904 Hatch Melting Average Temperature Profiles.xlsx','Data Cross');

pix = data(:,1)+500;
col = 1+(2*videonum);
temps = data(:,col);
temps_cross = data_cross(:,col);
standdev = data(:,col+1);
standdev_cross = data(:,col+1);

figure(1)
plot(pix,temps)
axis([300 530 1000 2800])
hold on
[x,y] = ginput(1);
x_liqtemp = round(x);
liqtemp = temps(x_liqtemp);
temp_stdev = standdev(x_liqtemp);

%finds mp length using liquidus temp
a = 20;
while temps(x_liqtemp+a) >= liqtemp
    a = a+1;
end

temp1 = temps(x_liqtemp+a-1);
temp2 = temps(x_liqtemp+a);
pix1 = x_liqtemp+a-1;
pix2 = x_liqtemp+a;

x1 = x_liqtemp;
x2 = pix1 + (pix2 - pix1)*(liqtemp - temp1)/(temp2 - temp1);

pixdist = x2 - x1;
res = 40.7;
dist = pixdist*res/1000;

%%finds mp length using liquidus temp + standard deviation temp
```

```

a = 1;
while temps(x_liqtemp+a) <= liqtemp+temp_stdev
    a = a+1;
end

temp3 = temps(x_liqtemp+a-1);
temp4 = temps(x_liqtemp+a);
pix3 = x_liqtemp+a-1;
pix4 = x_liqtemp+a;

x3 = pix3 + (pix4 - pix3)*(liqtemp+temp_stdev - temp3)/(temp4 - temp3);
x3rounded = round(x3);

a = 20;
while temps(x3rounded+a) >= liqtemp+temp_stdev
    a = a+1;
end

temp5 = temps(x3rounded+a-1);
temp6 = temps(x3rounded+a);
pix5 = x3rounded+a-1;
pix6 = x3rounded+a;

x4 = pix5 + (pix6 - pix5)*(liqtemp+temp_stdev - temp5)/(temp6 - temp5);

pixdist1 = x4 - x3;
dist_plus = pixdist1*res/1000;

%%finds mp width using liquidus temp

TF = isnan(temps_cross);
a = 1;
while TF(a) == 1
    a = a+1;
end

while temps_cross(a) <= liqtemp
    a = a+1;
end

temp1_cross = temps_cross(a-1);
temp2_cross = temps_cross(a);
pix1_cross = a-1;
pix2_cross = a;

```

```
x1_cross = pix1_cross + (pix2_cross - pix1_cross)*(liqtemp - temp1_cross)/(temp2_cross - temp1_cross);
```

```
while temps_cross(a) >= liqtemp  
    a = a+1;  
end
```

```
temp3_cross = temps_cross(a-1);  
temp4_cross = temps_cross(a);  
pix3_cross = a-1;  
pix4_cross = a;
```

```
x2_cross = pix3_cross + (pix4_cross - pix3_cross)*(liqtemp - temp3_cross)/(temp4_cross - temp3_cross);
```

```
pixdist_cross = x2_cross - x1_cross;  
res_cross = 65.2;  
dist_cross = pixdist_cross*res_cross/1000;
```

```
%%finds mp width using liquidus temp + stand dev  
a = 1;  
while TF(a) == 1  
    a = a+1;  
end
```

```
while temps_cross(a) <= liqtemp+temp_stdev  
    a = a+1;  
end
```

```
temp5_cross = temps_cross(a-1);  
temp6_cross = temps_cross(a);  
pix5_cross = a-1;  
pix6_cross = a;
```

```
x3_cross = pix5_cross + (pix6_cross - pix5_cross)*((liqtemp+temp_stdev) - temp5_cross)/(temp6_cross - temp5_cross);
```

```
while temps_cross(a) >= liqtemp+temp_stdev  
    a = a+1;  
end
```

```
temp7_cross = temps_cross(a-1);  
temp8_cross = temps_cross(a);  
pix7_cross = a-1;  
pix8_cross = a;
```

```

x4_cross = pix7_cross + (pix8_cross - pix7_cross)*((liqtemp+temp_stdev) -
temp7_cross)/(temp8_cross - temp7_cross);

pixdist1_cross = x4_cross - x3_cross;
dist_plus_cross = pixdist1_cross*res_cross/1000;

%%finds mp width using liquidus temp - stand dev

a = 1;
while TF(a)== 1
    a = a+1;
end

while temps_cross(a) <= liqtemp-temp_stdev
    a = a+1;
end

temp9_cross = temps_cross(a-1);
temp10_cross = temps_cross(a);
pix9_cross = a-1;
pix10_cross = a;

x5_cross = pix9_cross + (pix10_cross - pix9_cross)*((liqtemp-temp_stdev) -
temp9_cross)/(temp10_cross - temp9_cross);

while temps_cross(a) >= liqtemp-temp_stdev
    a = a+1;
end

temp11_cross = temps_cross(a-1);
temp12_cross = temps_cross(a);
pix11_cross = a-1;
pix12_cross = a;

x6_cross = pix11_cross + (pix12_cross - pix11_cross)*((liqtemp-temp_stdev) -
temp11_cross)/(temp12_cross - temp11_cross);

pixdist2_cross = x6_cross - x5_cross;
dist_minus_cross = pixdist2_cross*res_cross/1000;

%plots

plot([x1 x2],[liqtemp liqtemp])
plot([x3 x4],[liqtemp+temp_stdev liqtemp+temp_stdev])
hold off

```

```
figure(2)
plot(pix,temps_cross)
axis([300 700 1000 2400])
hold on
plot([x1_cross x2_cross],[liqtemp liqtemp])
plot([x3_cross x4_cross],[liqtemp+temp_stdev liqtemp+temp_stdev])
plot([x5_cross x6_cross],[liqtemp-temp_stdev liqtemp-temp_stdev])

mp_length = [dist;dist-dist_plus]
mp_width = [dist_cross;dist_minus_cross-dist_cross;dist_cross-dist_plus_cross]
```

Sample Beam Speed Calculation Code

```
clear all
close all
clc

videonum = input('What video: ');
speedfunc = input('What speed function: ');
sheetname = ['Test ' num2str(videonum) ' SF' num2str(speedfunc)]; %identifies name of sheet
that frame parameters are located on

if speedfunc == 20
    id = 1;
elseif speedfunc == 36
    id = 2;
elseif speedfunc == 50
    id = 3;
elseif speedfunc == 65
    id = 4;
end
frames = xlsread('131029 Consecutive Frames.xlsx',sheetname); %excel file identifying frames
to be plotted
cycles = length(frames); %number of frames to be plotted
data = ['F:/131029 Text Files/131029-test_' num2str(videonum) '-Hatch-Melting-SF'
num2str(speedfunc) '-']; %used to generate first part of filename
res_horiz = 48.5;
res_vert = 65.2;
files = 1;
a = 1;
while files <= (length(frames)-1)
    imagenum1 = frames(files);
    imagenum2 = frames(files+1);
    filename1 = [data num2str(imagenum1) '.txt'];
    filename2 = [data num2str(imagenum2) '.txt'];
    thermal1 = dlmread(filename1);
    thermal2 = dlmread(filename2);
    maxtemp1 = max(thermal1(:));
    maxtemp2 = max(thermal2(:));
    [ymax1 xmax1] = ind2sub(size(thermal1),find(thermal1==maxtemp1));
    [ymax2 xmax2] = ind2sub(size(thermal2),find(thermal2==maxtemp2));
    if length(xmax1)>1 || length(xmax2)>1
        xmax1 = round(mean(xmax1));
        ymax1 = round(mean(ymax1));
        xmax2 = round(mean(xmax2));
        ymax2 = round(mean(ymax2));
    end
end
```

```
m(a) = (ymax2-ymax1)/(xmax2-xmax1);
b(a) = ymax1-(m(a)*xmax1);

horizpix = abs(xmax2-xmax1);
vertpix = abs(ymax2-ymax1);
horizmm = horizpix*res_horiz/1000;
vertmm = vertpix*res_vert/1000;
dist = sqrt(horizmm^2+vertmm^2);
framerate = 58;
frametime = 1/framerate;
beamspeed(a,:) = dist/frametime;
files = files+2;
a = a+1;
end

beamspeed_avg = mean(beamspeed)
beamspeed_std = std(beamspeed)
```